**Astronomy
&
Astrophysics**

Comprehensive comparison of models for spectral energy distributions from 0.1 μm to 1 mm of nearby star-forming galaxies

L. K. Hunt[1], I. De Looze[2,3], M. Boquien[4], R. Nikutta[5,6], A. Rossi[7], S. Bianchi[1], D. A. Dale[8],
G. L. Granato[9], R. C. Kennicutt[10,11,12], L. Silva[9], L. Ciesla[13,14], M. Relaño[15,16], S. Viaene[3,17],
B. Brandl[18], D. Calzetti[19], K. V. Croxall[20,21], B. T. Draine[22], M. Galametz[23,13,14], K. D. Gordon[24,3],
B. A. Groves[25], G. Helou[26], R. Herrera-Camus[27], J. L. Hinz[11], J. Koda[28], S. Salim[29], K. M. Sandstrom[30],
J. D. Smith[31], C. D. Wilson[32], and S. Zibetti[1]

(Affiliations can be found after the references)

ABSTRACT

We have fit the far-ultraviolet (FUV) to sub-millimeter (850 μm) spectral energy distributions (SEDs) of the 61 galaxies from the Key Insights on Nearby Galaxies: A Far-Infrared Survey with *Herschel* (KINGFISH). The fitting has been performed using three models: the Code for Investigating GALaxy Evolution (CIGALE), the GRAphite-SILicate approach (GRASIL), and the Multiwavelength Analysis of Galaxy PHYSical properties (MAGPHYS). We have analyzed the results of the three codes in terms of the SED shapes, and by comparing the derived quantities with simple "recipes" for stellar mass (M_{star}), star-formation rate (SFR), dust mass (M_{dust}), and monochromatic luminosities. Although the algorithms rely on different assumptions for star-formation history, dust attenuation and dust reprocessing, they all well approximate the observed SEDs and are in generally good agreement for the associated quantities. However, the three codes show very different behavior in the mid-infrared regime: in the 5–10 μm region dominated by PAH emission, and also between 25 and 70 μm where there are no observational constraints for the KINGFISH sample. We find that different algorithms give discordant SFR estimates for galaxies with low specific SFR, and that the standard recipes for calculating FUV absorption overestimate the extinction compared to the SED-fitting results. Results also suggest that assuming a "standard" constant stellar mass-to-light ratio overestimates M_{star} relative to the SED fitting, and we provide new SED-based formulations for estimating M_{star} from WISE W1 (3.4 μm) luminosities and colors. From a principal component analysis of M_{star}, SFR, M_{dust}, and O/H, we reproduce previous scaling relations among M_{star}, SFR, and O/H, and find that M_{dust} can be predicted to within ~0.3 dex using only M_{star} and SFR.

Key words. galaxies: fundamental parameters – galaxies: star formation – galaxies: ISM – galaxies: spiral – infrared: galaxies –
ultraviolet: galaxies

1. Introduction

As galaxies form and evolve, their spectral energy distributions (SEDs) are characterized by different shapes. Dust grains reprocess stellar radiation to a degree which depends on many factors, but mainly on the galaxy's evolutionary state and its star-formation history (SFH). Stars form in dense, cool giant molecular clouds and complexes (GMCs), and heat the surrounding dust; as the stars age, the dust cools, and the stars emerge from their natal clouds. As evolution proceeds, the dust in the diffuse interstellar medium (ISM) is heated by the more quiescent interstellar radiation field (ISRF) of an older stellar population. Thus dust emission is a fundamental probe of the SFH of a galaxy, and the current phase of its evolution. A direct comparison of luminosity emitted by dust compared to that by stars shows that, overall, roughly half of the stellar light is reprocessed by dust over cosmic time (Hauser & Dwek 2001; Dole et al. 2006; Franceschini et al. 2008).

Over the last two decades, the increasing availability of data from ultraviolet (UV) to far-infrared (FIR) wavelengths has led to the development of several physically-motivated models for fitting galaxy SEDs. Among these are the Code for Investigating GALaxy Evolution (CIGALE, Noll et al. 2009), the GRAphite-SILicate approach (GRASIL, Silva et al. 1998), and the Multi-wavelength Analysis of Galaxy

PHYSical Properties (MAGPHYS, da Cunha et al. 2008). These algorithms rely on somewhat different assumptions for inferring SFH, extinction curves, dust reprocessing, and dust emission, and are all widely used for deriving fundamental quantities such as stellar mass M_{star}, star-formation rate SFR and total IR (TIR) luminosity L_{TIR} from galaxy SEDs (e.g., Iglesias-Páramo et al. 2007; Michałowski et al. 2008; Burgarella et al. 2011; Giovannoli et al. 2011; Buat et al. 2012; Smith et al. 2012; Berta et al. 2013; Lo Faro et al. 2013; Pereira-Santaella et al. 2015). While comparisons with simulations show that the codes are generally able to reproduce observed SEDs (e.g., Hayward & Smith 2015), little systematic comparison has been done of the codes themselves (although see Pappalardo et al. 2016). In this paper, we perform such a comparison using updated photometry (Dale et al. 2017) from the UV to sub-millimeter (submm) of a sample of galaxies from the Key Insights on Nearby Galaxies: A FIR Survey with *Herschel* (KINGFISH, Kennicutt et al. 2011).

The KINGFISH sample of 61 galaxies is ideal for comparing SED fitting algorithms, as there is a wealth of photometric and spectroscopic data over a wide range of wavelengths (see Dale et al. 2017). KINGFISH galaxies are selected to be nearby (≲30 Mpc) and to span the wide range of morphology, stellar mass, dust opacity, and SFR observed in the Local Universe. 57 of the 61 galaxies also are part of the SIRTF

Infrared Nearby Galaxy Survey (SINGS, Kennicutt et al. 2003). Although the KINGFISH sample is somewhat biased toward star-forming galaxies, several host low-luminosity active galactic nuclei (e.g., NGC 3627, NGC 4594, NGC 4569, NGC 4579, NGC 4736, NGC 4826), and ten galaxies are early types, ellipticals or lenticulars. As we shall see in more detail in the following sections, KINGFISH stellar masses span ~ 5 orders of magnitude from $\sim 10^6$ to $10^{11} M_\odot$, and most are along the "main-sequence" relation of SFR and $M_{\rm star}$ (SFMS, Brinchmann et al. 2004; Salim et al. 2007).

The rest of the paper is structured as follows: the three SED-modeling codes are described in Sect. 2. In Sect. 3, we analyze differences in the SEDs from the three algorithms and compare the fitted galaxy parameters to independently-derived quantities. The ramifications of the different assumptions made in the models are discussed in Sect. 4. Section 5 presents general scaling relations, together with refined "recipes" for calculating stellar mass, and a principal component analysis (PCA) to ameliorate the effect of mutual correlations among the parameters. We summarize our conclusions in Sect. 6.

2. The SED-fitting codes

All the codes rely on a given SFH, with stellar emission defined by an initial mass function (IMF; here Chabrier 2003), applied to Single-age Stellar Populations (SSPs, here Bruzual & Charlot 2003). However, the assumed SFHs are code dependent as are the assumptions for calculating dust extinction and dust emission, and the relative ratio of stars to dust.

The codes share the aim of solving the Bayesian parameter inference problem:

$$P(\boldsymbol{\theta}|\boldsymbol{D}) \propto P(\boldsymbol{\theta})P(\boldsymbol{D}|\boldsymbol{\theta}) \qquad (1)$$

seeking to derive the full posterior probability distribution $P(\boldsymbol{\theta}|\boldsymbol{D})$ of galaxy physical parameter vector $\boldsymbol{\theta}$ given the data vector $\boldsymbol{D}$ (the observed SED). This posterior is proportional to the product of the prior $P(\boldsymbol{\theta})$ on all model parameters (the probability of a model being drawn before seeing the data), and the likelihood $P(\boldsymbol{D}|\boldsymbol{\theta})$ that the data are compatible with a model generated by the parameters[1]. If the data carry Gaussian uncertainties, the likelihood is proportional to $\exp(-\chi^2/2)$ (see e.g., Trotta 2008; Nikutta 2012).

In the following, we describe each model in some detail, and give a summary of the different assumptions in Table 1. Conceptual differences and possible ramifications for the various approaches will be discussed in Sect. 4. For all three codes, the uncertainties of the inferred parameters correspond to the 16% and the 84% percentiles ($\pm 1\sigma$ confidence intervals) of their marginalized posterior probability distribution functions (PDFs).

2.1. CIGALE

The CIGALE[2] (Code Investigating GALaxy Evolution; Noll et al. 2009; Ciesla et al. 2016; Boquien et al. 2019) code is built around two central concepts to model galaxies and estimate their physical properties:

1. CIGALE assumes that the energy that is absorbed by the dust from the UV to the near-infrared (NIR) is re-emitted self-consistently in the mid- (MIR) and far-infrared (FIR).

2. The physical properties and the associated uncertainties are estimated in a Bayesian-like way over a systematic grid.

In practice the models are built combining several components: an SFH that can be analytic or arbitrary, single-age stellar populations, templates of ionized gas including lines and continuum (free-free, free-bound, and 2-photon processes), a flexible dust attenuation curve, dust emission templates, synchrotron emission, and finally the effect of the intervening intergalactic medium. Each component is computed by an independent module; different modules are available. For instance, stellar populations can be modeled alternatively with the Bruzual & Charlot (2003) or the Maraston (2005) models. For this run, we have used the following modules and sets of parameters:

- The star-formation history is modeled following a so-called "delayed" parametrization (e.g., Ciesla et al. 2016):

$$\mathrm{SFR}(t) \propto \begin{cases} t\,\exp(-t/\tau) & \text{when } t \leq t_{\rm trunc} \\ r_{\rm SFR}\,\mathrm{SFR}(t = t_{\rm trunc}) & \text{when } t > t_{\rm trunc}. \end{cases} \qquad (2)$$

The second case[3], with $r_{\rm SFR}$, considers reduced SFR for $t > t_{\rm trunc}$ (e.g., quenching), or an increase of star formation occurring at time $t_{\rm trunc}$.
- The stellar emission is computed adopting the Bruzual & Charlot (2003) SSPs with a metallicity $Z = 0.02$ and a Chabrier (2003) IMF;
- With the stellar spectrum computed, the nebular emission is included based on the production rate of Lyman continuum photons. CIGALE employs templates computed using CLOUDY models, with the same metallicity as the stellar population. We fixed the CIGALE ionisation parameter log $U_{\rm ion} = -2$, and assumed that 100% of the Lyman continuum photons ionise the gas, that is, the escape fraction is zero and Lyman continuum photons do not contribute directly to dust heating;
- To account for the absorption of stellar and nebular radiation by interstellar dust, CIGALE adopts a modified starburst attenuation law (e.g., Calzetti et al. 2000) that considers differential reddening of stellar populations of different ages: the baseline law is multiplied by a power law in wavelength λ^δ, with the slope δ ranging from -0.5 and 0.0 with steps of 0.1. The normalisation $E(B - V)$ for stars younger than 10 Myr ranges from 0.01 mag to 0.60 mag. To account for the difference in attenuation for stars of different ages (e.g., Charlot & Fall 2000), CIGALE includes an attenuation reduction factor for stars older than 10 Myr; here we set it to 0.25, 0.50, or 0.75. Finally, CIGALE adds a variable bump in the attenuation curve at $0.2175\,\mu$m with a strength of 0.0 (no bump), 1.5, or 3.0 (Milky-Way-like);
- With the total luminosity absorbed by the dust, the energy is re-emitted self-consistently adopting the Draine & Li (2007) and Draine et al. (2014) dust models, assuming that the dust emission is optically thin. CIGALE considers possible variations of the polycyclic aromatic hydrocarbon (PAH) abundance ($q_{\rm PAH}$=0.47, 2.50, 4.58, or 6.62%), of the minimum radiation field intensity ($U_{\rm min} = 0.10$, 0.25, 0.50, 1.0, 2.5, 5.0, 10, or 25), and the fraction of the dust mass γ heated by a power-law distribution of ISRF intensities ($U^{-\alpha}$) with log γ ranging from -3.0 to -0.3 in 10 steps. The maximum starlight intensity $U_{\rm max}$ is fixed to 10^7, and α, the power-law index is fixed to 2.0.

---

[1] Although the parameter inference problem is the same for all the codes, the model physical parameter vector $\boldsymbol{\theta}$ is different for each model.
[2] http://cigale.lam.fr

[3] $r_{\rm SFR}$ [$= \mathrm{SFR}(t > t_{\rm trunc})/\mathrm{SFR}(t_{\rm trunc})$] is a constant that quantifies a steady SFR at and after time $t_{\rm trunc}$, that could be higher or lower than the SFR at $t = t_{\rm trunc}$.

Table 1. Summary of model assumptions for SED fitting.

Property	CIGALE	GRASIL[a]	MAGPHYS
SFH	SFR(t_{gal}) delayed+truncation (defined by Eq. (2)) with $t_{gal} = (8, 10, 12)$ Gyr; $\tau = (0.5, 1, 2, 4, 8)$ Gyr; $r_{SFR} = (0.01, 0.05, 0.1, 0.5, 1, 5, 10)$; $age_{trunc} = (10, 100, 1000)$ Myr[b].	SFR(t_{gal}) $= \nu\, M_{gas}(t_{gal})^k$ with primordial gas infall described as $\dot{M}_{gas} \propto \exp(-t/\tau_{inf})$; $k = 1$; (NSS)[c] $\nu = (0.3, 0.5, 0.8, 2.3, 8.0, 23.0)$ Gyr^{-1}; (NSS)[c] $\tau_{inf} = (0.01, 0.1, 0.5, 1, 2, 5, 10)$ Gyr; (NSS)[c] $t_{gal} = (0.01, 0.02, 0.05, 0.1, 0.2, 0.5, 1, 2, 4, 7, 10, 13)$ Gyr.	SFR(t_{gal}) $= \exp(-\gamma\, t_{gal})$ with random bursts potentially occurring at all times with amplitude $A = M_{burst}/M_{const}$, the ratio of the stellar masses in the burst and exponentially declining component; $t_{gal} \in [0.1, 13.5]$ Gyr; burst duration $\in [3, 30]$ Myr.
Geometry	None	Two geometries: (NSS) spheroid with King profiles for stars and dust, and (NSD) disk radial+vertical exponential profiles for stars and dust; GMCs are randomly embedded within each of these structural components; stellar radial scalelength (NSS)[c] $R_{gal} = (0.04, 0.14, 0.52, 1.9, 7.2, 26.6)$ kpc; (NSD) inclination angle i such that $\cos(i) = (1, 0.8, 0.6, 0.4, 0.2, 0)$.	None
Stellar populations	Bruzual & Charlot (2003) SSPs with Chabrier (2003) IMF, and solar metallicity ($Z = Z_\odot$).	Bruzual & Charlot (2003) SSPs with Chabrier (2003) IMF, and metallicities ranging from $Z = 0.01\, Z_\odot$ to $Z = 2.5\, Z_\odot$.	Bruzual & Charlot (2003) SSPs with Chabrier (2003) IMF, and metallicities ranging from $Z = 0.02\, Z_\odot$ to $Z = 2\, Z_\odot$.
Ionized gas?	Yes[d]	No	No
Dust attenuation	Modified starburst attenuation law with power-law slope $\delta = (-0.5, -0.4, -0.3, -0.2, -0.1, 0.0)$; normalization $E(B-V)$ for stars younger than 10 Myr $\in [0.01, 0.60]$ mag; differential $E(B-V)$ factor $E(B-V)_{old}/E(B-V)_{young} = (0.25, 0.50, 0.75)$; variable $0.2175\,\mu m$ bump with strength of 0.0 (no bump), 1.5, 3.0 (Milky-Way-like).	Attenuation law as a consequence of geometry, grain opacities from Laor & Draine (1993) mediated over grain size distributions from $0.001\,\mu m$ to $10\,\mu m$, and radiative transfer of the GMC and diffuse dust components. Free parameters are: $R_{gmc} = (6.1, 14.5, 22.2, 52.2)$ pc; $f_{mol} = (0.1, 0.3, 0.5, 0.9)$; $t_{esc} = (0.001, 0.005, 0.015, 0.045, 0.105)$ Gyr.	Two-component (BC, ambient ISM) dust attenuation (Charlot & Fall 2000) as in Eq. (4) with $\mu \in [0,1]$, drawn from the probability density function $p(\mu) = 1 - \tan h(8\mu - 6)$; $\hat{\tau}_V$ parametrized according to the probability density function $p(\hat{\tau}_V) = 1 - \tan h(1.5\hat{\tau}_V - 6.7)$. Optical depth $\hat{\tau}_V$ is time-dependent as in Eq. (3).
Dust emission	Overall dust luminosity defined by energy-balance considerations with SED shape governed by the dust models of Draine et al. (2007, 2014). With the exception of one ($\alpha \equiv 2.0$), parameters of these models are left to vary: $q_{PAH} = (0.47, 2.50, 4.58, 6.62)\%$; $U_{min} = (0.10, 0.25, 0.50, 1.0, 2.5, 5.0, 10, 25)$; $\log \gamma = [-3.0, -0.3]$ in 10 steps. Dust emission is assumed to be optically thin; the DL07 models used in CIGALE have $\kappa_{abs} = 0.38$ cm^2 g^{-1} at $850\,\mu m$.	Overall dust luminosity and SED shape governed by geometry, grain opacities from Laor & Draine (1993) mediated over grain size distributions from $0.001\,\mu m$ to $10\,\mu m$, and radiative transfer of the GMC and diffuse dust components. The dust column is assumed to be proportional to the metallicity of the given SFH, and the consistent relation between extinction and emission ensures energy conservation. The same variable parameters for dust extinction govern dust emission through radiative transfer. Dust opacity $\kappa_{abs} = 0.56$ cm^2 g^{-1} at $850\,\mu m$ (Laor & Draine 1993).	Overall dust luminosity defined by energy-balance considerations with SED shape governed by four species of dust emitters in two environments (BC, ambient ISM), with both having PAH+hot+warm grains (ξ_{PAH}^{BC}, ξ_{MIR}^{BC}, ξ_{W}^{BC}, ξ_{PAH}^{ISM}, ξ_{MIR}^{ISM}, ξ_{W}^{ISM}), but an additional cold-dust component for the ambient ISM (ξ_{C}^{ISM}). In addition to ensuring unity ($\xi_{PAH}^{BC} + \xi_{MIR}^{BC} + \xi_{W}^{BC} = 1$, $\xi_{PAH}^{ISM} + \xi_{MIR}^{ISM} + \xi_{W}^{ISM} + \xi_{C}^{ISM} = 1$) fixed parameters are: $\xi_{PAH}^{ISM} = 0.550(1 - \xi_{C}^{ISM})$; $\xi_{MIR}^{ISM} = 0.275(1 - \xi_{C}^{ISM})$; and $\xi_{W}^{ISM} = 0.175(1 - \xi_{C}^{ISM})$. Parameters left to vary are: $\xi_{W}^{BC} \in [0,1]$; $\xi_{MIR}^{BC} \in [0, 1 - \xi_{W}^{BC}]$; $\xi_{C}^{ISM} \in [0,1]$; $T_{W}^{BC} \in [30,70]$ K; $T_{W}^{ISM} \in [30,70]$ K; $T_{C}^{ISM} \in [10,30]$ K. Dust emission is assumed to be optically thin; dust opacity $\kappa_{abs} = 0.77$ cm^2 g^{-1} at $850\,\mu m$ (Dunne et al. 2000).
Free parameters	11 with SFH (t_{gal}, τ, r_{SFR}, age_{trunc}); dust attenuation (δ, normalization $E(B-V)$, differential $E(B-V)$, variable $0.2175\,\mu m$ bump strength); dust emission (q_{PAH}, U_{min}, γ).	7 for NSS templates with SFH (t_{gal}, τ_{inf}, ν); geometry (R_{gal}); dust attenuation (R_{gmc}, f_{mol}, t_{esc}); dust emission (same as for dust attenuation). 8 for NSD templates with the addition of galaxy inclination (viewing angle).	12 with SFH (γ, t_{gal}, A, Z_{star}); dust attenuation (μ, and $\hat{\tau}_V$); dust emission (ξ_{W}^{BC}, ξ_{MIR}^{BC}, T_{W}^{BC}, ξ_{C}^{ISM}, T_{C}^{ISM}, T_{W}^{ISM}).

Notes. [a]The parameter ranges for GRASIL are sampling points only; ultimately the best-fit parameters are interpolated so that essentially the entire range of parameters is covered making the symbol $\in$ more appropriate (see text for more details). [b]Age of the truncation at $t = t_{trunc}$. [c]For the NSD library: $\nu = (0.3, 0.9, 3, 9)$; $\tau_{inf} = (0.1, 0.5, 1, 5, 10)$ Gyr; $t_{gal} = (0.5, 1.25, 2, 5, 13)$ Gyr. $R_{gal} = (0.1, 0.3, 1, 3, 10)$ kpc; $R_{gmc} = (6.1, 13.1, 19.3, 28.1)$ pc; $f_{mol} = (0.1, 0.2, 0.5, 0.9)$; $t_{esc} = (0.001, 0.002, 0.005, 0.02, 0.05, 0.1)$ Gyr. [d]See Sect. 2.1 for details.

With 11 variables sampled as described, the total grid consists of 80 870 400 model templates. Each model is fitted to the observations by computing the χ^2 on all valid bands; data points with only upper limits were discarded for consistency with the other codes that cannot accommodate them. Data are fitted in f_ν (linear) space. Finally, the output parameters are obtained by computing the likelihood of the models, and the likelihood-weighted means and standard deviations to estimate the physical properties and the associated uncertainties.

2.2. GRASIL

The GRASIL[4] chemo-spectrophotometric self-consistent models (Silva et al. 1998) rely on a chemical evolution code that follows the SFR, the gas fraction, and the metallicity, comprising the basic ingredients for a stellar population synthesis. The stellar populations are simulated through a grid of integrated spectra of SSPs of different ages and metallicities. The newest version of the code adopted here relies on a Chabrier (2003) IMF, and is based on the Bruzual & Charlot (2003) populations.

The chemical evolution process is modeled through a separate code (CHE_EVO, Silva 1999) that considers the infall of primordial (metal-free) gas with an exponential folding timescale (τ_{inf}) in order to simulate the cold-accretion phase of galaxy formation ($\dot{M}_{gas} \propto \exp(-t/\tau_{inf})$). The SFR scheme is a Schmidt/Kennicutt-type law (e.g., Schmidt 1959; Kennicutt 1998), with SFR $= \nu \times M_{gas}^k$, where M_{gas} is the available gas mass, and ν the SF efficiency. Thus the model describes a SFH according to the variations of the input parameters τ_{inf} and ν: the current version of the code includes 49 SFHs for the spheroids (see below), and 20 SFHs for the disks. The smaller range for τ_{inf} and ν (see Table 1) is sufficient for the disks (e.g., Calura et al. 2009).

The effects of dust on SEDs depend on the relative spatial distribution of stars and dust. Hence GRASIL relies on three components: star-forming GMCs, stars that have already emerged from these clouds, and diffuse gas+dust (e.g., cirrus-like). Disk galaxies are described through a double exponential (radial, vertical), assuming that the dust is distributed radially like the stars, but has a smaller vertical scale height (specifically 0.3 times the stellar vertical scale, see Bianchi 2007). The vertical stellar scaleheight is taken to be 0.1 of the stellar radial scale length. Spheroidal systems are quantified by King (1962) profiles for both the stars and the dust. For both geometries, GMCs are embedded within these structural components. Once the geometry is given, radiative transfer is performed through the GMCs and the diffuse medium assuming the Laor & Draine (1993) opacities for grain sizes from $0.001\,\mu m$ to $10\,\mu m$, mediated over the grain size distribution given by Silva et al. (1998). The relative contribution of dust and gas, namely the dust-to-gas ratio, is taken to be proportional to the metallicity of the given SFH. More details are found in Silva et al. (1998).

For this work, we have computed with GRASIL $\sim 3 \times 10^6$ spheroidal SED templates (new star-forming spheroids, NSS), and 1.2×10^6 disk templates (new star-forming disks, NSD), corresponding to the full Cartesian product of all values sampled per model parameter. The common seven free parameters for both NSS and NSD are:

- for the SFH: the exponential folding timescale (τ_{inf}), the SF efficiency (ν), galaxy age (t_{gal});
- radius R_{gmc} of the molecular clouds that, since cloud mass is fixed, defines optical depth of the GMCs;

- molecular gas mass fraction (f_{mol});
- escape time (t_{esc}) for the stars to emerge from GMCs;
- radial scale lengths (R_{gal}) (vertical dimension scales with this).

An additional free parameter is needed for the NSD library: galaxy inclination or viewing angle i.

Operationally, the SED library is reshaped into seven- (NSS) and eight-dimensional (NSD) hypercubes. The wavelength axis of the SEDs is considered as an additional dimension in the cube, and the cube axes represent the model parameters. The vertices of the hypercubes correspond to unique combinations of model parameters; here the sampling is either linear or logarithmic (per-axis), ensuring that the parameter space is sufficiently covered by the sampling.

The hypercubes enable multidimensional interpolation of SEDs at *any* continuous vector of model parameter values $\boldsymbol{\theta} = \{\theta_j\}$, $j \in (\tau_{inf}, \nu, t_{gal}, R_{gmc}, f_{mol}, t_{esc}, R_{gal}, (i))$ within the envelope spanned by the parameter axes, that is not just at the discrete grid vertices. An important assumption in this scheme is that every parameter axis is sampled finely enough so as not to miss important features in the output SED.

To fit an observed SED we run a Markov chain Monte-Carlo code originally developed in Nikutta (2012). It invokes a Metropolis-Hastings sampler (Metropolis et al. 1953; Hastings 1970) which at every step samples from log-uniform priors $P(\boldsymbol{\theta})$ on all free model parameters (except λ, for which we use the observed set of wavelengths). The model SED is interpolated from the hypercube on the fly using the sampled $\boldsymbol{\theta}$ as input, and compared to the observed SED, logging the likelihood. A long chain of samples is recorded in the run, which by construction of the MCMC algorithm converges toward the posterior distribution $P(\boldsymbol{\theta}|\boldsymbol{D})$.

The histograms of the chains are the marginalized one-dimensional posterior distributions. Their analysis can include, e.g., determining the maximum-a-posteriori (MAP) vector $\boldsymbol{\theta}_{MAP}$, computing the mode of the distribution (location of the distribution peak), or the median (mean) ± confidence ranges around it. Here for the SED best fit, we use a model generated by the vector $\boldsymbol{\theta}_{MAP}$ of free parameters values that together maximize the likelihood. Derived parameters (stellar mass, M_{star}, dust mass, M_{dust}, SFR, and metallicity) are median values of their posterior PDFs. These posteriors are not modeled directly, but rather computed from the full sample of SEDs produced in the MCMC run. Uncertainties are then inferred by computing the ±1σ confidence ranges around the median values. A_V and A_{FUV} are the ratios, at the respective wavelengths, of attenuated to unattenuated light. We run MCMC twice for every galaxy, once with the NSS and NSD model hypercubes. The best-fit model is then chosen between the NSS and NSD libraries according to the lowest rms residual.

2.3. MAGPHYS

MAGPHYS[5] is an analysis tool to fit multiwavelength SEDs of galaxies (da Cunha et al. 2008). Based on a Bayesian approach, the median PDFs of a set of physical parameters characterising the stars and dust in a galaxy are derived. The emission of stars is modeled using Bruzual & Charlot (2003) SSP models, assuming a Chabrier (2003) IMF. An analytic prescription of the SFH is coupled with randomly superimposed bursts to approximate realistic SFHs. More specifically, the exponentially declining SFH model is parametrized as SFR$(t) \propto \exp(-\gamma t)$, characterized by an age t_{gal} of the galaxy and star formation time-scale γ^{-1}.

---

[4] http://adlibitum.oats.inaf.it/silva/grasil/grasil.html

[5] http://www.iap.fr/magphys/

Throughout the galaxy's lifetime, random bursts are set to occur with equal probability at all times, with an amplitude defined by the stellar mass ratios in the burst and the exponentially declining component. The SFR is assumed to be constant throughout the burst with a duration of the bursts ranging between 30 Myr and 300 Myr. The stellar metallicity Z_{star} is varied uniformly between 0.02 and $2\,Z_\odot$. The probability of random bursts is set so that half of the SFH templates in the stellar library have experienced a burst during the last 2 Gyr.

Dust attenuation is modeled using the two-phase model of Charlot & Fall (2000), which accounts for the increased level of attenuation of young stars (<10 Myr) that were born in dense molecular clouds. Thus, young stars experience obscuration from dust in their birth clouds and the ambient ISM while stars older than 10 Myr are attenuated only by the ambient ISM. Consequently, the attenuation of starlight is time dependent:

$$\hat{\tau}_\lambda = \begin{cases} \tau_\lambda^{BC} + \tau_\lambda^{ISM} & \text{for } t' \le t_0 \\ \tau_\lambda^{ISM} & \text{for } t' > t_0, \end{cases} \qquad (3)$$

where $\hat{\tau}_\lambda$ is the "effective" absorption optical depth of the stars at time t', and t_0 is defined to be 10^7 yr. The wavelength dependence of dust attenuation is modeled based on the following relations:

$$\begin{aligned} \tau_\lambda^{BC} &= (1-\mu)\,\hat{\tau}_V\,(\lambda/5500\text{A})^{-1.3} \\ \tau_\lambda^{ISM} &= \mu\,\hat{\tau}_V\,(\lambda/5500\text{A})^{-0.7}, \end{aligned} \qquad (4)$$

where μ is the fraction of the V-band optical depth contributed by the diffuse ISM (and thus $f_\mu \equiv 1-\mu$ is the fraction of obscuration in birth clouds, BC).

The total infrared luminosity is a combination of the infrared emission from birth clouds and the ambient ISM:

$$L_{\lambda,d}^{tot} = L_{\lambda,d}^{BC} + L_{\lambda,d}^{ISM}. \qquad (5)$$

The dust emission in birth clouds and the ambient ISM is modeled using a combination of dust-emission mechanisms: PAHs and hot+warm dust grains in birth clouds and similar dust species in the ambient ISM, but with an additional cold-dust component. As described in da Cunha et al. (2008), the hot grains consist of single-temperature modified black bodies (MBBs) with fixed temperatures; the warm and cold dust temperatures are allowed to vary, with cold dust temperatures between 10 K and 30 K (for ambient ISM only) and warm dust temperatures between 30 K and 70 K, using the extended dust libraries from Viaene et al. (2014). The opacity curves are assumed to be power laws, and different emissivity indices are assigned to the different dust components. All emission is assumed to be optically thin.

The prior for the parameter, f_μ, which sets the relative contribution of birth clouds and the ambient ISM, is assumed to be uniformly distributed between 0 and 1. A similar uniform distribution between 0 and 1 is assumed for the fractional contribution of warm dust emission to BC IR luminosity, ξ_W^{BC}, in birth clouds. For the ambient ISM, the fractional contribution of cold dust emission to the ISM IR luminosity, ξ_C^{ISM}, is assumed to be uniformly distributed between 0.5 and 1. The fractional contributions to the IR emission of the ambient ISM of PAHs (ξ_{PAH}^{ISM}), the hot MIR continuum (ξ_{MIR}^{ISM}), and warm grains (ξ_W^{ISM}) are fixed to average ratios with ξ_C^{ISM} for the Milky Way (for more details, see Table 1 and da Cunha et al. 2008). The dust temperatures for warm and cold dust grains are assumed to be uniformly distributed within their temperature ranges. To summarize, MAGPHYS has 6 free parameters (ξ_W^{BC}, ξ_{MIR}^{BC}, T_W^{BC}, ξ_C^{ISM}, T_C^{ISM}, T_W^{ISM}) to model the infrared SED emission, and 6 free

parameters (γ, t_{gal}, A, Z_{star}, μ, and $\hat{\tau}_V$) to model the stellar emission and dust attenuation.

By varying the star formation history, stellar metallicity and dust attenuation, a library of 50 000 stellar population models are generated. An additional set of 50 000 dust SED templates is generated with a range of dust temperatures and varying relative abundances for the various dust components. To link the stellar radiation that was absorbed by dust to the thermal dust emission, the code assumes a dust energy balance, namely the amount of stellar energy that is absorbed by dust is re-emitted in the infrared (with a 15% margin to allow for model uncertainties arising from geometry effects, etc.).

To derive the best fitting parameters in the model, the observed luminosities are compared to the luminosities of each model j and the goodness of each model fit is characterized by:

$$\chi_j^2 = \sum_i \left(\frac{L_\nu^i - w_j L_{\nu,j}^i}{\sigma_i} \right)^2, \qquad (6)$$

with the observed and model luminosities, L_ν^i and $L_{\nu,j}^i$, and observational uncertainties, σ_i in the ith waveband, and a model scaling factor, w_j, to minimise χ_j^2 for each model j. All models are convolved with the appropriate response curves prior to comparison with the observed fluxes for each filter. Under the assumption of Gaussian uncertainties (see above), the PDF for every parameter is derived by weighting a specific parameter value with the probability $\exp(-\chi_j^2/2)$ of every model j; the output model parameters correspond to the median of the PDF.

3. Comparison of SED models

The SED algorithms have been applied to the KINGFISH sample of 61 galaxies which have a wide range of multiwavelength photometric observational constraints. The fits have been performed independently, by different individuals, in order to avoid potential biases in the outcome. In the ideal case, the multiwavelength SED emission of a single galaxy is constrained by 32 photometric data points across the UV-to-submm wavelength range. We refer to Dale et al. (2017) for a detailed description of the data reduction and aperture photometry techniques used in each of those bands. Before fitting, the data from Dale et al. (2017) has been corrected for foreground Galactic extinction according to A_V measurements by Schlafly & Finkbeiner (2011) and the extinction curve of Draine (2003).

Not all KINGFISH galaxies have complete observational coverage, and some observations have resulted in non-detections (upper limits are not accounted for in the SED modeling), which results in an inhomogeneous data coverage for the entire sample of KINGFISH galaxies. While this inhomogeneity of photometric data points might bias the quantities derived from the SED modeling (e.g., Ciesla et al. 2014), the main interest of this paper is to compare the SED model output from the three different codes (which have been constrained by the same set of data). Any inhomogeneity in the photometric constraints for different galaxies will not affect the main goal of this work. Table 2 gives an overview of the filters and central wavelength of the wavebands used to constrain the SED models, and the number of galaxies for which measurements (detections or upper limits) are available (see also Dale et al. 2017). In all galaxies, the number of data points significantly exceeds the number of free parameters in the models.

Some of the filters also cover the same wavelength range (e.g., SDSS $ugriz$ and $BVRI$, MIPS and PACS) but show offsets

Table 2. Wavelength coverage for KINGFISH SEDs.

Filter	Wavelength (μm)	Number galaxies[a]
GALEX_FUV	0.152	57
GALEX_NUV	0.227	58
SDSS_u	0.354	40
B_Bessel	0.440	61
SDSS_g	0.477	40
V_Bessel	0.550	59
SDSS_r	0.623	40
R_Cousins	0.640	56
SDSS_i	0.762	40
I_Cousins	0.790	56
SDSS_z	0.913	40
2MASS_J	1.235	61
2MASS_H	1.662	61
2MASS_Ks	2.159	61
WISE_W1	3.353	59
IRAC_CH1	3.550	61
IRAC_CH2	4.490	61
WISE_W2	4.603	57
IRAC_CH3	5.730	61
IRAC_CH4	7.870	61
WISE_W3	11.561	61
WISE_W4[b]	22.088	54
MIPS_24	23.70	61
PACS_70	71.11	61
MIPS_70	71.42	61
PACS_100	101.20	61
MIPS_160	155.90	61
PACS_160	162.70	61
SPIRE_250	249.40	61
SPIRE_350	349.90	61
SPIRE_500	503.70	61
SCUBA_850	850.0	21

Notes. [a]These numbers give the sum of the detections and upper limits. [b]Shifting this effective wavelength to the modified value given by Brown et al. (2014a) would bring the WISE W4 and MIPS 24 μm fluxes into closer agreement.

in their absolute photometry. To avoid preferentially biasing any individual source of photometry, we have opted to use all available photometric constraints available for every single galaxy. As long as there is no preferred spectral region in the models, the relative comparison of the SED output quantities should not be strongly affected by inconsistencies of flux measurements at similar wavelengths.

In the remainder of this section, we compare the SED results from the three different codes. First, we assess the capability of the model to reproduce the *shape* of the data SED (Sect. 3.1); then, we confront fitted results against an independently-derived set of "reference" or recipe quantities (Sect. 3.2).

3.1. Comparison of SED shapes

The best-fit[6] SEDs for all three models are overlaid on the observed SED for a representative KINGFISH galaxy

---

[6] Unlike the derived quantities from the inferred SED (that are mean of the PDF for CIGALE, and median of the PDF for GRASIL and MAGPHYS), these are the maximum-likelihood solutions.

(NGC 5457 = M 101) in Fig. 1, and for the remaining galaxies in Fig. A.1. We have assessed the quality of the three SED-fitting algorithms using three criteria: reduced χ^2, χ_ν^2; the root-mean-square residuals in logarithmic space (i.e., log(flux)), rms; and the weighted root-mean-square residuals rms_w. Figure 2 shows the comparison of the rms values; the rms is calculated as the square root of the mean of the sum of squares. All algorithms provide quite good approximations of the observed SED across all wavelengths, typically with rms $\lesssim 0.08$ dex; such values are typical of the uncertainties in the fluxes themselves (see Dale et al. 2017). Interestingly, the outliers with large rms for CIGALE and GRASIL are not the same galaxies; CIGALE has more problems with dwarf galaxies (e.g., DDO 053, IC 2574, NGC 5408) while GRASIL struggles with early types (e.g., NGC 584, NGC 1316, NGC 4594).

In the optical and FIR-to-submm wavelength domains, the three SED models show similar SED shapes. Despite the different SFH prescriptions for the three codes, the SED models are all able to reproduce the stellar emission of intermediate-aged and old stars in the KINGFISH galaxies. Also the emission of the colder dust components in the models seems to agree well with a similar slope for the Rayleigh-Jeans tail of the SED in all three models. This is not surprising because the average FIR-submm dust emissivity indices of the three models are very close: $\beta = 2.08$ (Bianchi 2013) for the Draine & Li (2007, hereafter DL07) dust model used in CIGALE; $\beta = 2.02$ (see Sect. 3.3.3) for the Laor & Draine (1993) dust used in GRASIL; and $\beta = 2$ assumed for the cold dust component in MAGPHYS. The KINGFISH galaxies without observational constraints at FIR wavelengths (e.g., DDO 154 and DDO 165) show strong variations in their fitted dust SEDs, indicating that dust energy balance models cannot constrain the dust component in galaxies based only on UV and optical information on the dust extinction.

In the UV and FIR wavelength domains, the three models are also generally in good agreement, although for some galaxies GRASIL overestimates the observed UV emission. However, the predictions of the three models sometimes differ significantly at NIR and MIR wavelengths. Since MAGPHYS applies a fixed PAH emission template for their models (see Table 1), the relative changes in PAH abundance are not always reflected in the best-fit model (e.g., NGC 3190). Several galaxies show little or no PAH emission in their *Spitzer*/IRS spectra (e.g., Ho II, NGC 1266, NGC 1377, NGC 2841, NGC 4594: Roussel et al. 2006; Smith et al. 2007), but have significant PAH emission modeled by CIGALE and MAGPHYS. A detailed study of the PAH emission in NGC 1377 has shown that it is suppressed by dust that is optically thick at $\sim 10\,\mu$m (Roussel et al. 2006). On the other hand, the strong PAH features in some galaxy spectra observed with IRS (e.g., NGC 3190, NGC 3521, NGC 4569: Smith et al. 2007) are not reproduced by GRASIL. PAH emission in galaxies seems to be a source of significant disagreement among the models, and the models in many cases are unable to adequately approximate the detailed shape of the emission features.

At MIR wavelengths, there are also some continuum variations among the three different models. Ciesla et al. (2014) have already shown that MIR photometry is required to constrain the emission of warmer dust in SED models. But even with the MIPS 24 μm data point, the shape of the three SED models between 24 μm and 70 μm can be very different. The MAGPHYS models tend to have a bump in their SED shape in between 24 μm and 70 μm for some galaxies (e.g., NGC 3773, NGC 4236), possibly due to the addition of a warm component unconstrained by data. GRASIL shows a more constant SED slope at those
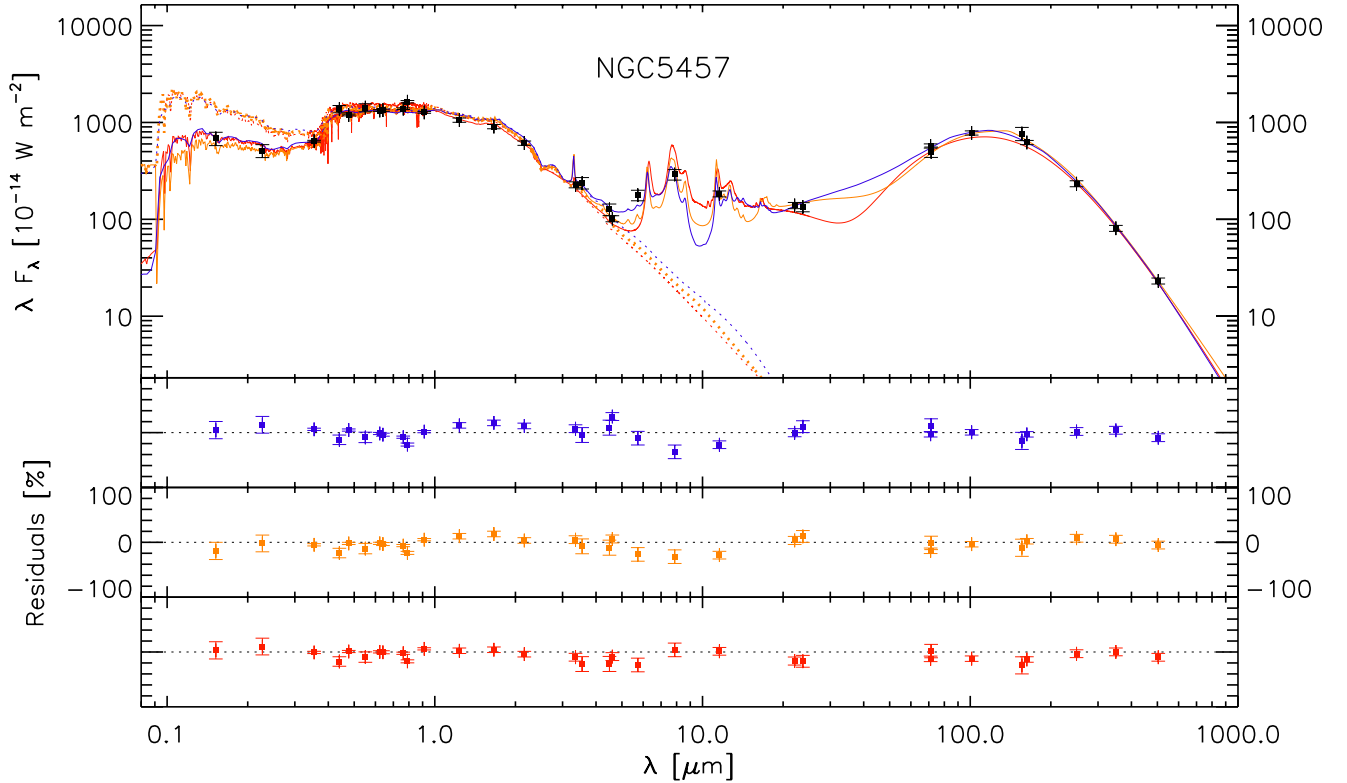
Fig. 1. Panchromatic SED for NGC 5457 (M 101) based on the photometry measurements from Dale et al. (2017) overlaid with the best-fitting SED model inferred from the SED fitting tools MAGPHYS (red curve), CIGALE (dark-orange curve) and GRASIL (blue curve). The dashed curves represent the (unattenuated) intrinsic model emission for each SED fitting method (using the same color coding). The bottom part of each panel shows the residuals for each of these models compared to the observed fluxes in each waveband.
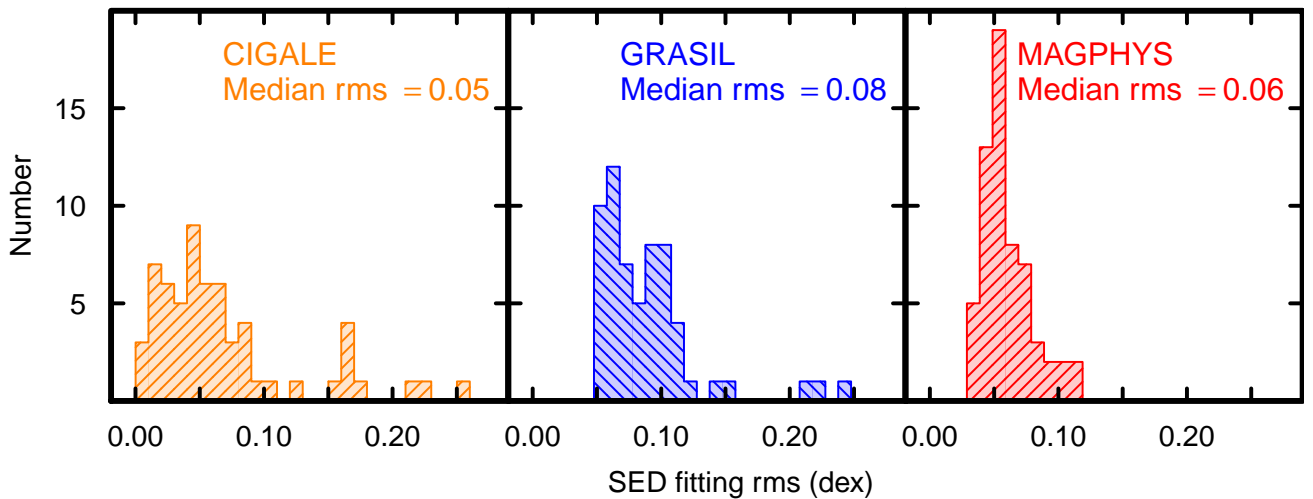

Fig. 2. Distribution of the root-mean-square residuals for the three SED-fitting algorithms, CIGALE, GRASIL, MAGPHYS. The rms is calculated as the square root of the mean of the sum of squares; the values are comparable to the typical uncertainty in the fluxes themselves.

wavelengths, while there is typically a small dip in emission in the CIGALE models; this dip can cause difficulties in fitting the mid- and far-IR emission of some galaxies (e.g., NGC 5408).

The changing behavior of the models in the MIR regime is illustrated in Fig. 3 where we show the $40\,\mu$m residuals ($(f_{\mathrm{Interpolated}} - f_{\mathrm{Model}})/f_{\mathrm{Model}}$) calculated by linearly interpolating the observed flux between $24\,\mu$m and $70\,\mu$m. MAGPHYS tends to overestimate the interpolated $40\,\mu$m emission (by median ~13%, but with large spread), while CIGALE underestimates the emission (~71%); GRASIL also underestimates but by less ($\lesssim$11%).

Although it is tempting to assume that small differences mean an accurate model, the true shape of the SED in this wavelength region is highly uncertain. Our linear interpolation is only providing a "fiducial" against which to compare the models; here our aim is to compare the different models with a common reference, rather than infer "truth".

Wu et al. (2010) show that over a wide range of IR luminosities, ratios of the $70\,\mu$m and $24\,\mu$m fluxes can vary by a factor of 5, and the variations seem to depend on the flux ratios at shorter wavelengths. Indeed, for MAGPHYS, the flux ratio between MIPS
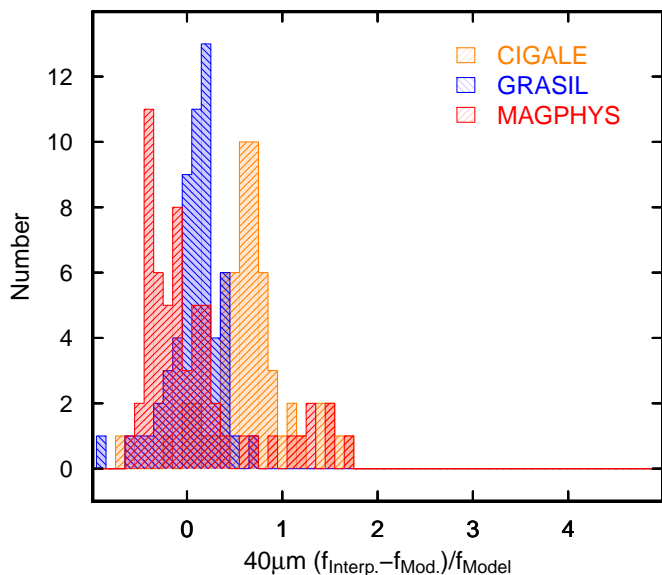
Fig. 3. Distributions of the residuals, $(f_{Interpolated} - f_{Model})/f_{Model}$, at $\sim 40\,\mu m$ for the three SED-fitting algorithms, `CIGALE`, `GRASIL`, `MAGPHYS`. As noted in the legend, `CIGALE` residuals are shown in dark orange, `GRASIL` in blue, and `MAGPHYS` in red.

$24\,\mu m$ (or WISE $22\,\mu m$) and the $12\,\mu m$ WISE band seems to play a role; if high, then the model wants to include more warm dust resulting in a $40\,\mu m$ "bump". For `CIGALE`, the power-law index α governing the variation of the ISRF U, is important; increasing α to 2.5 results in an increase in $40\,\mu m$ flux of 30%, not enough to compensate completely, but bringing the models closer to the observations. Finally, `GRASIL` seems to do a decent job of reproducing the observations, except in one highly discrepant galaxy; for NGC 4594 (the Sombrero), `GRASIL`'s estimate of the $24\,\mu m$ flux ($f_\nu(24)$) is lower than the observations by a factor of 4. `GRASIL` underestimates the diffuse dust component that is responsible for the mid-IR emission, possibly as a consequence of the geometry of this galaxy; the best `GRASIL` fit is for a spheroid, but the dust in the Sombrero is found in a conspicuous dust lane.

3.2. Reference quantities for comparison

To compare the three different SED models, we have devised a set of six quantities representative of a galaxy's general properties that will be used to quantify any model deviations. As fundamental quantities descriptive of galaxies, we have opted to compare stellar mass (M_{star}), star formation rate (SFR), dust mass (M_{dust}), total-infrared luminosity (L_{TIR}), intrinsic (dust-corrected) far-ultraviolet (FUV) luminosity (L_{FUV}) and FUV attenuation (A_{FUV}). M_{star}, SFR, and M_{dust} are quantities directly output by `CIGALE` and `MAGPHYS`; for `MAGPHYS` they are derived as the median values of the PDFs based on Bayesian statistics for the derived model quantities, while for `CIGALE`, they are the means (see Sect. 2). For `GRASIL`, the marginalized posteriors of the model parameters SFH and age of the galaxy t_{gal} are output (together with the other fitted parameters, see Table 1); M_{star}, SFR, and M_{dust} are not directly fit, but rather obtained from the medians of the PDFs allowed by the PDFs and confidence levels of SFH and t_{gal}. For `CIGALE`, L_{TIR}, L_{FUV}, and A_{FUV} are computed in the same way as the other quantities, from the likelihood-weighted means. For `GRASIL` and `MAGPHYS`, the luminosities and A_{FUV} are derived from a convolution (with

the appropriate response curves) and integration of the best-fit (maximum likelihood) model SED. Attenuation is inferred at a given wavelength through the ratio of intrinsic to observed (attenuated) emission.

For an independent measure of these six "fundamental" galaxy quantities, we have computed estimates using recipes based on one or two photometric bands (with the exception of the updated DL07 models for M_{dust} also included in the analysis). The methodology for these derivations is described in detail in Appendix B and summarized in Table B.1; the resulting values are reported in Table B.2. We emphasize that the quantities calculated by these recipes are almost certainly not the truth, but rather "poor-person" estimates, necessary when multiwavelength coverage is missing. The problem is that truth is unknown and here elusive. It could be reflected by one or more of the SED algorithms that certainly do better than the simple recipes based on a restricted photometric regime; it is almost certainly not reflected by these recipes since the whole idea of fitting SEDs is to improve our understanding of these parameters and their interrelation. The following sections attempt to maintain this philosophy.

### 3.3. SED model derived quantities compared

Here we perform linear regressions on the results from the three SED codes with respect to the derived recipe quantities. In principle, such an analysis will give insight as to the relative performance of the codes, but more importantly will enable an independent assessment of the accuracy of the reference quantities that are in truth simplified recipes that cannot be as accurate as a complete multiwavelength SED fitting. We calculated the regressions using a "robust" estimator (see Li 2006; Fox 2008), as implemented in the R statistical package[7]. In Figs. 4–8, the best-fit correlations are indicated with solid lines. Table 3 gives the results of the correlation analysis for the comparison of the results of the SED modeling and the reference recipe values; the normalizations for M_{star}, M_{dust}, L_{TIR}, and L_{FUV} for both axes are non-zero because otherwise the non-unit slopes would exaggerate the deviations for small x values. A discussion of results and disagreements is given in Sect. 4.

3.3.1. Comparison of stellar masses

The comparison of the SED results with the stellar masses determined from two IRAC-based independent methods (see Appendix B.1) is illustrated in Fig. 4. There is good agreement between the values of M_{star} inferred from SED fitting and M_{star} from both methods based on $3.6\,\mu m$ luminosities; the rms deviations are between 0.12 and 0.19 dex for the Wen et al. (2013) method with a luminosity-dependent Υ_* (mass-to-light ratio, M/L), and between 0.12 to 0.22 dex for constant Υ_*. However, both the Wen et al. (2013) luminosity-dependent Υ_* and the constant Υ_* (McGaugh & Schombert 2014) formulations overestimate M_{star} relative to the SED fitting algorithms: the discrepancy is ~ 0.1–0.3 dex for the former, and ~ 0.3–0.5 dex for the latter. For constant Υ_*, the deviation seems to depend on M_{star}, since the power-law slopes are generally significantly greater than unity. These discrepancies are larger than the rms deviations (see Table 3), and may be telling us something about the limitations of the assumption of constant Υ_* even at $3.6\,\mu m$ (e.g., Eskew et al. 2012; Norris et al. 2014). A new formulation

---
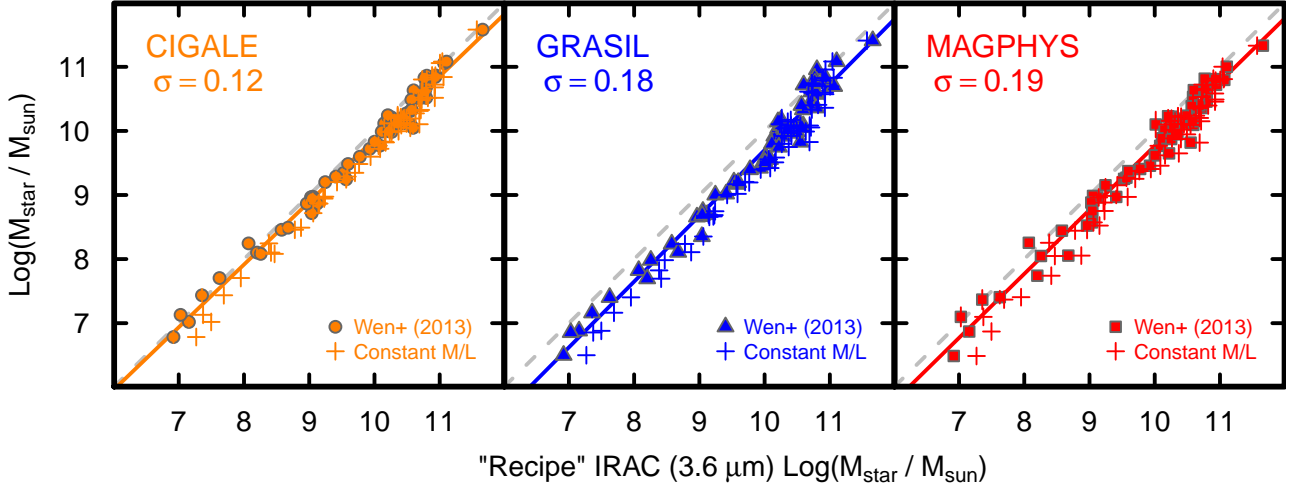
Fig. 4. SED-derived M_{star} plotted vs. independently determined M_{star} from the recipe IRAC 3.6 μm luminosities (see Sect. 3.3.1 for details). The Wen et al. (2013) M_{star} values are shown by filled (dark-orange) circles (CIGALE), filled (blue) triangles (GRASIL), and filled (red) squares (MAGPHYS), and the constant M/L ones by +; the σ values shown in the upper left corner of each panel correspond to the mean deviations from the fit of M_{star} with the Wen et al. (2013) method (see Table 3). Similarly, SED-fitting uncertainties are shown as vertical lines only for the Wen et al. (2013) x values, and are usually smaller than the symbol size. The robust correlation relative to the Wen et al. (2013) values is shown as a solid line, and the identity relation by a (gray) dashed one.
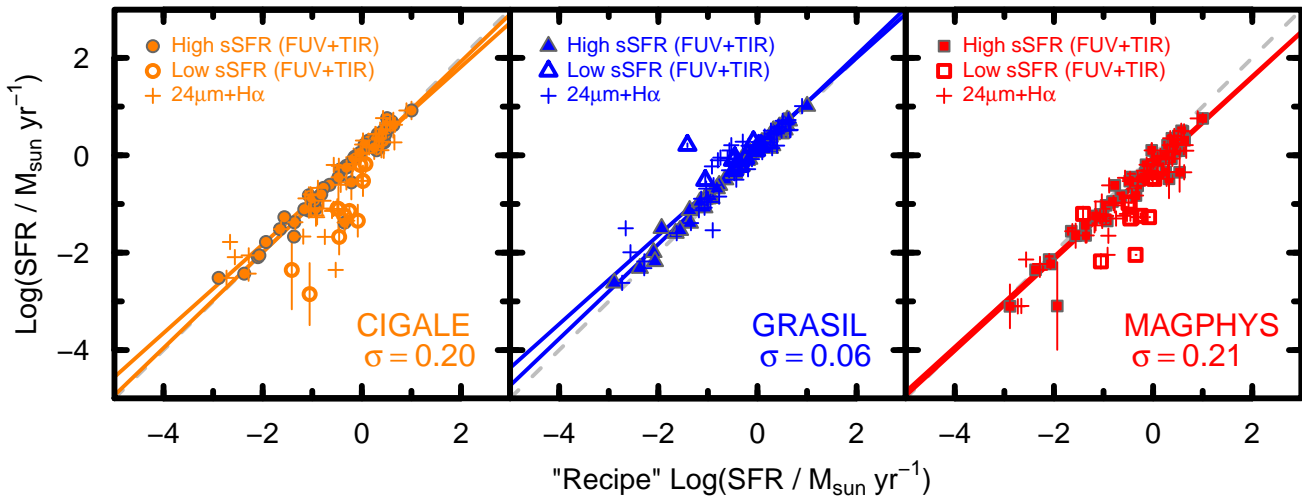
Fig. 5. SED-derived SFR plotted vs. independently determined recipe SFR (see Sect. 3.3.2 for details). Two different SFR tracers are shown: FUV+TIR and Hα+24μm luminosity; see Appendix B for details. Symbols (dark-orange circles for CIGALE, blue triangles for GRASIL, and red squares for MAGPHYS) are calculated with SFR(FUV+TIR); plus signs show the recipe SFR(Hα+24μm) luminosity. Filled symbols correspond to "high" specific SFR (Log(sSFR/yr^{-1}) > −10.6), and open ones to "low" specific SFR (Log(sSFR/yr^{-1}) ≤ −10.6, calculated with SFR(FUV+TIR). The robust correlations are shown as solid lines, and the identity relation by a (gray) dashed one; in each panel, the steeper power-law slope corresponds to the fit to SFR(FUV+TIR) and the shallower one to SFR(Hα+24μm) (see Table 3 for details). The rms deviations for the fit of SED-derived quantities vs. the reference ones (for SFR(FUV+TIR)) are shown by the σ value in the lower right corner of each panel; similarly, SED-fitting uncertainties are shown as vertical lines only for SFR(FUV+TIR) x values. rms deviations for SFR(Hα+24μm) are 0.25 dex, 0.18 dex, and 0.26 dex for CIGALE, GRASIL, and MAGPHYS, respectively (see Table 3).

based on our SED-fitting results for converting 3.4−3.6 μm luminosities into stellar masses is discussed in Sect. 5.4.

3.3.2. Comparison of star-formation rates

SED fitting typically gives more than one value of SFR; here we have compared the SED SFR averaged over the last 100 Myr with our two choices of reference hybrid SFRs estimated from FUV+TIR luminosities and Hα+24 μm luminosities (see Appendix B.2). The (robust) regression parameters are reported in Table 3 as before, and the comparisons of SED-inferred SFRs with reference ones are shown in Fig. 5.

For CIGALE and MAGPHYS, the agreement with SED fitting and independently-derived SFRs is slightly worse than with M_{star}; mean deviations are ∼0.2 dex, and there are several galaxies for which reference values are much higher than the SED-derived values. On the other hand, GRASIL SFRs are relatively close to the reference values, with the exception of NGC 1404, an early-type galaxy for which the recipe SFR is roughly 10 times lower than the GRASIL prediction; there are no FIR detections for this galaxy so SFR is not as well constrained as with IR data.

Because SFRs are a sensitive function of SFH, it is possible that some of the SED fitting algorithms are unable to identify
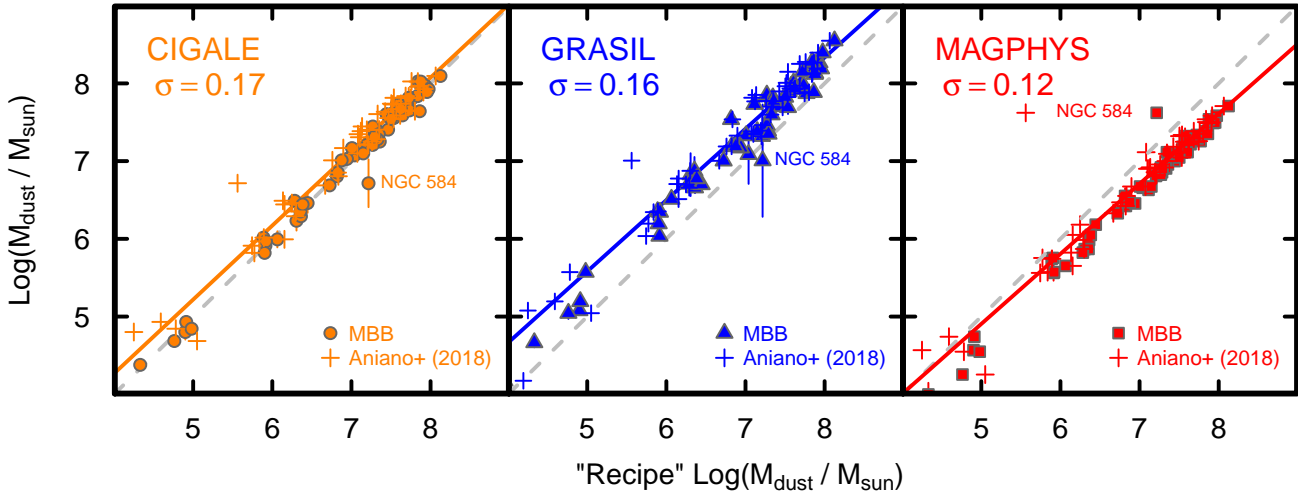
Fig. 6. SED-derived M_{dust} plotted vs. independently determined M_{dust} (see Sect. 3.3.3 for details). The identity relation by a (gray) dashed lines, and the robust correlation relative to the DL07 values is shown as a solid line; the mean deviations for the fit of SED-derived quantities vs. those using DL07 are shown by the σ value in the upper left corner of each panel. SED-fitting uncertainties are shown as vertical lines only for MBB x values.

the most suitable SFH because of degeneracies; similarly good SED fits may be obtained with a variety of different SFHs. Virtually all of the deviant galaxies for `CIGALE` and `MAGPHYS` are early types and/or lenticulars with low levels of specific SFR (sSFR = SFR/M_{star}) where the FUV may be indicating older stellar populations rather than young stars (e.g., Rich et al. 2005). However, SFR($H\alpha+L_{24}$) also shows a discrepancy relative to the fitting algorithms, although the scatter is slightly larger than for SFR(FUV+TIR) (see Table 3). This discrepancy could also be due to the SFR we chose for comparison, namely the 100 Myr average; because of timescales, this estimate is expected to be more consistent with FUV+TIR than with $H\alpha+L_{24}$.

As noticed by Schiminovich et al. (2007), it is very difficult to probe star formation at levels below sSFR $\lesssim 10^{-12}\,\mathrm{yr}^{-1}$, and there are four KINGFISH galaxies with sSFRs at roughly this level (NGC 1404, NGC 584, NGC 1316, NGC 4594). The problem of tracing SFR in low-sSFR (mainly early-type) galaxies will be discussed further in Sect. 4.2.

### 3.3.3. Comparison of dust masses

As shown in Fig. 6, the single-temperature modified blackbody (MBB) dust masses estimated from the updated *Herschel* photometry using the methods of Bianchi (2013, see Appendix B.3) are able to reproduce fairly well the SED models. The scatter is quite low with mean rms deviations between 0.06 and 0.15 dex (see Table 3), although dominated by early-type NGC 584, which is a problematic galaxy for all the codes (see also Fig. A.1). However, the MBB offsets are sometimes significant; MBB estimates for M_{dust} are generally higher than `MAGPHYS` estimates, and more so at high dust masses. Conversely, MBB estimates are below those of `GRASIL`, and more so at low masses. The MBB estimates (with the DL07 opacities) show the best agreement with the `CIGALE` models (based on the updated version of the DL07 models, Draine et al. 2014). The power-law slope of the comparison is consistent with unity (1.029 ± 0.01), and the mean offset is virtually zero (see Table 3), consistent with the rms deviations for `CIGALE` of ~0.10 dex.

The rms deviations of the DL07 (Aniano et al., in prep.) models compared to the SED fitting M_{dust} are higher than for

the MBB fits, ranging from 0.12 to 0.17 dex (shown in Fig. 6). The offset in the comparison of the DL07 models used here for `CIGALE` with the DL07 M_{dust} values given by Aniano et al. (in prep.) is consistent with the renormalization applied by those authors. This renormalization, based on the results by Planck Collaboration Int. XXIX (2016), lowers the DL07 dust mass by a small amount that depends on U_{min}, the minimum ISRF heating the dust. On average, this correction amounts to ~12% (see Table 3). The M_{dust} estimates of the different codes show similar behavior relative to the DL07 values by Aniano et al. (in prep.) as for the MBB values calculated here: namely `CIGALE` shows the best agreement, while the DL07 values are low compared to `GRASIL` and high compared to `MAGPHYS`.

We investigated whether discrepancies in M_{dust} between the `GRASIL` and `MAGPHYS` SED models and the reference dust estimates could be attributed to differences in the adopted dust opacity. The `MAGPHYS` models (da Cunha et al. 2008) assume a fiducial dust opacity at $850\,\mu m$ of $\kappa_{abs} = 0.77\,\mathrm{cm}^2\,\mathrm{g}^{-1}$ (Dunne et al. 2000), and a spectral index β of 1.5 or 2.0 for the warm and cold component, respectively. At $850\,\mu m$, the DL07 models have $\kappa_{abs} = 0.38\,\mathrm{cm}^2\,\mathrm{g}^{-1}$, roughly a factor of two lower than the value used by `MAGPHYS` (and ~1.5 times lower than the value at $850\,\mu m$ of the opacities of Laor & Draine 1993). Thus, the observed underestimate of $\lesssim 2$ would be consistent with the different assumed dust opacities of `MAGPHYS` relative to the DL07 values used by Bianchi (2013). However, the observed significant sub-unity slope (see Table 3), and the use of a flatter β according to the temperature of the dust, contribute to the discrepancy which increases with increasing M_{dust}.

`GRASIL` dust is based on the Laor & Draine (1993) opacity curves, which for the combined grain populations gives $\kappa_{abs} = 6.4\,\mathrm{cm}^2\,\mathrm{g}^{-1}$ at $250\,\mu m$, roughly 60% higher than the value of $\kappa_{abs} = 4.0\,\mathrm{cm}^2\,\mathrm{g}^{-1}$ used here (see Bianchi 2013), based on the dust models by DL07. This would imply that the `GRASIL` M_{dust} values should be underestimated by a factor of ~1.6 (~0.2 dex) relative to the MBB values, but, instead, they tend to be overestimated. Another difference between the DL07 models and the Laor & Draine (1993) dust used by `GRASIL` is the mean emissivity power-law index, β. If the DL07 opacities are fitted with a wavelength-dependent power law between 70 and $700\,\mu m$, the power-law index $\beta = 2.08$ (Bianchi 2013); for the
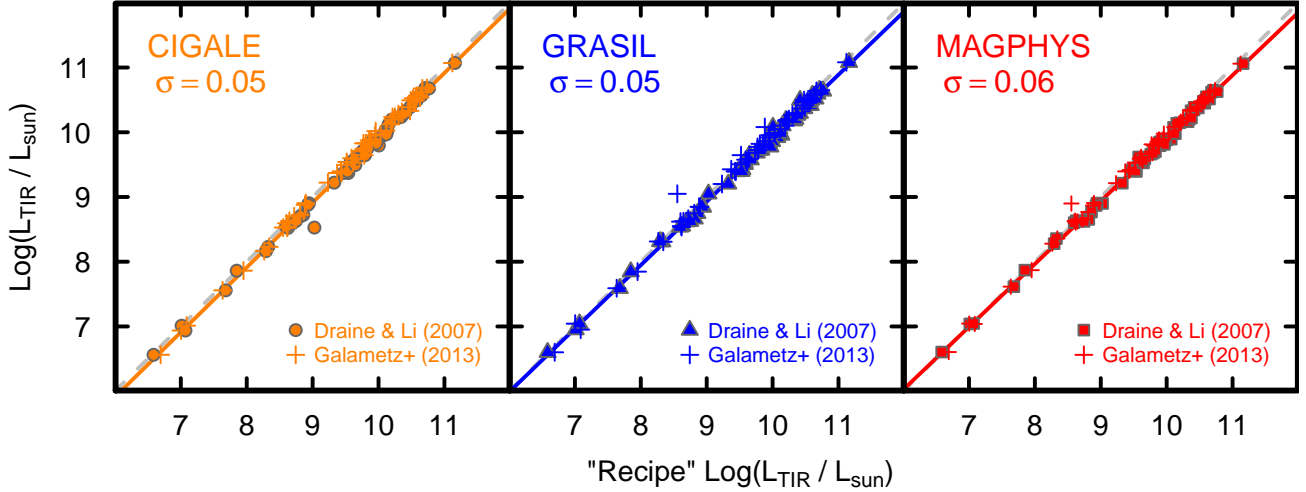
Fig. 7. SED-derived L_{TIR} plotted vs. independently determined L_{TIR} from *Spitzer* and *Herschel* photometric data (see Sect. 3.3.4 for details). In each panel, the DL07 L_{TIR} values are shown by filled circles (`CIGALE`), filled triangles (`GRASIL`), and filled squares (`MAGPHYS`), and those from Galametz et al. (2013) by +. The σ values shown in the upper left corner of each panel correspond to the mean deviations of the L_{TIR} fit with the DL07 values (see Table 3). The lines are as in Fig. 4, and SED-fitting uncertainties are shown as vertical lines only for the DL07 x values (but they are typically smaller than the symbol size).
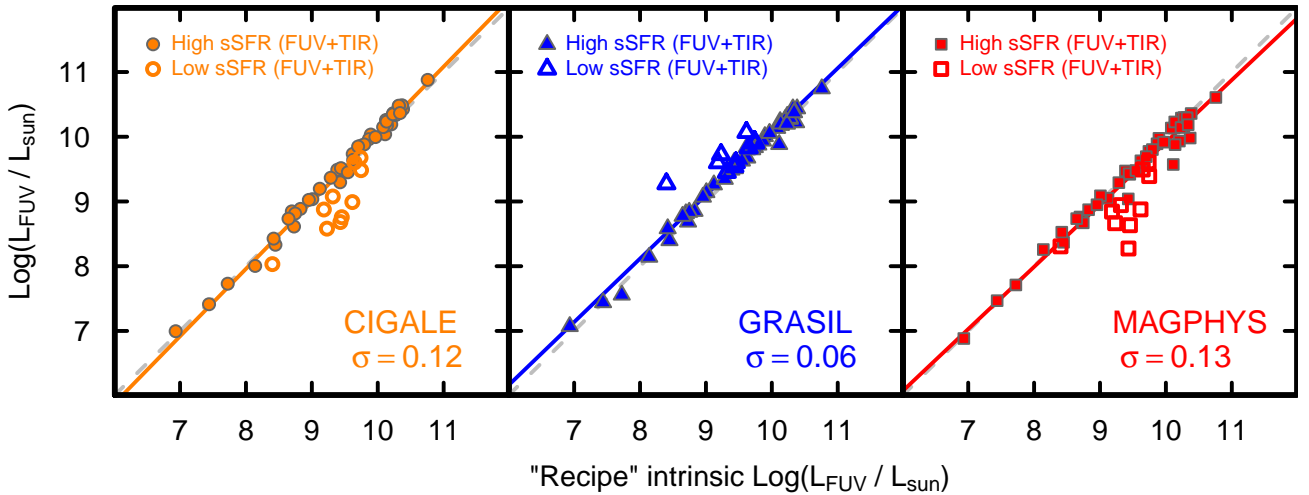
Fig. 8. SED-derived L_{FUV} plotted vs. independently determined L_{FUV} with extinction corrections derived from *Spitzer* and *Herschel* photometric data (see Sect. 3.3.4 for details). The σ values shown in the lower right corner of each panel correspond to the mean deviations of the L_{FUV} fit (see Table 3). The lines are as in Fig. 4. As in Fig. 5, filled symbols correspond to high specific SFR (Log(sSFR/yr^{-1}) > −10.6), and open ones to low specific SFR (Log(sSFR/yr^{-1}) ≤ −10.6), as noted in the legend in the upper left corners. This sSFR limit corresponds roughly to the lowest quartile in the KINGFISH galaxies, and also to the inflection in the SFMS by Salim et al. (2007).

Laor & Draine (1993) grains the fitted index over the same wavelength range is slightly smaller, $\beta = 2.02$. Although seemingly a minor difference, because most of the dust mass resides in the cooler dust that emits at longer wavelengths, and because the absolute emissivity at the fiducial wavelength is fixed, shallower β values cause an increase in the submm emission and thus, incrementally, lower estimated dust mass when matching to observed fluxes. Between 100 and 500 μm, this tiny difference in β causes an increase in fitted flux at longer wavelengths, and thus of M_{dust}, of ~10%; this could partially compensate the differences in adopted dust opacities.

However, the MBB fits (and the DL07 values from Aniano et al., in prep.) are lower than the `GRASIL` dust-mass estimates, contrary to what would be expected from the differences in opacities. It is interesting that the only one of the three SED models that includes realistic geometries of dust and stars generally

gives dust masses that are higher than the single-temperature MBB fits. It is possible that the true dust mass needed to shape the SED with the combined effects of dust extinction and emission is larger than what would be inferred from the simple MBB assumption (e.g., Dale & Helou 2002; Galliano et al. 2011; Magdis et al. 2012; Santini et al. 2014).

3.3.4. Comparison of luminosities and FUV attenuation

Figure 7 compares L_{TIR} derived from SED fitting with the two photometric formulations described in Appendix B.4: DL07 and Galametz et al. (2013, hereafter G13). L_{TIR} is the most robust parameter compared with SED fitting, with rms deviations relative to the analytical expressions between 0.03 and 0.06 dex. Nevertheless, both formulations slightly overestimate L_{TIR} relative to the SED models. Taking DL07 which relies

Table 3. Correlations of SED-derived vs. independently-derived recipe quantities: $y = a + b\,x$.

Quantity	x method	y method	Number galaxies	a	b	rms residual
$\mathrm{Log}[M_{\mathrm{star}}/10^9\,M_\odot]$	var M/L$_{3.6}$ (Wen + 2013)	CIGALE	61	-0.106 ± 0.02	0.979 ± 0.02	0.121
		GRASIL	61	-0.325 ± 0.03	1.026 ± 0.02	0.181
		MAGPHYS	61	-0.232 ± 0.03	0.999 ± 0.02	0.192
$\mathrm{Log}[M_{\mathrm{star}}/10^9\,M_\odot]$	fix M/L$_{3.6}$	CIGALE	61	-0.305 ± 0.02	1.046 ± 0.01	0.120
		GRASIL	61	-0.534 ± 0.04	1.102 ± 0.03	0.152
		MAGPHYS	61	-0.427 ± 0.03	1.071 ± 0.02	0.216
$\mathrm{Log}[\mathrm{SFR}/M_\odot\,\mathrm{yr}^{-1}]$	FUV+TIR/$M_\odot\,\mathrm{yr}^{-1}]$	CIGALE	61	-0.034 ± 0.03	0.981 ± 0.04	0.204
		GRASIL	61	0.117 ± 0.01	0.971 ± 0.01	0.065
		MAGPHYS	61	-0.277 ± 0.03	0.935 ± 0.03	0.206
$\mathrm{Log}[\mathrm{SFR}/M_\odot\,\mathrm{yr}^{-1}]$	Hα+24	CIGALE	60	-0.040 ± 0.04	0.957 ± 0.04	0.251
		GRASIL	60	0.125 ± 0.03	0.941 ± 0.03	0.186
		MAGPHYS	60	-0.274 ± 0.04	0.955 ± 0.04	0.256
$\mathrm{Log}[M_{\mathrm{dust}}/10^7\,M_\odot]$	MBB fit	CIGALE	58	0.018 ± 0.01	1.029 ± 0.01	0.103
		GRASIL	58	0.315 ± 0.02	0.991 ± 0.02	0.149
		MAGPHYS	58	-0.399 ± 0.01	0.974 ± 0.01	0.056
$\mathrm{Log}[M_{\mathrm{dust}}/10^7\,M_\odot]$	DL07 fit	CIGALE	54	0.123 ± 0.02	0.952 ± 0.02	0.173
		GRASIL	54	0.416 ± 0.03	0.917 ± 0.02	0.161
		MAGPHYS	54	-0.292 ± 0.02	0.901 ± 0.02	0.120
$\mathrm{Log}[L_{\mathrm{TIR}}/10^7\,L_\odot]$	DL07 formulation	CIGALE	58	-0.087 ± 0.01	1.001 ± 0.01	0.046
		GRASIL	58	-0.072 ± 0.01	0.981 ± 0.01	0.053
		MAGPHYS	58	-0.063 ± 0.01	0.972 ± 0.01	0.059
$\mathrm{Log}[L_{\mathrm{TIR}}/10^7\,L_\odot]$	GL13 formulation	CIGALE	58	-0.046 ± 0.01	1.014 ± 0.01	0.051
		GRASIL	58	-0.040 ± 0.01	0.995 ± 0.01	0.032
		MAGPHYS	58	-0.022 ± 0.01	0.983 ± 0.01	0.042
$\mathrm{Log}[L_{\mathrm{FUV}}/10^9\,L_\odot]$	IRX correction Murphy + (2011)	CIGALE	54	0.001 ± 0.02	1.041 ± 0.02	0.115
		GRASIL	54	0.098 ± 0.01	0.981 ± 0.01	0.060
		MAGPHYS	54	-0.048 ± 0.02	0.962 ± 0.03	0.127
A_{FUV}	Murphy + (2011)	CIGALE	54	0.181 ± 0.05	0.933 ± 0.02	0.218
		GRASIL	54	0.136 ± 0.04	0.852 ± 0.02	0.150
		MAGPHYS	54	0.211 ± 0.06	0.807 ± 0.03	0.210

only on *Spitzer* photometry, the discrepancy is ∼0.06–0.09 dex; the agreement is better for the G13 formulation which incorporates *Herschel* photometry (0.05 dex for CIGALE; 0.04 dex for GRASIL; 0.02 dex for MAGPHYS). The power-law slopes relative to both estimates of L_{TIR} are unity to within the uncertainties for all the SED models, with the possible exception of MAGPHYS (relative to DL07). Overall, the ultimate agreement with the SED-derived values is within 3–5% for G13 and within ∼6–9% for DL07.

The intrinsic FUV luminosities L_{FUV} from SED fitting and from the corrected observed luminosity are compared in Fig. 8. As described in Appendix B.4, we have derived the reference L_{FUV} by correcting observed FUV fluxes for attenuation using A_{FUV} calculated according to Murphy et al. (2011)[8]. Instead of FUV colors (e.g., Boquien et al. 2012), this correction relies on IRX, $\log_{10}$ of the ratio of L_{TIR} and L_{FUV} (e.g., Buat et al. 2005). As in previous figures, the open symbols in Fig. 8 correspond to low sSFR = SFR/M_{star} (Log(sSFR/yr^{-1}) ≤ −10.6), roughly the inflection or turnover point in the SFMS by Salim et al. (2007), and also approximately to the lowest quartile of the KINGFISH sample. L_{FUV} estimated by all the SED algorithms is very close to the photometric estimate using the Murphy et al. (2011) recipe for the extinction correction, with mean deviations

between ∼0.08–0.13 dex. Results are unchanged if we incorporate, instead, the recipe by Hao et al. (2011).

Interestingly, for the problematic early-type galaxy, NGC 584 (the discrepant open triangle in the middle panel of Fig. 8), the recipe L_{FUV} is much lower than the GRASIL estimate, while recipe L_{FUV} for galaxies with low sSFR tends to exceed the CIGALE and MAGPHYS values (see also Sect. 3.3.2). As discussed above, these discrepancies are almost certainly due to different approaches in associating a specific SFH with a given SED, and we will elaborate on this further in Sect. 4.

The SED models derive extinction at a given wavelength through the ratio of intrinsic to observed (attenuated) emission, while the reference A_{FUV} is derived through IRX rather than UV colors (see Appendix B.4). Figure 9 shows the comparison of the SED-derived A_{FUV} and A_{FUV} calculated according to Murphy et al. (2011). In all cases, there is a discrepancy between photometric and SED fitting results, with photometric A_{FUV} exceeding the SED A_{FUV} values with fairly large scatter, ∼0.2 dex. The discrepancy increases with increasing attenuation (see significant sub-unity slopes in Table 3), and can be ≳1 mag at high A_{FUV}. However, at low A_{FUV} (and low L_{FUV}, see above), the disagreements for CIGALE and MAGPHYS are apparently associated with low sSFR (shown by open symbols in Fig. 9). This association probably results from two potential problems with the usual (photometric) estimates of A_{FUV}: dust heating from longer-lived low-mass stars may contribute to

---

[8] Here we use L_{TIR} from the formulation of G13.
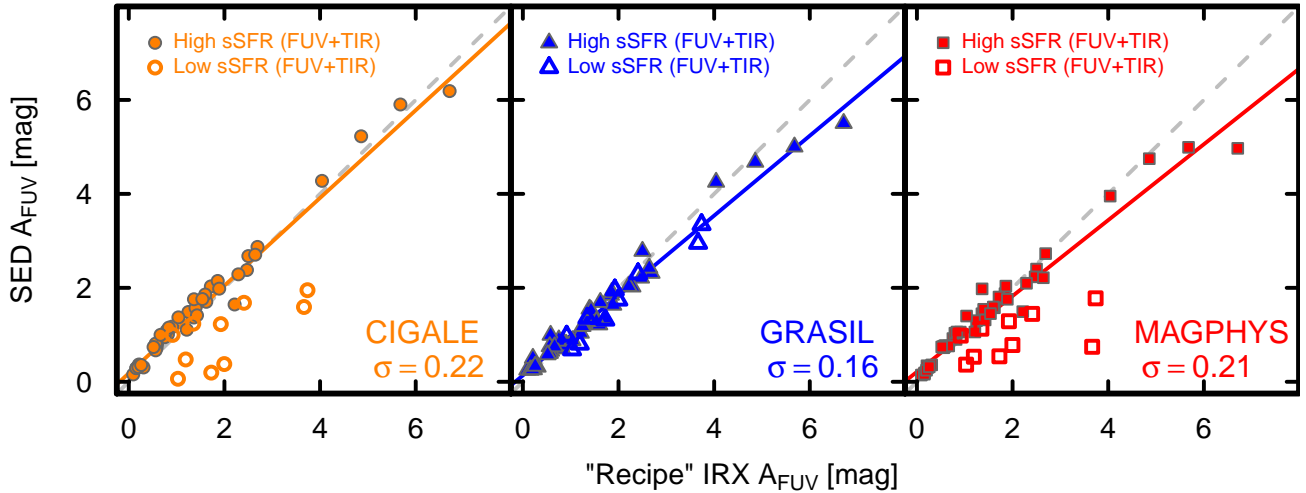
Fig. 9. SED-derived A_{FUV} plotted vs. A_{FUV} derived according to Murphy et al. (2011, see Sect. 3.3.4 for details). The lines are as in Fig. 4. The mean deviations for the fit of SED-derived A_{FUV} vs. A_{FUV} derived as in Murphy et al. (2011) are shown by the σ value in the lower right corner of each panel. As in Fig. 5, filled symbols correspond to high specific SFR (Log(sSFR/yr^{-1}) > −10.6), and open ones to low specific SFR (Log(sSFR/yr^{-1}) ≤ −10.6), as noted in the legend in the upper left corners.

IR emission and thus spuriously increase IRX causing A_{FUV} to be overestimated (e.g., Boquien et al. 2016). Conversely, FUV emission from post-Asymptotic Giant Branch (pAGB) stars may contribute to FUV luminosity and cause A_{FUV} to be underestimated. For GRASIL, these factors may also be problematic, but the disagreements are not so clearly associated with galaxies having low sSFR; we will discuss this point further below.

The shallower slope of A_{FUV} relative to the reference values common to all three codes may provide valuable input to the Murphy et al. (2011) or (equivalent) Hao et al. (2011) formulations:

$$A_{\text{FUV}} = 2.5 \log_{10}(1 + a_{\text{FUV}} \times 10^{\text{IRX}}), \qquad (7)$$

where a_{FUV} is a scale parameter, related to the fraction of the bolometric luminosity emitted in the FUV, η_{FUV} ($L_{\text{FUV}}(\text{cor}) = \eta_{\text{FUV}} L_{\text{bol}}$). The FUV optical depth τ_{FUV} (FUV attenuation in magnitudes $A_{\text{FUV}} = 1.086 \tau_{\text{FUV}}$) is defined by:

$$L_{\text{FUV}}(\text{obs}) = L_{\text{FUV}}(\text{cor}) e^{-\tau_{\text{FUV}}}, \qquad (8)$$

and the effective opacity of the dust-heating starlight $\bar{\tau}$:

$$L_{\text{TIR}} = L_{\text{bol}}(1 - e^{-\bar{\tau}}). \qquad (9)$$

where L_{bol} is the bolometric luminosity. As shown by Hao et al. (2011),

$$\tau_{\text{FUV}} = \ln\left[1 + \eta_{\text{FUV}} \frac{L_{\text{TIR}}}{L_{\text{FUV}}(\text{obs})} \frac{1 - e^{-\tau_{\text{FUV}}}}{1 - e^{-\bar{\tau}}}\right], \qquad (10)$$

implying that $a_{\text{FUV}} = \eta_{\text{FUV}}(1 - e^{-\tau_{\text{FUV}}})/(1 - e^{-\bar{\tau}})$ since IRX = $\log_{10}(L_{\text{TIR}}/L_{\text{FUV}}(\text{obs}))$.

Murphy et al. (2011) find $a_{\text{FUV}} = 0.43$ for the KINGFISH sample studied here, while Hao et al. (2011) find $a_{\text{FUV}} = 0.46$ for a similar sample. We have estimated new values of a_{FUV} for each of the SED algorithms by fitting Eq. (7) to the comparison of SED-derived A_{FUV} and the IRX values of the best-fit SED (using the L_{TIR} shown in the ordinate of Fig. 7 combined with "observed", extinguished, values of L_{FUV}, i.e., not the corrected values shown in the ordinate of Fig. 8). The fits have been performed using only galaxies with "high sSFR" (Log(sSFR/yr^{-1}) > −10.6).

Figure 10 shows the results of this exercise; the rms deviations of the fits given in each panel correspond to all the galaxies, including all values of sSFR. We find that CIGALE ($a_{\text{FUV}} = 0.59 \pm 0.02$) and GRASIL ($a_{\text{FUV}} = 0.52 \pm 0.02$) prefer higher values of a_{FUV}, while the best fit for MAGPHYS gives a lower value ($a_{\text{FUV}} = 0.40 \pm 0.02$). That a_{FUV} is generally larger than the recipe-derived value (0.43−0.46) is possibly counter-intuitive, given the sub-unity slope comparing SED- and recipe A_{FUV} seen in Fig. 9. However, the SED-derived IRX tend to be 0.1–0.2 dex smaller than the photometric values of IRX, and, except for GRASIL, are related with a super-unity power-law index; thus in some sense the effects compensate one another and result in a slightly larger a_{FUV}.

Although the extinction curve assumptions in CIGALE and MAGPHYS differ substantially from the geometry of stars and dust contemplated by GRASIL, the SED shapes of all three algorithms are well approximated by Eq. (7). Except for GRASIL, the scatter is large for galaxies with low sSFR, but the general agreement is encouraging, both because SEDs generated from diverse complex algorithms are consistent, and also because the simplistic photometric approach is a realistic approximation of galaxy SEDs, at least for the KINGFISH galaxies.

4. Impact of different model assumptions

In the previous section, we have compared results for fundamental quantities derived from SED fitting to those obtained from simpler methods (recipes). Sometimes the agreement both among the models and with the recipe quantities is excellent (e.g., L_{TIR}); in other cases, there are slight (M_{star}) or severe (A_{FUV}) discrepancies of the recipe parameter relative to all the models. Finally, there are some cases where a particular model is in closer agreement than others relative to the reference parameter. Some of this behavior may arise from the assumptions behind the photometric methods used to derive the reference values, which may or may not be also incorporated in the models (e.g., optically thin dust, FUV light from active star-forming stellar populations, etc.).

It is also true that SED fitting inherently suffers from degeneracies; a similar SED may emerge from radically different SFHs, while small variations of other parameters may cause
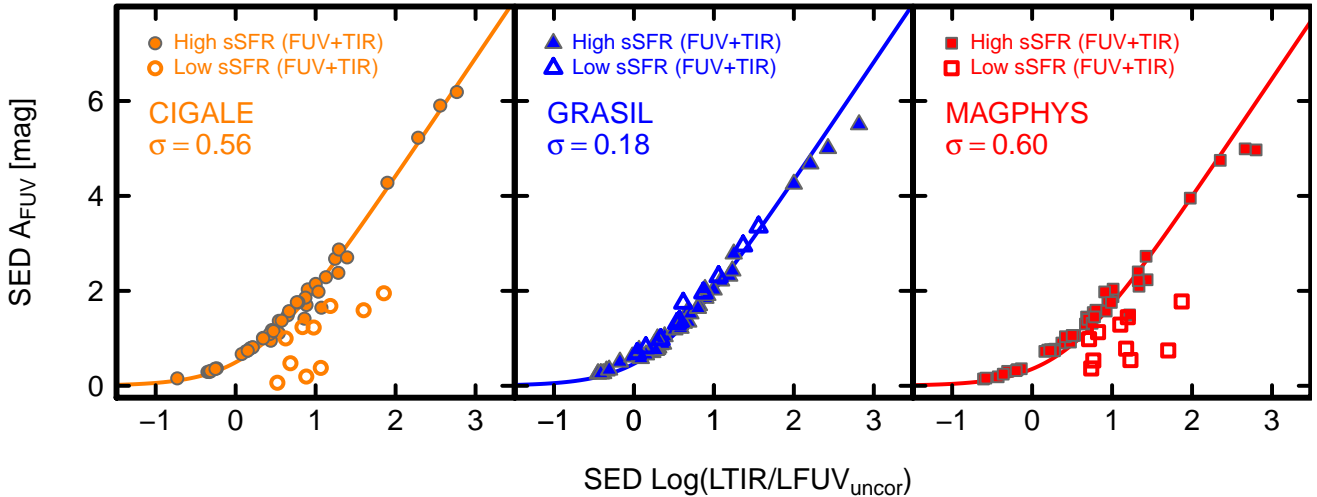
Fig. 10. SED-derived A_{FUV} plotted against SED-derived IRX [$\log_{10}(L_{TIR}/L_{FUV})$]. The solid curve shows the fit obtained by adopting the formulation in Eq. (7); as described in the text, the best-fitting a_{FUV} values are estimated using only the galaxies with (Log(sSFR/yr^{-1}) > −10.6). The mean deviations comparing the SED-derived A_{FUV} and the fitted ones from SED-derived IRX (now including all galaxies) are shown by the σ value in each panel. As in previous figures, filled symbols correspond to high specific SFR (Log(sSFR/yr^{-1}) > −10.6), and open ones to low specific SFR (Log(sSFR/yr^{-1}) ≤ −10.6), as noted in the legend in the upper left corners.

very different SEDs (e.g., the dust optical depth, see Takagi et al. 2003). In part, the inclusion of the IR regime helps to break the age-attenuation degeneracy inherent in optical SED fitting (e.g., Lotz et al. 2000; Lo Faro et al. 2013), distinguishing between dusty star-forming galaxies and evolved stellar populations (e.g., Pozzetti & Mannucci 2000). Nevertheless, it is important to examine how the different SED-fitting algorithms treat possible degeneracies in order to achieve the best-fit SED.

As pointed out by Michałowski et al. (2014), the scatter of SED-derived values is probably an inherent limit for the accuracy of SED models because of the necessary simplifications (e.g., galaxy geometry and the form of the dust-attenuation wavelength dependence). On the other hand, the quality of SED fitting is strongly affected by the set and quality of data at our disposal. Ultimately, the quantity and quality of the data are the defining factors in the reliability of SED-fitting models. Given the broad wavelength coverage and good quality of the KING-FISH photometry (Dale et al. 2017), we can assess differences in the results of SED fitting better than previously possible. Below we discuss some of the assumptions intrinsic to each of the SED models, and how these could impact the derived results.

4.1. Star-formation history, stellar mass, and SFR

Perhaps the most critical parameter in the SED fitting is the assumed SFH. All SED-fitting algorithms rely on a grid of SFHs, but which differ in their formulation (see Table 1). The version of CIGALE used here defines a "delayed" SFH at early times, with a step-like change of the SFR added at more recent times; MAGPHYS adopts an exponentially declining SFR with random bursts of SF activity superimposed uniformly over the lifetime of the galaxy. GRASIL approaches the problem from a different point of view, namely to model the timescale of gas inflow and leave as an additional free parameter the efficiency of the conversion of gas into stars; the age of the galaxy results from the best-fitting SED. These differences in SFH among the models propagate to differences between the photometric recipes and model-derived quantities.

It has been argued that a necessary ingredient for deriving accurate stellar masses at high redshift is a bi-modal SFH,

that is one with more than one episode of star formation (Michałowski et al. 2014). On the other hand, Lo Faro et al. (2013) find that most of the IR-luminous galaxies at $z \sim 1$−2 modeled with GRASIL do not require a two-component SFH. Conroy et al. (2010) analyzed the impact of SFH on the (UV-NIR) SED of simulated galaxies; the simulated galaxies were characterized by basically one star-formation episode each, but at different ages to distinguish passive from star-forming galaxies. CIGALE and MAGPHYS both have bi-modal SFHs, with one or more recent bursts of star formation superimposed on an older episode; however the GRASIL libraries we use here have only a single episode whose timescale and efficiency are fitted parameters.

Despite the different approaches to SFH, the three codes generally give similar stellar masses and even SFRs. Given that the three codes result in similar M_{star} values, it is likely that the three different recipes for SFH are equally effective for the nearby KINGFISH galaxies. Stellar populations for all codes are modeled with SSPs from Bruzual & Charlot (2003), and use the Chabrier (2003) IMF. As discussed in Sect. 3.3.1, the best agreement with SED-derived M_{star} and the reference M_{star} values is for the Wen et al. (2013) luminosity-dependent Υ_* formulation, rather than a constant Υ_* (e.g., McGaugh & Schombert 2014). The latter gives M_{star} that, on average, is 0.3–0.5 dex larger than derived from SED fitting, while the estimates using the luminosity-dependent Υ_* (Wen et al. 2013) tend to be ~0.1–0.3 dex too large.

Part of the discrepancy of the recipe M_{star} may be from the contribution of warm dust to the 3.6 μm continuum (Meidt et al. 2012, 2014), which we did not correct for here (although we do correct for nebular contamination, see Appendix B.1); nevertheless, globally, the warm-dust component is expected to be rather small, (~3–10%, Meidt et al. 2012) so probably cannot explain the systematic difference. In addition, our assumption that IRAC 3.6 μm and WISE W1 fluxes are the same may also be incorrect in some cases; however, judging from our own photometry, they cannot be more than a few percent discrepant. Stellar masses derived from SED fitting are almost certainly superior, when there is sufficient data coverage (here also IR). Moreover, the relatively good agreement among the codes suggests

that stellar masses can be consistently determined even under the rather different assumptions inherent to each of the models. Different formulations of SFH, SSPs, and extinction (see below) do not greatly affect the determinations of stellar mass, at least when IR data are included.

An important difference in the `CIGALE` modeling is that SFHs are included with a strong diminution of star formation in the recent past to allow for quenching (see also Ciesla et al. 2016). Thus it is possible to model passive galaxies now forming few to no stars at all. However, the characterization of a very low level of star formation is particularly difficult. A SFR of $10^{-7} M_\odot$ yr^{-1} will give an SED very similar to that obtained with an SFR of $10^{-3} M_\odot$ yr^{-1} as in either case, older stellar populations will contribute a large fraction of total dust heating. Indeed, for galaxies with sSFR $\lesssim 3 \times 10^{-11}$ yr^{-1} [Log(sSFR/ yr^{-1}) = -10.6], both `CIGALE` and `MAGPHYS` show differences in the estimates of SFR, $L_{\rm FUV}$, and $A_{\rm FUV}$ compared to empirical recipes and to `GRASIL`. The differences in inferred SFR are evident even when the recipe SFR tracer relies on Hα+24 μm, rather than FUV+TIR.

4.2. SFR estimates revisited to account for older stars

As discussed above, the codes incorporate different approaches to the parametrization of the SFH: `CIGALE` and `MAGPHYS` have a bi-modal SFH, while `GRASIL` relies on a single SF episode. As shown in Fig. 5, our choice of recipe SFR compares best with SED-derived values by `GRASIL` while, as mentioned above, `CIGALE` and to some extent also `MAGPHYS` underestimate SFR relative to the recipe for galaxies with low sSFR ($\lesssim 3 \times 10^{-11}$ yr^{-1}). This could be consistent with the idea that the smoother SFH of `GRASIL` (because of the one-component SFH) is closer to the constant SFR assumption of the recipe value. Indeed, Boquien et al. (2014) found evidence that the usual assumption of a constant SFH over 100 Myr can cause discrepancies of ∼25% on average compared to the true SFR.

On the other hand, SFRs in galaxies with low sSFRs are notoriously difficult to measure (e.g., Schiminovich et al. 2007; Temi et al. 2009a,b; Davis et al. 2014). Such galaxies are typically early types (ETGs), and the KINGFISH sample is no exception, even though there is not an exact one-to-one correspondence between Hubble type and sSFR. The UV upturn caused by extreme Horizontal Giant Branch stars can be an important component of UV flux in ETGs (e.g., Kaviraj et al. 2007). Also FUV and Hα may be produced by photoionization from old stars, in particular pAGBs (e.g., Binette et al. 1994). As pointed out by Sarzi et al. (2010), the ionizing continuum of pAGBs is not comparable to that of a single O-star, but their large numbers in ETGs make them the probable source of ionizing photons in this population.

The TIR component of the FUV+TIR SFR recipe is also potentially problematic because of a contribution from the low-mass evolved stellar population. This effect was noticed more than three decades ago with IRAS data, in which there was strong evidence for an increasing "cirrus" contamination in earlier Hubble types (Helou 1986; Sauvage & Thuan 1992). The problem with TIR estimates of SFR because of dust heating by older stars is now well established (e.g., Walterbos & Schwering 1987; Pérez-González et al. 2006; Kennicutt et al. 2009; Bendo et al. 2010, 2012; Leroy et al. 2012; Boquien et al. 2014; Hayward et al. 2014; De Looze et al. 2014; Herrera-Camus et al. 2015; Viaene et al. 2017). 24 μm luminosities, L_{24}, can also be affected by older stellar populations, but in this case the contamination is from AGB
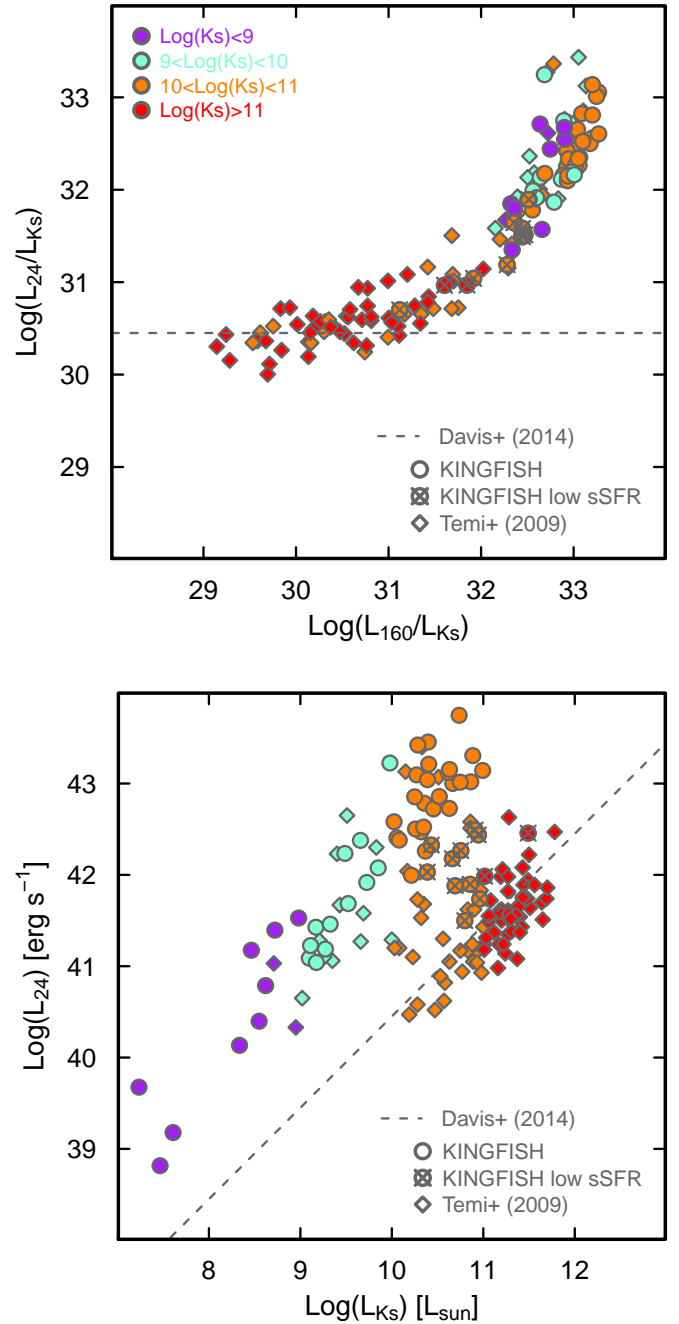
Fig. 11. *Upper panel*: log(L_{24}/L_{Ks}) vs. Log(L_{160}/L_{Ks}) luminosities of the KINGFISH galaxies (shown as filled circles), together with the sample of ETGs from Temi et al. (2009b) shown as filled diamonds. Following Temi et al. (2009a,b) and Davis et al. (2014), L_{Ks} luminosities are in units of $L_\odot$, and the IR luminosities in units of erg s^{-1}. KINGFISH galaxies with low sSFR (as in previous figures) are shown with a × superimposed. The color scale corresponds to bins of L_{Ks} as indicated in the *upper left* corner. The horizontal dashed line corresponds to the quiescent stellar ratio of L_{24}/L_{Ks} (Eq. (11)) as defined by Davis et al. (2014). It is evident that galaxies with low sSFR have L_{24}/L_{Ks} ratios close to the quiescent value. *Lower panel*: log(L_{24}) vs. Log(L_{Ks}) with the Davis et al. (2014) relation (Eq. (11)) shown as a dashed line. Symbols are the same as in the upper panel.

circumnuclear dust shells (e.g., Bressan et al. 1998, 2002; Verley et al. 2009).

Thus we are left with the difficulty for low sSFR galaxies of how to calculate SFRs that better reflect the truth in order to
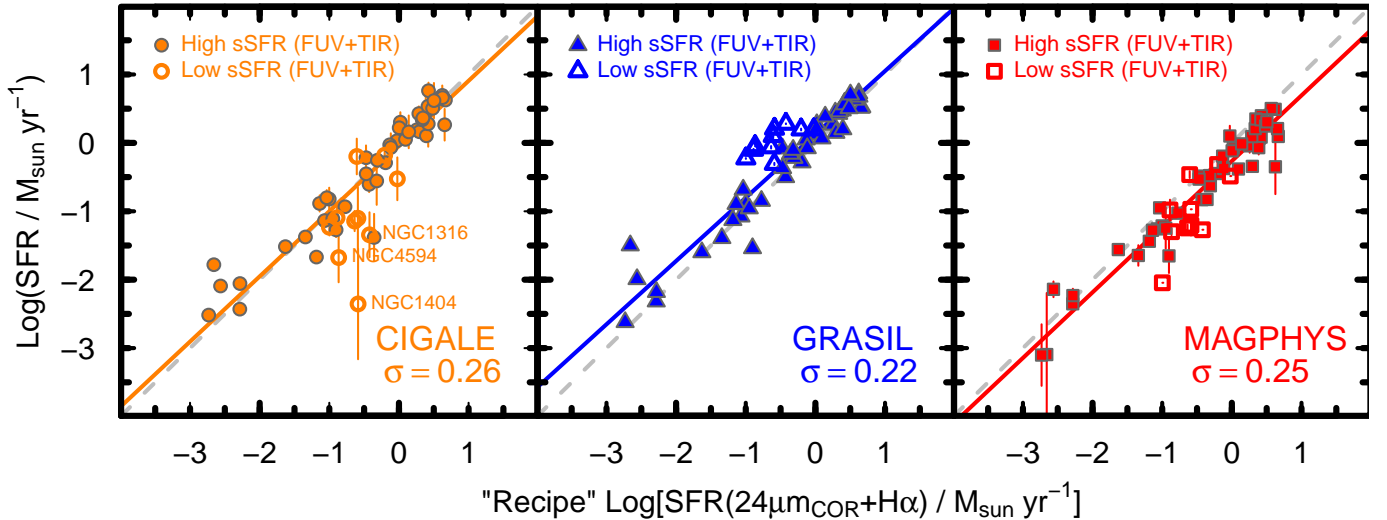
Fig. 12. SED-derived SFR plotted vs. SFRs determined from $L_{24\mu m,cor} + L_{H\alpha}$. As in previous figures, filled symbols correspond to high specific SFR, and open ones to low specific SFR (as calculated with SFR(FUV+TIR)). This figure is the same as Fig. 5, but here the SFRs from $H\alpha$+24 μm luminosities have been corrected as described in the text. The regression lines are as in Fig. 5; the mean deviations for the fit of SED-derived quantities vs. the recipe (for SFR($L_{24\mu m,cor} + L_{H\alpha}$)) are shown by the σ value in the lower right corner of each panel.

compare with SED results. Despite possible problems with $H\alpha$, Temi et al. (2009a,b) and Davis et al. (2014) advocate for ETGs the use of SFRs from $H\alpha$+24 μm luminosities after the stellar contribution to the 24 μm emission is subtracted; here we adopt this method and re-compute the SFRs for the KINGFISH sample. Following Temi et al. (2009b), we first calculated the L_{24}, L_{160}, and K_s-band luminosities[9], L_{Ks}, from the data in Dale et al. (2017). The ratios are shown in the upper panel of Fig. 11, where the quiescent stellar component of 24 μm emission (normalized to K band, see Davis et al. 2014) is plotted as a horizontal dashed line. It is clear that galaxies with low sSFR (the KINGFISH × symbols, and virtually all the galaxies from Temi et al. 2009b) have L_{24}/L_{Ks} ratios close to the quiescent stellar value. Figure 11 (lower panel) also illustrates the trend between L_{24} and L_{Ks}, emphasizing the clustering of the ETGs in Temi et al. (2009b) around the regression line.

To correct the 24 μm luminosities, we first need to subtract the quiescent component. This approach was first proposed by Temi et al. (2009b) who used the galaxies shown in Fig. 11 to calibrate the 24 μm emission from "passive" stars; Davis et al. (2014) applied the method to a different sample observed with the 22 μm WISE band (W4), and we use their calibration:

$$\log\left(\frac{L_{22\mu m,passive}}{erg\,s^{-1}}\right) = \log\left(\frac{L_{Ks}}{L_\odot}\right) + 30.45, \qquad (11)$$

with L_{22} ($\approx L_{24}$) in units of erg s^{-1} and L_{Ks} in $L_\odot$. The smaller constant (30.1) found by Temi et al. (2009b) is consistent with Eq. (11) given that their values of L_{Ks} are in the mean 0.29 ($\pm$0.08) dex larger than ours (and those in Davis et al. 2014); we have evaluated this offset using the 9 KINGFISH galaxies in common with Temi et al. (2009b). Since the Davis et al. (2014) analysis relied on W4, rather than on MIPS_24, we have also checked that this does not introduce an additional discrepancy; we find a difference between the KINGFISH 24 μm and 22 μm Log(fluxes) of -0.03 ± 0.06 dex, and thus assume equality. Once we have subtracted this quiescent stellar emission from

the observed L_{24} ($L_{24\mu m,cor} = L_{24\mu m,obs} - L_{24\mu m,passive}$) we recalculate the SFRs using the same approach as in Appendix B.2 for 24 μm+$H\alpha$, but now with the corrected $L_{24\mu m,cor}$.

This comparison is shown in Fig. 12 which is the same as Fig. 5 but with the 24 μm luminosities now corrected for stellar emission according to Eq. (11). The comparison is not significantly changed, and in fact is slightly worse; the rms deviation for the original SFR (uncorrected for stellar emission) inferred from $H\alpha$+24 μm is 0.25 dex, 0.19 dex, and 0.26 dex, for CIGALE, GRASIL, and MAGPHYS, respectively (see Table 3). For a few galaxies, CIGALE in particular seems to find lower SFRs than what would be expected with the new estimates[10]. For NGC 1404, the new photometric SFR (and previous 24 μm+$H\alpha$ estimate, see Table B.2) is almost certainly incorrect. The $H\alpha$ measurement (see also Skibba et al. 2011) comes from the "radial strip" flux by Moustakas et al. (2010), because there are no nuclear or circumnuclear fluxes, and the resulting $H\alpha$ luminosity is >5 times brighter than $0.02 L_{24\mu m,cor}$ that is the other term in the SFR calibration (see Appendix B.2). This seems unrealistic in such an ETG, so we do not consider this galaxy discrepant. The three remaining problematic galaxies are NGC 1316, NGC 4569, and NGC 4594, for which the new recipe SFR and the SED SFR by CIGALE differ by almost an order of magnitude. Both NGC 1316 (Fornax A) and NGC 4569 host an AGN, but the nuclear $H\alpha$ flux is ~8% and 24%, respectively, of the circumnuclear emission (Moustakas et al. 2010), so the AGN is not dominating the $H\alpha$ budget. The ratio of $L_{24\mu m,passive}/L_{24\mu m,obs}$ for NGC 1316 and NGC 4594 is ~30%, so not a huge correction; it is even smaller (~4%) in NGC 4569[11]. In all these galaxies the contribution from $H\alpha$ is 2–3 times lower than from 24 μm, so the reason for the discrepancy is not clear. However, it is likely that these early-type galaxies are in a "quenching" phase of their SFH, as discussed further in Sect. 5.1.

---

[9] We assume that the absolute magnitude of the Sun at K_s band is 3.28 mag (see Binney & Merrifield 1998; Davis et al. 2014).

[10] The most extreme deviant using SFR(FUV+TIR), NGC 584, as in Fig. 5 has no $H\alpha$ measurement, so we do not consider it further.

[11] NGC 4569 is not really an ETG, but rather an HI-deficient Virgo cluster galaxy suffering from gas removal by ram-pressure stripping (Boselli et al. 2016).

4.3. Extinction, dust emission, and geometry

Both `CIGALE` and `MAGPHYS` require an energy balance (see Table 1), namely that the fraction of stellar radiation absorbed by dust is re-emitted in the IR. In both cases (see Table 1 for details), the form of the interstellar attenuation curve used in the `CIGALE` and `MAGPHYS` models is unrelated to the dust emissivity, but rather relies on a two-component dust model (e.g., Calzetti et al. 2000; Charlot & Fall 2000) to account for the differential reddening between stellar populations of different ages. `MAGPHYS` uses a time-dependent attenuation law, while `CIGALE` lets vary some parameters of the shape of the attenuation curve, but neither account for radiation transfer. For `CIGALE`, dust emission is defined by the Draine & Li (2007) models, while for `MAGPHYS`, dust is divided into two components, birth clouds and the ambient ISM, and emission within these components is modeled as a combination of PAH templates and MBBs at different temperatures; the dust power-law emissivities are different for the various components, but with the same normalization at long wavelengths.

`GRASIL`, on the other hand, considers three components of stars and dust: stars embedded within GMCs, stars having already emerged from their birth clouds, and diffuse gas (+ cirrus-like dust). Previous incarnations of `GRASIL` included dust emission from circumstellar dust shells around AGBs as in Bressan et al. (1998, 2002), but here we use the Bruzual & Charlot (2003) stellar populations that are devoid of circumstellar dust. The geometry of each of these components is specified in the model, and radiative transfer is performed separately for each of the components assuming the Laor & Draine (1993) dust opacities/emissivities. Thus, for `GRASIL`, the effect of dust extinction is related, by definition, to dust emission because of the self-consistent definition of dust properties in the Laor & Draine (1993) dust opacity curve. `GRASIL` systematically gives higher M_{dust} relative to the other codes, and also to DL07 and MBB dust estimates. Because `GRASIL` also includes the cool dust that shines at longer wavelengths, necessary to produce the dust extinction, this component may add mass relative to the warmer luminosity-weighted dust emission that dominates the SED.

While one or another approach may be more valid for starbursts or high-z galaxy populations, the KINGFISH galaxies studied here are equally well fit by all three models. Thus, the assumption of optically thin dust, which obviates the need for radiative transfer, does not seem to be a problem for this sample in terms of estimating M_{dust}. This is because in these galaxies the bulk of the dust emits at longer wavelengths where the dust is optically thin, and because the long-wavelength dust emissivities adopted here are similar (see Sect. 3.3.3). Moreover, the three rather different attenuation curves also do not seem to introduce significant discrepancies in the SED shapes, possibly because any variations are compensated for by differences in A_{FUV}. Even though the assumptions made for dust attenuation and emission in each of the codes are quite different, in the end they lead to similar results, at least for the KINGFISH sample.

The difference of A_{FUV} predicted by the Murphy et al. (2011) or Hao et al. (2011) formulations and those of the SED models may also depend on the implicit assumptions. `CIGALE`, and `MAGPHYS` rely on attenuation curves whose fitted parameters account for geometry and extinction, while `GRASIL` takes into account the geometry of the dust and performs the radiative transfer. However, for all three models the estimated A_{FUV} tends to be smaller than that given following Hao et al. (2011).

This is not surprising for two reasons: the first is the geometry of the attenuating dust relative to the emission sources, and the second is the homogeneity of the medium. For a given dust column ($\propto \tau_{dust}$), a screen geometry would be expected to give larger attenuation relative to a mixed or more complex distribution of dust (Witt & Gordon 2000), so this could be one part of the explanation. Another part lies in the probable clumpiness of the dust distribution (e.g., Natta & Panagia 1984; Witt & Gordon 1996; Gordon et al. 2000). If the dust is not uniformly distributed within the absorbing region, then the optical depth inferred from SED modeling would be smaller than that derived by assuming a homogeneous medium as done by Hao et al. (2011). The homogeneous constant-density medium corresponds to the highest efficiency for dust attenuation given a specified dust mass (Witt & Gordon 1996). This effect is clearly seen in the three-dimensional radiative transfer models of M 51 by De Looze et al. (2014); the larger the fraction of dust mass in dense clumps, the lower the inferred A_{FUV}. Since `GRASIL` takes the dust distribution explicitly into account through geometry, this would explain the discrepancy in A_{FUV} relative to Murphy et al. (2011) or Hao et al. (2011). `CIGALE` and `MAGPHYS` also consider complex attenuation curves (see Sect. 2), and so implicitly also account for different dust distributions rather than homogeneous ones.

4.4. Metallicity

The `CIGALE` models used in this work adopt solar-metallicity SSPs, while `MAGPHYS` considers a range in metallicity for the SSPs (see Table 1). `GRASIL` instead models the metallicity evolution and gas content through CHE_EVO, and relates the dust mass necessary for the SED's best-fit shape to the hydrogen gas mass. Consequently, metallicity is varied also (albeit indirectly) in the `GRASIL` models, through its relation to the dust-to-gas mass ratio, assumed to vary linearly with metallicity[12]. Despite these significant differences in treatment of metallicity, there seem to be no salient differences in the quality of the SED shape relative to the observed SED. It is also true that the KINGFISH sample does not probe metallicities below ~20% $Z_\odot$, so it could be that lower metallicities are required to significantly reshape the SED. We are pursuing possible reasons for this in a future paper.

5. Scaling relations in the Local Universe

In what follows, we examine the derived quantities given by SED fitting in the context of several well-established scaling relations. Such scaling relations constrain the observed parameter space of galaxy populations, and may give important insight into the assumptions behind the SED models.

5.1. The star-formation "main sequence"

It is well known that M_{star} and SFR are related both in local galaxies and at high redshift through the "star formation main sequence" (e.g., Brinchmann et al. 2004; Salim et al. 2007; Noeske et al. 2007; Karim et al. 2011; Elbaz et al. 2011). We have investigated whether the KINGFISH SED results show a similar trend in Fig. 13 where Log(SFR) is plotted against Log(M_{star}). The dashed (gray) line shows the SFMS relation derived by Hunt et al. (2016) for galaxies in the Local Universe (including KINGFISH galaxies but with recipe-derived

---

[12] Linear scaling is potentially a problem at low metallicities 12+log(O/H) ≲ 8.0 (Rémy-Ruyer et al. 2014).
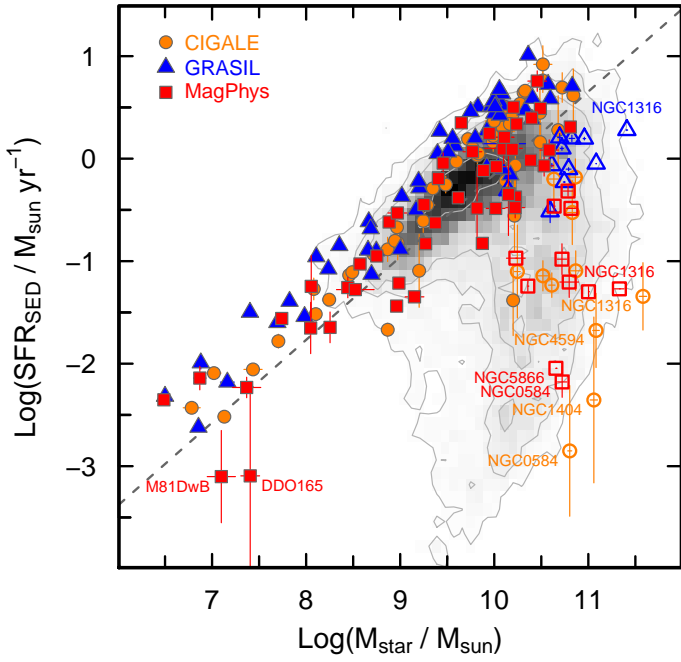
Fig. 13. SED-derived SFR vs. M_{star} in logarithmic space superimposed on the GSWLC sample shown in gray-scale from Salim et al. (2016, see text for details). As in previous figures, filled symbols correspond to high specific SFR ($\mathrm{Log}(sSFR/yr^{-1}) > -10.6$), and open ones to low specific SFR ($\mathrm{Log}(sSFR/yr^{-1}) \leq -10.6$). The (gray) dashed line corresponds to the SFMS relation found by Hunt et al. (2016) for nearby galaxies.

quantities); the slope of this relation, ~ 0.8 ($\mathrm{SFR} \propto M_{star}^{0.8}$), is consistent with the value found by Elbaz et al. (2007) of ~ 0.77 for a local comparison sample (see also compilation in Leitner 2012). As in previous figures, open symbols correspond to KINGFISH galaxies with low sSFR ($\lesssim 3 \times 10^{-11}$ yr^{-1}).

Also shown in Fig. 13 is the GALEX SDSS WISE Legacy Catalog (GSWLC) deep sample from Salim et al. (2016); the plotted points have been limited to the "Main Galaxy Sample" (MGS), and in redshift to $0.015 \leq z \leq 0.06$, and there is no K-correction applied to the data. For the GSWLC sample, the SFRs are derived by SED fitting using a different version of the CIGALE code than we use here, in particular, a SFH comprising two-component declining exponentials. Moreover, we have adopted the infrared refinement of Salim et al. (2018) that takes into account the WISE 22 µm photometry to constrain SFR; there are no longer-wavelength constraints on the SED fitting. Here, and in subsequent figures, the GSWLC gray scales correspond to galaxy number densities within the sample, with outer contours delimiting 99.99%.

Most of the galaxies having disagreements between SED-derived SFRs and the recipe values are ETGs, and thus possibly in a quenching (or already quiescent) phase of their SFH. This is seen clearly in Fig. 13 with the superposition of the KINGFISH galaxies on the GSWLC locus below the main sequence having low SFRs at high M_{star}; galaxies (virtually all early-type) falling into this category are plotted with open symbols (because of their low sSFR) and labeled in Fig. 13.

We test further the idea that these galaxies are transitioning into a more quiescent SFH phase in the upper panel of Fig. 14 where we have plotted SDSS $u-r$ colors against M_{star}. Again the KINGFISH galaxies are superimposed on the GSWLC (Salim et al. 2016, 2018) where, as before, the redshift range is limited to $0.015 \leq z \leq 0.06$, and only MGS
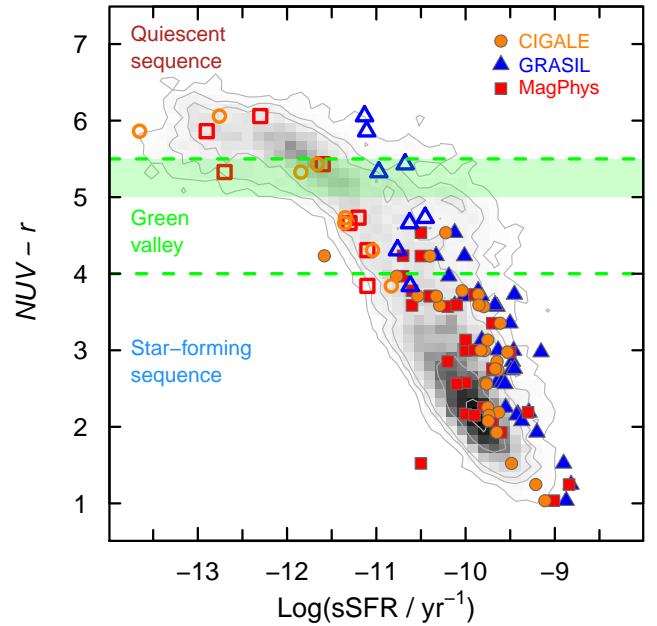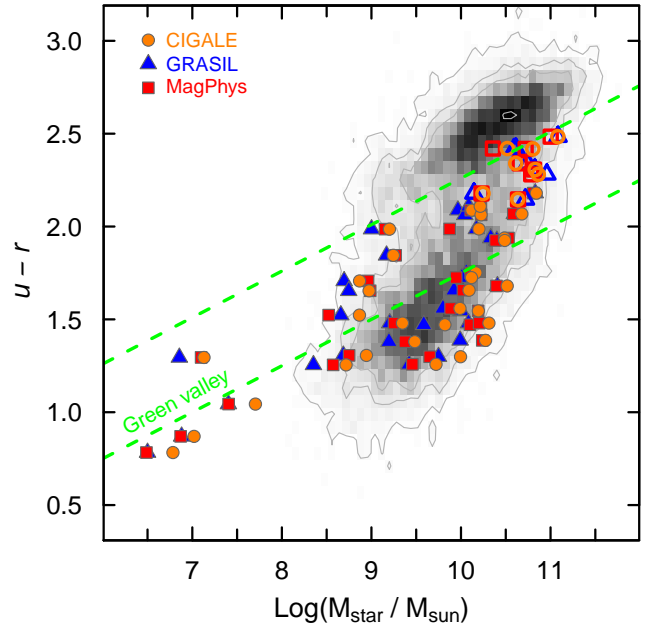
Fig. 14. Colors of KINGFISH galaxies plotted against the logarithm of stellar mass given by the respective SED-fitting algorithms (*top panel*) and the SED-derived logarithm of sSFR (*bottom*, with units of yr^{-1}); the *top panel* shows SDSS $u-r$, and the *bottom* NUV$-r$. In both panels, the KINGFISH galaxies are superimposed on the GSWLC sample, taking only those galaxies with $0.015 \leq z \leq 0.06$. As in previous figures, filled symbols correspond to high specific SFR ($\mathrm{Log}(sSFR/yr^{-1}) > -10.6$), and open ones to low specific SFR ($\mathrm{Log}(sSFR/yr^{-1}) \leq -10.6$). In the *top panel*, the (green) dashed lines correspond to the separation of the "green valley" from the upper (red) and lower (blue) loci of SDSS galaxies as given by Schawinski et al. (2014). In the *bottom*, we have included the NUV$-r$ color range for the "green valley" transition proposed by Salim (2014), together with the limit for ETG SF activity of NUV$-r = 5.5$ given by Kaviraj et al. (2007). The green shaded area marks the (uncertain) boundary between star-forming and quiescent ETGs.

galaxies are considered. The (green) dashed lines, taken from Schawinski et al. (2014), delimit the transition green valley regime from the "red sequence" to the "blue cloud". Virtually all the galaxies in which SED-derived SFRs differ from the recipe

values are upper "green-valley" or "red-sequence" galaxies, at the massive end of the transition from bluer, star-forming ones.

However, it is well established that optical colors are less sensitive to low levels of SFR than the UV (e.g., Wyder et al. 2007; Schawinski et al. 2007; Kaviraj et al. 2007; Salim 2014). NUV−r is particularly suited for examining weak SF because NUV traces young stars and r is a proxy for stellar mass. The lower panel of Fig. 14 thus plots observed NUV−r against sSFRs as estimated by the SED-fitting codes. As in previous figures, the KINGFISH galaxies are superimposed on the GSWLC sample, again limited to MGS galaxies and a redshift range of $0.015 \leq z \leq 0.06$. The NUV−r color correlates well with sSFR, proving to be an effective diagnostic of the transition from star-forming galaxy populations to more passive ones (e.g., Salim 2014). ETGs with an NUV−r color $\lesssim 5.5$ are very likely to have experienced recent star formation, even when considering the contamination by UV upturn (Kaviraj et al. 2007), while galaxies with colors redder than this have very little molecular gas (Saintonge et al. 2011) and are almost certainly non-star-forming quiescent systems (Schawinski et al. 2007). The SFRs from CIGALE and MAGPHYS are consistent with the GSWLC, and the observed NUV−r colors seem to indicate that the galaxies with particularly low sSFR (as determined by SED fitting), are in a quiescent phase of their SFH. On the other hand, GRASIL finds sSFRs that are higher for these galaxies but not inconsistent with what could be expected given their NUV−r colors.
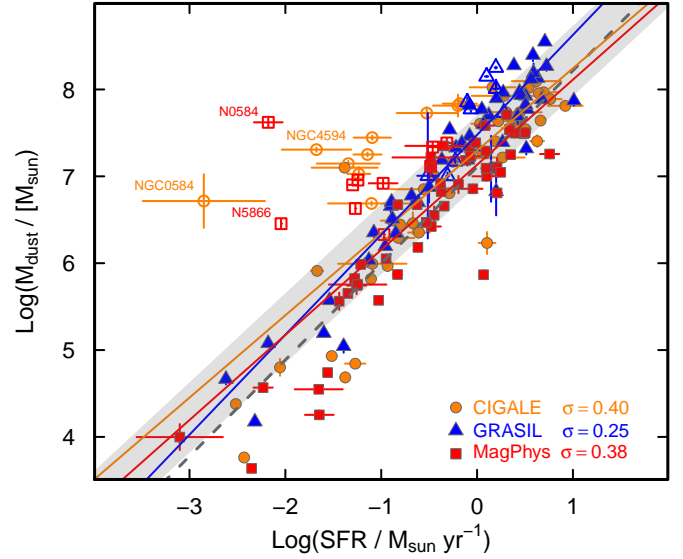
As discussed above (Sects. 3.3.2 and 4.2), galaxies with very low sSFR are difficult to model because of the potential similarity/degeneracies in SEDs in this parameter range. Such difficulties are also seen in the comparisons with reference quantities shown in Figs. 5, 8, and 12 where parameter estimations show discrepancies with SFR and L_{FUV} relative to some of the models. The essence of the problem is the SFH, and how we can ascertain observationally whether or not galaxies are already in the quenching phase.

### 5.2. Dust mass, star-formation rate, and stellar mass

Using MAGPHYS, da Cunha et al. (2010) found that M_{dust} and SFR are also tightly correlated in a large sample of SDSS galaxies with IR photometry from IRAS. We have explored this scaling relation in the KINGFISH galaxies using quantities derived from our SED fitting. This correlation is seen not only with MAGPHYS, but also with CIGALE and GRASIL as shown in Fig. 15 where the M_{dust}-SFR correlation is illustrated (only the 58 galaxies with sufficient IR photometry are plotted); the da Cunha et al. (2010) relation is given by a (gray) dashed line and the best-fit robust KINGFISH correlations (for each algorithm separately) by solid ones. M_{dust} and SFR are fairly well correlated in the KINGFISH galaxies with a scatter of ~0.4–0.5 dex.

Over four orders of magnitude in M_{dust} and SFR, the scatter is smaller than that found for the KINGFISH SFMS, and is probably suggesting something fundamental about the relation of dust mass, gas mass, and SFR as discussed by da Cunha et al. (2010). Again, galaxies with low sSFR are problematic, emerging as galaxies whose SFRs are too low for the inferred dust content; low levels of SFR are difficult to constrain observationally since evolved stars are expected to dominate the dust heating.

In their metal census in star-forming galaxies at $z \sim 0$, Peeples et al. (2014) find a correlation between M_{dust} and M_{star} using a dataset similar to the KINGFISH sample studied here. We reassess this correlation based on our SED-fitting results in Fig. 16, where M_{dust} is plotted against M_{star} in logarith-
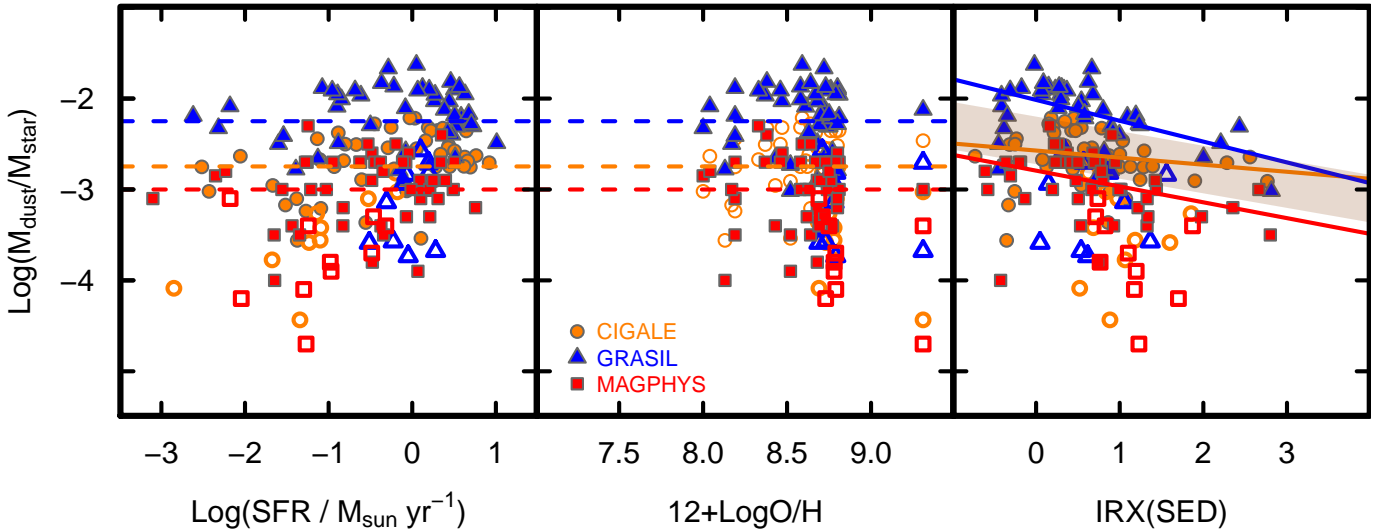

Fig. 15. SED-derived M_{dust} vs. SFR in logarithmic space. The σ values of the best-fit robust correlations are shown in the lower right corner, and the robust regressions for each SED-fitting algorithm are shown as solid lines. The (gray) dashed one corresponds to the relation given by da Cunha et al. (2010) for SDSS galaxies. The gray area illustrates the $\pm 1\sigma$ range around the mean slope: here σ corresponds to the mean rms of the three individual fits, and the mean slope to the mean of the three individual slopes. As in previous figures, filled symbols correspond to high specific SFR (Log(sSFR/yr^{-1}) > −10.6), and open ones to low specific SFR (Log(sSFR/yr^{-1}) ≤ −10.6).
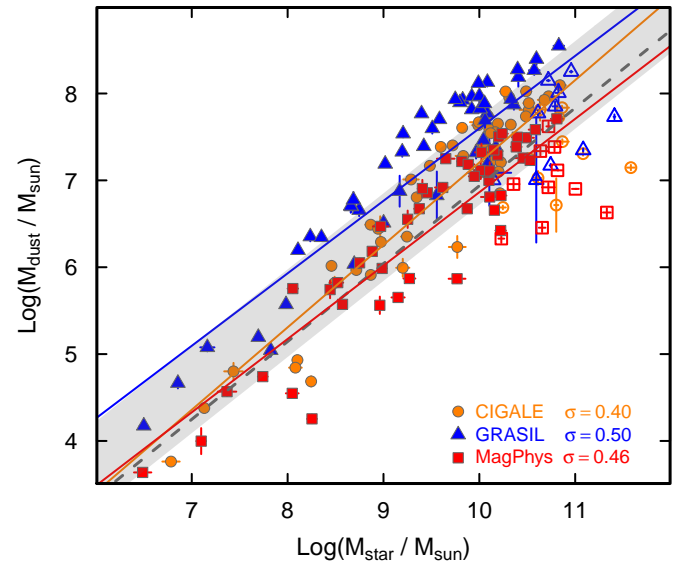
Fig. 16. SED-derived M_{dust} vs. M_{star} in logarithmic space. The σ values of the best-fit robust correlation are shown in the lower right corner. The robust correlations are shown as solid lines, and the (gray) dashed one corresponds to the relation given by da Cunha et al. (2010) for SDSS galaxies, reported to M_{star} through the SFMS by Hunt et al. (2016). The gray area is defined the same way as in Fig. 15. As in previous figures, filled symbols correspond to high specific SFR (Log(sSFR/yr^{-1}) > −10.6), and open ones to low specific SFR (Log(sSFR/yr^{-1}) ≤ −10.6).

mic space. The different SED algorithms give similar slopes (~0.8−0.9), although GRASIL is slightly shallower (~0.7). These regressions are consistent with that found by Peeples et al. (2014): Log M_{dust} = 0.86 Log M_{star} − 1.31. With the expression

Fig. 17. SED-derived M_{dust}/M_{star} ratios in logarithmic space plotted against (SED-derived) SFR, 12+log(O/H), and (SED-derived) IRX. The *middle panel* shows the PP04N2 calibration for 12+log(O/H) as described in the text. The dashed horizontal lines in the *left* and *middle panels* show the means of Log(M_{dust}/M_{star}) for each SED-fitting algorithm (dark orange: CIGALE; blue: GRASIL; red: MAGPHYS). The fits of (Log) M_{dust}/M_{star} vs. IRX for the individual SED algorithms are shown as colored solid lines in the *right panel*; the gray region gives the $\pm 1\sigma$ interval around the mean of the three individual regressions. As in previous figures, open symbols correspond to galaxies with low sSFR [Log(sSFR/yr^{-1}) ≤ -10.6], and filled symbols to high sSFR [Log(sSFR/yr^{-1}) > -10.6].

for gas-mass fraction as a function of M_{star} by Peeples et al. (2014), this expression gives gas-to-dust ratios of between ~80 and 200 for a galaxy with $M_{star} \sim 10^{10.5}\,M_\odot$.

Because of the relatively strong correlations of both M_{dust} and M_{star} with SFR (see Figs. 13 and 15), we might expect the relative dust content, as measured by dust-to-stellar mass ratios, to depend on SFR. Dust content is also thought to depend on metallicity (as measured by its emission-line proxy O/H), and on IRX, the logarithm of the ratio between L_{TIR} and (observed) L_{FUV}; thus M_{dust}/M_{star} could also correlate with these quantities. These trends are shown in Fig. 17 where we have plotted the different SED-fitting algorithms with different symbols as before. Here we have taken the metallicities from Aniano et al. (in prep.) where the original determinations by Moustakas et al. (2010; see also Kennicutt et al. 2011) have been converted to the nitrogen calibration of Pettini & Pagel (2004, hereafter PP04N2) according to the prescriptions of Kewley & Ellison (2008). For more details, see Aniano et al. (in prep.).

Overall, there appears to be little dependence of M_{dust}/M_{star} on either SFR or O/H in these galaxies. However, there is a weak trend of M_{dust}/M_{star} with IRX, with rms deviations of ~0.4 dex. The individual slopes of GRASIL and MAGPHYS are consistent, but the CIGALE slope is shallower (~−0.27 for GRASIL, MAGPHYS and −0.12 for CIGALE; see right panel of Fig. 17); the mean relation (averaged over the three SED algorithms) is Log(M_{dust}/M_{star}) = −2.5 − 0.25 IRX. If only the high sSFR points are included in the fit, the slope is shallower (−0.18) and the scatter is smaller (0.18–0.26 dex). Thus, the SED fitting of the KINGFISH galaxies implies that the dust-to-stellar mass ratio decreases with IRX, but not very steeply and with large scatter; for more than three orders of magnitude of change in IRX, the M_{dust}/M_{star} ratio decreases by only a factor of ~10 (not considering the low sSFR objects).

### 5.3. Infrared-to-ultraviolet luminosity ratio, IRX

Attenuation of UV light is also expected to depend on relative dust content, and IRX is one way to quantify this attenu-

ation (e.g., Kong et al. 2004; Cortese et al. 2006; Boquien et al. 2009, 2016; Hao et al. 2011; Viaene et al. 2016). However, IRX is somewhat dependent on the age of the dust-heating populations, so may vary with other parameters besides dust content. In Fig. 18, we compare IRX from the SED fitting of KINGFISH galaxies with the PP04N2 O/H calibration as in Fig. 17, and SED-derived M_{star} and SFR. The left panel of Fig. 18 shows the correlation of IRX with M_{star} (Pearson correlation coefficient $\rho = 0.6$–0.7). Although the formal dispersion is high ~0.6 dex, it is mostly due to the three outliers with IRX > 2: NGC 1266, an S0 galaxy with a molecular outflow (Pellegrini et al. 2013); NGC 1482, an S0 galaxy with a dusty wind (McCormick et al. 2013); and NGC 2146, a luminous IR galaxy with $L_{TIR} = 1.3 \times 10^{11}\,L_\odot$ and a powerful outflow in atomic, ionized, and molecular gas (Kreckel et al. 2014).

That IRX, a measure of dust attenuation, is roughly correlated with M_{star} is probably not surprising given the relation between visual extinction A_V and M_{star} found by Garn & Best (2010). A similar relation between UV attenuation and M_{star} is evident over a wide range of redshifts (e.g., Pannella et al. 2009, 2015; Whitaker et al. 2014; Bouwens et al. 2016). The "consensus relation" found by Bouwens et al. (2016) for galaxies at $z \sim 2-3$ is also shown as a (green) shaded region in the left panel of Fig. 18; with unit slope, it is steeper than the trends given by our SED-fitting algorithms, and could indicate selection effects at high redshift given that the KINGFISH sample probes more than two orders of magnitude lower in M_{star}. It could also point to different geometries for high-z galaxies compared to local ones. We find a mean regression of IRX = −3.4 + 0.41 Log(M_{star}). Over the mass ranges probed by the Bouwens et al. (2016) study, there is no strong evidence for evolution, at least to $z \sim 3$, consistently with the conclusions of Whitaker et al. (2014) who noted little evolution at low stellar masses $\lesssim 3 \times 10^{10}\,M_\odot$.

The middle panel of Fig. 18 illustrates the trend of IRX with SFR; the correlation is weaker than with M_{star} ($\rho = 0.4$–0.6), although excluding the low sSFR galaxies (with Log(sSFR/yr^{-1}) ≤ -10.6) would improve the tightness of the trend. The steepest power-law index is given by the GRASIL fits
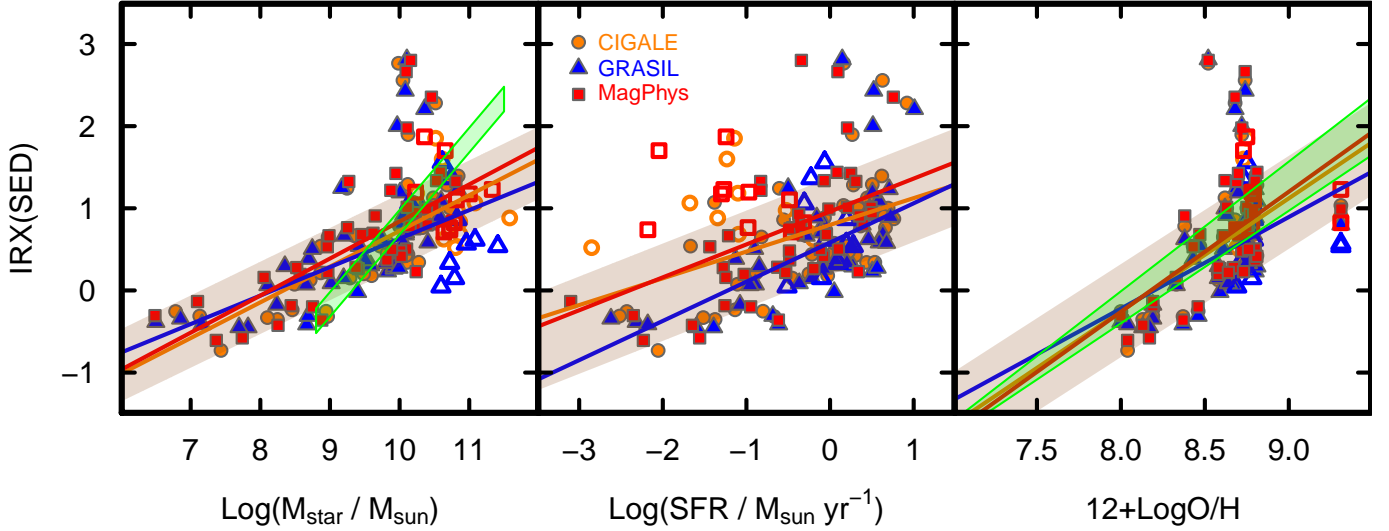
Fig. 18. IRX (from SED fitting) plotted against M_{star}, SFR, and 12+log(O/H). In each panel, the individual best-fit regressions are shown by colored solid lines, and the gray regions denote the $\pm 1\sigma$ interval around the mean regression. The *left panel* includes the "consensus" relation for galaxies at redshifts $z \sim 2-3$ found by Bouwens et al. (2016), and shown as a green shaded region. As in Fig. 17, the *right panel* shows the PP04N2 calibration for 12+log(O/H) as described in the text. Also shown in the right panel is the correlation between IRX and O/H found for normal star-forming galaxies by Cortese et al. (2006) and for starbursts by Heckman et al. (1998); the region enclosed between these two relations is green-shaded, and is slightly steeper than the mean relation. As in previous figures, open symbols correspond to galaxies with low sSFR [Log(sSFR/yr^{-1}) ≤ -10.6], and filled symbols to high sSFR [Log(sSFR/yr^{-1}) > -10.6]. The three KINGFISH galaxies with IRX > 2 are NGC 1266 (IRX = 3.3), NGC 1482 (IRX = 2.8), and NGC 2146 (IRX = 2.6); the first two are early type S0's and NGC 2146 is a luminous IR galaxy.

(0.49), and the shallowest by CIGALE (0.31); the mean regression (averaged over the three fitting algorithms) is IRX = 0.78 + 0.39 Log(SFR) that is reflecting the increase of dust content with SFR (e.g., Fig. 15).

Because of the tendency of dust content to increase with metallicity, many previous studies have examined the trend of IRX and metallicity in nearby galaxies (e.g., Heckman et al. 1998; Cortese et al. 2006; Johnson et al. 2007; Boquien et al. 2009). The correlation of IRX and metallicity shown in the right panel of Fig. 18 is thus not a new result although here we confirm it with the KINGFISH sample, albeit with large spread at Solar metallicity. The regressions found by Cortese et al. (2006, slope ~1.4) for normal star-forming galaxies and by Heckman et al. (1998, slope ~1.2) for starbursts are shown as solid (green) lines, enclosing the green-shaded region. We find similar trends with power-law indices ranging from ~1.2 (GRASIL) to 1.4 (CIGALE) and 1.5 (MAGPHYS). Given the different metallicity calibrations and the previous lack of *Herschel* data that would be expected to lower the IR contribution, the agreement is fairly good between our determination and previous ones. Here the scatter is high, ~0.5–0.6 dex ($\rho = 0.4$–0.5), but again mostly due to the three outliers at high IRX. The mean regression averaged over the three SED algorithms is: IRX = 0.28 + 1.4 (12+log(O/H)–8.0) In conclusion, for the KINGFISH galaxies IRX is at least approximately related to M_{star}, SFR, and O/H, as might be expected given that dust attenuation should grow with the increase of each of these quantities.

5.4. Inferring stellar masses from IRAC and WISE W1 luminosities

The SED-derived M_{star} values can be used to derive mass-to-light ratios and thus a new recipe for stellar masses and M/L ratios in the mid-infrared, from $\Upsilon^{[3.6]}$, based on IRAC 3.6 μm luminosities, or equivalently Υ^{W1} based on WISE W1. The super-linear power-law index for the trend of SED-M_{star} vs. M_{star} derived

with a constant Υ_* ratio indicates that the Υ_* ratio increases with increasing $L_{3.6}$, similar to the trend found by Wen et al. (2013) with L_{W1}. As we argued in Appendix B.1, IRAC 3.6 μm and WISE W1 photometry is virtually indistinguishable, and here we analyze only L_{W1} in order to compare with the GSWLC (Salim et al. 2016, 2018). To better assess non-linearity in the luminosity dependence of Υ^{W1} (or $\Upsilon^{[3.6]}$), we have fit the M/L ratio Υ^{W1} as a function of luminosity; thus in the case of constant M/L ratio, we would expect a slope of zero. Instead, we find the following best-fit regressions (where L_{W1} is given[13] in $L_{W1,\odot}$ and M_{star} in $M_{\odot}$):

$$\log[M_{star}(\text{CIGALE})/L_{W1}] =$$
$$(0.050 \pm 0.013) \log(L_{W1}) - (1.05 \pm 0.14);$$
$$\log[M_{star}(\text{GRASIL})/L_{W1}] =$$
$$(0.102 \pm 0.026) \log(L_{W1}) - (1.76 \pm 0.26);$$
$$\log[M_{star}(\text{MAGPHYS})]/L_{W1}] =$$
$$(0.079 \pm 0.024) \log(L_{W1}) - (1.46 \pm 0.25). \quad (12)$$

Figure 19 shows the mass-to-light ratio inferred from M_{star} from the SED algorithms divided by the W1 luminosity L_{W1}, together with the best-fit regressions given in Eq. (12). As seen in Fig. 19, these expressions reproduce the SED-derived M_{star} values with rms deviations of 0.11 dex, 0.16 dex, and 0.21 dex for CIGALE, GRASIL, and MAGPHYS, respectively; moreover, the slopes (+1) are identical to those given in Table 3 for $L_{3.6}$, reinforcing the notion that IRAC 3.6 μm and WISE 3.4 μm photometry is indistinguishable.

The power-law slopes are significantly larger than zero implying that to within the scatter, the M/L ratio at 3.4 μm depends on luminosity as also found by Wen et al. (2013).

[13] We have taken $L_{\odot}$(W1) to be 1.68×10^{32} erg s^{-1} (see also Cook et al. 2014), assuming that the W1 Solar (Vega) magnitude is 3.24 (Norris et al. 2014; Jarrett et al. 2013), and that the W1 zero-point calibration is 309.5 Jy (Jarrett et al. 2013).

To calculate M_{star} with the Wen et al. (2013) formulation (see Appendix B.1), we adopted their variation with Hubble type which assumes slopes between 1.03 and 1.04; however, values from the SED-fitting codes are better fit with larger slopes (see Table 3 and Eq. (12)). A comparably large slope connecting M_{star} and L_{W1} was obtained by Wen et al. (2013) for the sample as a whole (1.12), with active galaxy nuclei (AGN) having a steeper trend (1.13) than either composite (star-forming and AGN hybrids with 1.08) or late Hubble types (1.03).

Several previous studies have found that a constant value of $\Upsilon^{[3.6]} \sim 0.5-0.7$ fits SSP-derived stellar masses quite well (e.g., Oh et al. 2008; Eskew et al. 2012; Meidt et al. 2012, 2014; McGaugh & Schombert 2014, 2015; Norris et al. 2014; Querejeta et al. 2015). For $L_{W1} = 10^{11} L_\odot(W1)$ (see Fig. 19), we would infer (with CIGALE) $\Upsilon^{W1} = 0.3$, roughly 2 times smaller. From dynamical considerations of the vertical force perpendicular to the disk in 30 galaxies, Martinsson et al. (2013) find a mean K-band M/L ratio $\Upsilon^{[K]} = 0.31 \pm 0.07$. Assuming $\Upsilon^{[K]} = 1.29\,\Upsilon^{[3.6]}$ (McGaugh & Schombert 2014), this would give $\Upsilon^{W1} \approx \Upsilon^{[3.6]} = 0.24$, consistent with what we have derived from SED fitting. Just et al. (2015) analyzed a new sample of stars in the Milky Way and obtained a local volumetric mass-to-light ratio $\Upsilon^{[K]} = 0.31 \pm 0.02$, the same as found by Martinsson et al. (2013). Ponomareva et al. (2018) compared $\Upsilon^{[3.6]}$ from various methods, and found that SED fitting and dynamical arguments tend to give lower $\Upsilon^{[3.6]}$ than values derived from correlations with NIR color (e.g., Eskew et al. 2012; Meidt et al. 2014; Querejeta et al. 2015). Moreover, Fig. 19 shows a steepening luminosity dependence of Υ^{W1} beginning around $L_{W1} \sim 3 \times 10^{10} L_\odot$; thus the higher M/L ratios could also be a function of more massive samples under consideration. In any case, because the reason for these discrepancies is not yet understood, the stellar mass scale is evidently pervaded by a systematic uncertainty of roughly a factor of two (e.g., McGaugh & Schombert 2014).

Unlike global assessments of galaxy mass, to ensure that region-by-region cumulative stellar masses agree with globally measured values, resolved studies of stellar mass surface density require an approach that is linear with luminosity. Here we attempt to furnish color-dependent recipes that can be used within galaxies, rather than only between galaxies. Our approach is similar to that of Eskew et al. (2012), Meidt et al. (2014), and Querejeta et al. (2015), but here we incorporate the vast range of photometric bands available for the KINGFISH sample. The idea is to compensate the non-linear slope of the $M_{star}-$luminosity trend by exploiting the color-magnitude effect; colors typically change with luminosity (reflecting trends with age and metallicity), thus implying a change in M/L. We have investigated several single colors (ranging from FUV/NUV to W1−W3), and have also assessed the improvement offered by introducing two colors rather than only one. Judging from Zibetti et al. (2009), one of the best colors for reducing scatter in M/L ratios should be SDSS $g-i$; for the KINGFISH sample, the $g-i$ color does a good job of reducing the scatter in the Υ^{W1} ratio (0.066 dex w.r.t. 0.11 dex for CIGALE M_{star}), but this includes a residual non-linear slope with L_{W1} luminosity. Imposing linearity for Υ^{W1} gives an increased rms scatter for Υ^{W1} vs. $g-i$ of 0.075 dex (CIGALE). Other single colors we tested (in the AB system) under the necessity of imposing linearity with L_{W1} luminosity include FUV−NUV, NUV−(W1, W3), NUV−r, NUV−J, $r-J$, $i-H$, $r-$(W1,W3), $J-H$, $J-$(W1, W2, W3), and W1−W3.

Figure 20 shows Υ^{W1} plotted against the single colors that most reduced the rms scatter for the KINGFISH sample; the best color is $J-$W3 (with rms σ of 0.05 dex for CIGALE, left panel),
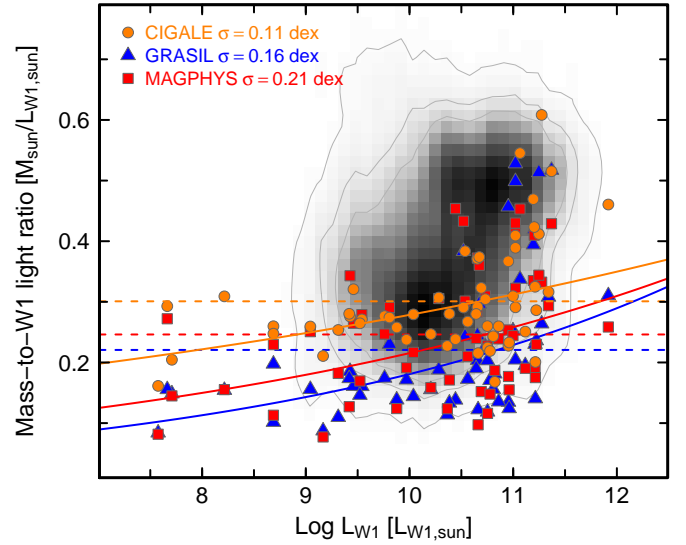
Fig. 19. SED-derived stellar masses with observed WISE W1 luminosities for mass-to-W1 light ratios plotted against observed W1 luminosity; the underlying gray scale gives the GSWLC sample from Salim et al. (2016, see text for details). Squares (orange) show CIGALE M_{star} values, triangles (blue) GRASIL, and circles (red) MAGPHYS. The robust regressions for each SED-fitting algorithm are shown as solid curves, and the σ values are given in the upper left corner. The horizontal dashed lines show the mean of Υ^{W1} for M_{star} values from the three fitting codes: 0.30 (CIGALE), 0.22 (GRASIL), and 0.25 (MAGPHYS).

followed closely by W1−W3 (rms $\sigma = 0.06$ dex for CIGALE, middle). Meidt et al. (2014) and Querejeta et al. (2015) have used W1−W2 to refine M/L ratios in the mid-infrared ($\Upsilon^{[3.6]}$, Υ^{W1}), and we have compared this color with our best-fit results in the right panel of Fig. 20. Compared to the W3 colors ($J-$W3, W1−W3), W1−W2 gives a slightly worse fit to SED-derived Υ^{W1} (rms $\sigma \sim 0.08$ dex for CIGALE). Part of the reason for this could be simply the smaller dynamic range of the W1−W2 color: ~ 0.4 AB mag relative to ~ 5 AB mag for $J-$W3 and ~ 4 AB mag for W1−W3. In other samples, the ranges in these colors tend to be even smaller, given that KINGFISH encompasses low mass, blue, dwarf galaxies, often excluded by sensitivity considerations. After experimenting with some additional colors (e.g., NUV−W1, NUV−J), with two colors the improvement in the scatter of Υ^{W1} was marginal; we were unable to reduce the scatter below ~ 0.05 dex in any case. M/L ratios derived from CIGALE M_{star} are generally less noisy with color (and luminosity) than those from either GRASIL or MAGPHYS; the reasons for this are not completely clear. Summarizing, our best recipes for resolved studies of stellar masses within galaxies are given by (see Fig. 20):

$$\log[M_{star}(\text{CIGALE})/L_{W1}] = (-0.093 \pm 0.007)\,J - W3 - (0.552 \pm 0.009);$$

$$\log[M_{star}(\text{GRASIL})/L_{W1}] = (-0.096 \pm 0.022)\,J - W3 - (0.712 \pm 0.026);$$

$$\log[M_{star}(\text{MAGPHYS})]/L_{W1}] = (-0.079 \pm 0.021)\,J - W3 - (0.653 \pm 0.024). \qquad (13)$$

(with rms deviations of 0.05 dex, 0.17 dex, and 0.16 dex for CIGALE, GRASIL, and MAGPHYS, respectively), and

$$\log[M_{star}(\text{CIGALE})/L_{W1}] = (-0.099 \pm 0.008)\,W1 - W3 - (0.485 \pm 0.009);$$
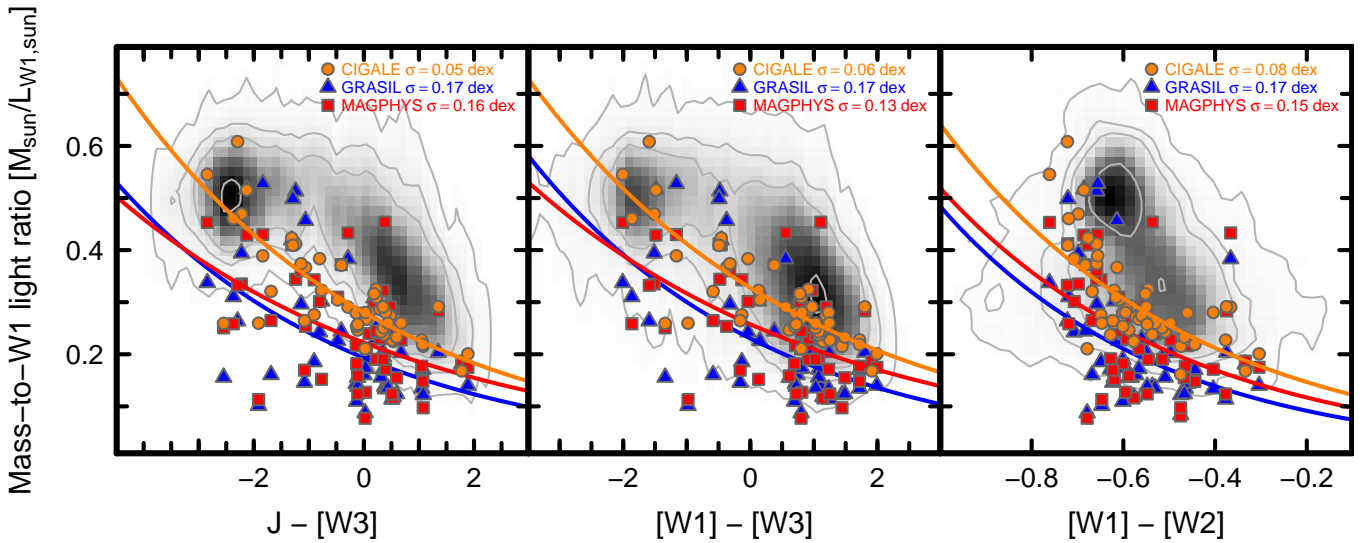
Fig. 20. Mass-to-light ratios in the WISE W1 band of KINGFISH galaxies plotted vs. the J−[W3] color (*left panel*); [W1]−[W3] (*middle*); and [W1]−[W2] (*right*). As in Fig. 19, the underlying gray scale corresponds to the GSWLC data (Salim et al. 2016). Legends in the upper right corners give the rms deviation of the robust best fits, shown as curves in each panel, of the M/L(W1) ratios vs. and colors. The best fit rms of 0.05 dex (for CIGALE) is obtained for M/L as a function of J−[W3] (*left panel*), but [W1]−[W3] is only 0.01 dex worse (for CIGALE, see *middle panel*). The fit of M/L with [W1]−[W2] (*right panel*) is the worst of all three colors shown here, but only by 0.03 dex (for CIGALE, comparable for the other two algorithms). All magnitudes are on the AB system.

$$\log[M_{star}(\text{GRASIL})/L_{W1})] =$$
$$(-0.113 \pm 0.022)\,W1 - W3 - (0.637 \pm 0.025);$$
$$\log[M_{star}(\text{MAGPHYS})]/L_{W1})] =$$
$$(-0.090 \pm 0.023)\,W1 - W3 - (0.589 \pm 0.026). \quad (14)$$

(with rms deviations of 0.06 dex, 0.17 dex, and 0.14 dex for CIGALE, GRASIL, and MAGPHYS, respectively).

Although the KINGFISH sample is much smaller in number than the SDSS collection adopted by Wen et al. (2013), it spans a large range of Hubble types and more than four orders of magnitude in M_{star}. The detailed SED fitting done here may be a better representation of stellar mass, implying a steeper variation of M/L ratio with L_{W1} (or $L_{3.6}$) than previously determined. This is borne out by the comparison with the large GSWLC sample (Salim et al. 2016), suggesting that sample selection is important because of the color dependence of the M/L ratio. Nevertheless, the comparison with the GSWLC also suggests that simple power-law recipes relating Υ^{W1} (or $\Upsilon^{[3.6]}$) to AB colors are insufficient to completely capture the behavior shown by the GSWLC: M/L is apparently constant until a threshold where M/L decreases with increasing color. Especially for extreme starbursts, it is important to subtract non-stellar emission (e.g., ionized gas continuum, hot dust) from the flux as we have described in Appendix B.1 (see also, e.g., Querejeta et al. 2015). It is also essential to avoid application of the non-linear relations in Eq. (12) to resolved measurements of stellar mass surface density.

5.5. Principal component analysis

Because of the mutual correlations of M_{star}, M_{dust}, and SFR, it is likely that one or more of them is just a secondary consequence of a fundamental, intrinsic, relation. In this case, these three variables could define a planar relation, based on just two parameters, and it is important to know which of these three is the most fundamental in defining the correlations. To accomplish this, a

PCA is an ideal tool. A PCA essentially diagonalizes the three-dimensional covariance matrix, thus defining the "optimum projection" of the parameter space which minimizes the covariance. The orientation is defined by the eigenvectors, which by definition are mutually orthogonal. For a truly planar representation, we would expect most of the variation to be contained in the first two eigenvectors; for the third, perpendicular, eigenvector, the variance should be minimal.

We have performed a PCA on Log(M_{star}), Log(M_{dust}), and Log(SFR) for each SED -fitting algorithm, and one for the independently-determined recipe quantities. For the independently-determined quantities, we have adopted the M_{star} values derived with the Wen et al. (2013) formulation, M_{dust} DL07 values from Aniano et al. (in prep.), and SFRs calculated with FUV+L_{TIR}. Results of the PCA of these variables show that they truly define a plane: 92% of the variance is contained in the first eigenvector (E1), ~5% in the second (E2), and only ~3% in the third (E3)[14]. Figure 21 illustrates the eigenvectors, and the different projections of the plane: E1 (PC1) has roughly equal contributions from all three parameters, and E2 (PC2) has virtually no dependence on M_{dust}. Interestingly, the galaxies with low sSFRs are the most discrepant from the main trends, independently of the fitting algorithm.

The eigenvector containing the least variance, E3 (PC3), is dominated by M_{dust}. Thus, by inverting the expression for E3, it is possible to calculate M_{dust} from SFR and M_{star}, to an accuracy that corresponds to the scatter of the PCA estimation. The PCA inference of M_{dust} from M_{star} and SFR is shown in Fig. 22, where we have compared M_{dust} that would be derived from the PCA (as a function of M_{star} and SFR) against the true (observed) values of M_{dust} using the values independently determined and from SED fitting. Results show that with knowledge of only M_{star} and SFR for galaxies like those in the KINGFISH sample, mainly main sequence galaxies, we can estimate M_{dust} to within a factor of 2

---

[14] These numbers come from the independently-determined quantities, but are similar for the other PCAs.
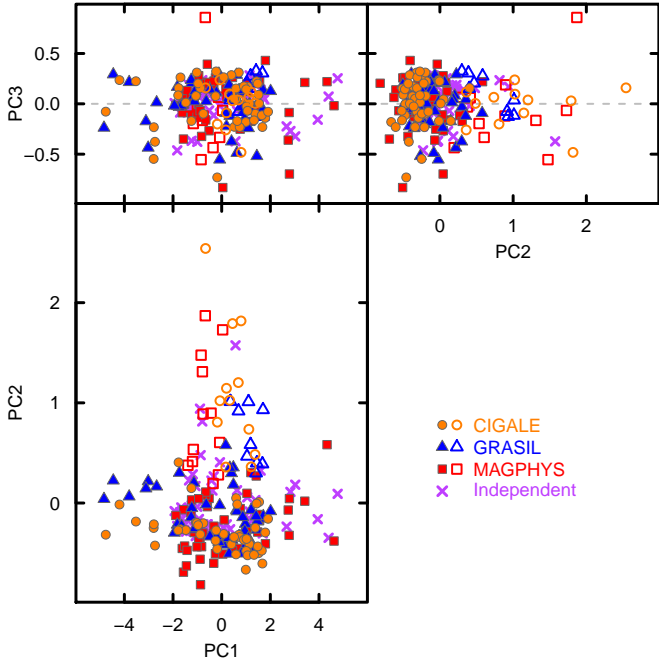
Fig. 21. Different projections of the plane defined by $\log(M_{star})$, $\log(SFR)$, and $\log(M_{dust})$ for KINGFISH galaxies: the edge-on projection is given in the *top panels* and the face-on in the *bottom*. As in previous figures, open symbols correspond to galaxies with low sSFR [$\log(sSFR/yr^{-1}) \leq -10.6$], and filled symbols to high sSFR [$\log(sSFR/yr^{-1}) > -10.6$]. With $x_1 = \log(M_{dust}) - \langle\log(M_{dust}/M_\odot)\rangle$; $x_2 = \log(SFR) - \langle\log(SFR/M_\odot \, yr^{-1})\rangle$; $x_3 = \log(M_{star}) - \langle\log(M_{star}/M_\odot)\rangle$; and for CIGALE mean values $\langle\log(M_{dust}/M_\odot)\rangle = 6.93$; $\langle\log(SFR/M_\odot \, yr^{-1})\rangle = -0.44$; $\langle\log(M_{star}/M_\odot)\rangle = 9.76$; we find PC1 $= 0.65\,x_1 + 0.48\,x_2 + 0.59\,x_3$; PC2 $= 0.01\,x_1 - 0.80\,x_2 + 0.60\,x_3$; PC3 $= 0.76\,x_1 - 0.37\,x_2 - 0.54\,x_3$. The PCAs for the different SED-fitting algorithms are similar.

($\sigma \sim 0.26\,dex$) through the equation:

$$\log(M_{dust}) = 1.13 \log(SFR) + 0.14 \log(M_*) + 5.77, \qquad (15)$$

where M_{dust} and M_{star} are in units of $M_\odot$, and SFR in $M_\odot \, yr^{-1}$. Equation (15) is the equation resulting from the independent-parameter PCA with M_{dust} from DL07 models (Aniano et al., in prep.), while the PCA from MBB M_{dust} values is somewhat different ($\sigma \sim 0.31\,dex$):

$$\log(M_{dust}) = 0.80 \log(SFR) + 0.36 \log(M_*) + 3.58. \qquad (16)$$

Those for the SED-fitting algorithms are close to these: CIGALE ($\sigma = 0.29\,dex$):

$$\log(M_{dust}) = 0.48 \log(SFR) + 0.71 \log(M_*) + 0.23 \qquad (17)$$

GRASIL ($\sigma = 0.32\,dex$) :

$$\log(M_{dust}) = 1.14 \log(SFR) + 0.090 \log(M_*) + 6.58 \qquad (18)$$

MAGPHYS ($\sigma = 0.36\,dex$):

$$\log(M_{dust}) = 0.46 \log(SFR) + 0.66 \log(M_*) + 0.49. \qquad (19)$$

The seemingly innocuous differences in the behavior of the three SED-fitting codes emerge strikingly in the PCA. In particular, GRASIL coefficients are most similar to the PCA derived from the DL07 M_{dust} values (see Eq. (15)), and CIGALE and MAGPHYS are consistent with the PCA with MBB values (Eq. (16)). The PCAs of CIGALE and MAGPHYS are different from GRASIL, but
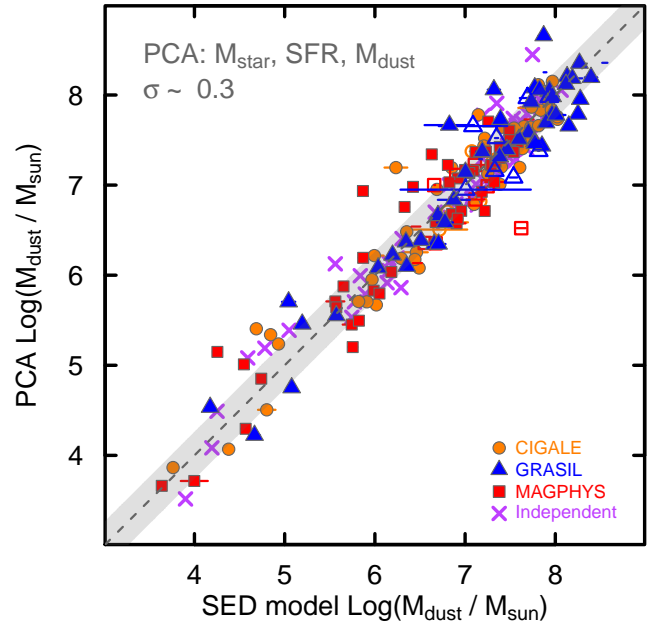
Fig. 22. PCA-derived $\log(M_{dust})$ vs. model SED-derived and "independently"-derived (here MBB) $\log(M_{dust})$ for KINGFISH galaxies. The identity relation as a (gray) dashed line as described in the text. and the σ values of the four PCAs range from (0.28 dex for CIGALE to 0.4 dex for GRASIL), with mean $\sigma \sim 0.3$; the gray region shows identity $\pm 1\sigma$. As in previous figures, open symbols correspond to galaxies with low sSFR [$\log(sSFR/yr^{-1}) \leq -10.6$], and filled symbols to high sSFR [$\log(sSFR/yr^{-1}) > -10.6$]. Horizontal error bars show the uncertainties in the SED-fitted parameters (usually smaller than the symbol size).

mutually consistent, possibly because of the similarity in their underlying assumptions (see Table 1).

Independently of the SED code, we might expect that M_{dust} depends on metallicity (or its common proxy, oxygen abundance O/H), so we have also performed a PCA on a set of four quantities, M_{star}, M_{dust}, and SFR as before, but now including $12+\log(O/H)$. As in the previous section, we have taken the values of $12+\log(O/H)$ from Aniano et al. (in prep.) converted to the nitrogen calibration of Pettini & Pagel (2004) according to Kewley & Ellison (2008). In this case, the least variation is contained in the eigenvector dominated by O/H, similar to other PCA analyses including M_{star}, SFR, and O/H of galaxies (e.g., Hunt et al. 2012, 2016; Bothwell et al. 2016). Thus, $12+\log(O/H)$ can be expressed as a linear combination of terms depending on M_{star}, M_{dust}, and SFR to the accuracy (mean dispersion) of the PCA, in this case 0.14 dex.

However, this mean dispersion is similar to that obtained by a 3-component PCA without M_{dust}, namely with M_{star}, SFR, and $12+\log(O/H)$. For a sample of ~1000 galaxies up to $z \sim 3.7$ using the PP04N2 O/H calibration, Hunt et al. (2016) find a mean dispersion of ~0.16 dex of such a PCA. Performing a similar 3-component PCA analysis on the ~60 KINGFISH galaxies alone gives a mean dispersion of 0.15 dex, not significantly larger than with the 4-component PCA including M_{dust}. This is telling us that the addition of the M_{dust} parameter does not help to reduce the scatter of the PCA. The correlations of M_{dust} with M_{star} and SFR make M_{dust} superfluous in describing the scaling relations with metallicity. In fact, we have inverted the 4-component PCA to derive M_{dust}, even though the M_{dust}-dominated eigenvector does not contain the least variation; the result is an expression for M_{dust} which has the same dispersion as that without $12+\log(O/H)$ (~0.3 dex). Thus, for the KINGFISH

sample, it seems that M_{star} and SFR are sufficient to determine M_{dust} to within a factor of two. Moreover, M_{dust} is not needed to determine 12+log(O/H) to an accuracy of ~0.14–0.15 dex; M_{star} and SFR alone are also sufficient to describe metallicity. Ultimately, at least for the KINGFISH galaxies, the relative importance of current star formation (SFR) and past star formation (M_{star}) essentially drive the observed dust content and metallicity.

6. Summary and conclusions

We have fit the observed SEDs (Dale et al. 2017) of the 61 galaxies from KINGFISH with three well-known models: CIGALE (Noll et al. 2009), GRASIL (Silva et al. 1998), and MAGPHYS (da Cunha et al. 2008). Although these codes differ in their approach to defining SFHs and dust attenuation, they all provide excellent approximations to the shape of the observed SEDs with rms deviations ranging from (0.05–0.08 dex); these values are comparable to the typical uncertainties in the fluxes (Dale et al. 2017). Nevertheless, the three algorithms show significantly different behavior in the mid-infrared: in the 25–70 μm range where there are no observational constraints, but also between 5 μm and 10 μm where the SED is constrained by observations and dominated by PAH emission. We summarize below the comparison of the associated SED derived quantities with recipe-derived values of M_{star}, SFR, M_{dust}, and monochromatic luminosities.

- Stellar masses estimated with simple methods are fairly consistent with the SED-fitting results to within ≲0.2 dex (see Fig. 4). Nevertheless, the assumption of the "standard" (e.g., McGaugh & Schombert 2014) constant 3.6 μm M/L ratio results in super-linear power-law slopes relative to SED-inferred values, and overestimates M_{star} by ~0.3–0.5 dex.
- Although there is generally good agreement between SED-derived SFRs and those estimated either from FUV+TIR or from Hα+24 μm luminosities, in galaxies with low sSFRs (≲3 × 10^{-11} yr), recipe SFRs are larger than those from CIGALE and to some extent MAGPHYS. SFRs in galaxies without IR constraints can create some difficulties for GRASIL (see Fig. 5).
- The most salient difference among the three fitting codes is in the determination of M_{dust}; GRASIL tends to give dust masses that are larger than either CIGALE or MAGPHYS (or the recipe values) by a factor of ~0.3 dex (see Fig. 6). Because it is the only code that performs radiative transfer in realistic geometries, this may be telling us that the usual methods of deriving M_{dust} are underestimating dust mass even in "normal" galaxies like the KINGFISH sample.
- Infrared luminosity L_{TIR} is the most robust recipe estimate, consistent with all the SED-inferred values to within 0.02–0.09 dex (see Fig. 7). FUV luminosity L_{FUV} derived from photometry and corrected using IRX (e.g., Hao et al. 2011; Murphy et al. 2011) is within 0.08−0.13 dex of the L_{FUV} from the SED (Fig. 8), although the recipe estimate of FUV extinction A_{FUV} is too high compared with all three SED codes (see Fig. 9). This is almost certainly due to a clumpy dust distribution that, for a given IRX value, would reduce the effective attenuation, relative to the uniform dust screens implicitly assumed by the IRX recipes.

We have explored scaling relations based on the derived quantities from SED fitting, and confirm previously established relations including the SFMS, the correlation between M_{dust} and SFR (e.g., da Cunha et al. 2010), between M_{dust} and M_{star} (e.g., Peeples et al. 2014), and various scalings of IRX including M_{star}, SFR, and O/H (see Fig. 18). Galaxies with low sSFRs tend to

be either on the red sequence as quenched systems or in a pre-quenching phase of their SFHs, as reflected by their UV-optical colors and discrepancies between recipe and model SFRs. As seen in Fig. 14, these disagreements occur primarily in galaxies with red NUV−r ≳ 5, where the correlation between NUV−r and sSFR begins to degrade and flatten.

We have established a new expression for M_{star} depending on L_{W1} and colors that is accurate to 0.06–0.17 dex (see Eqs. (12)–(14)). In addition, to further investigate possible dependencies among the fundamental quantities, we have computed a PCA of the KINGFISH sample using M_{star}, SFR, O/H, and M_{dust}. The result is that both O/H and M_{dust} can be expressed to within good accuracy using only M_{star} and SFR. The PCA of M_{star}, SFR, and M_{dust} is to our knowledge a new result, and enables estimating dust mass to within a factor of 2 using only M_{star} and SFR (see Eqs. (15) and (16)).

Overall, our results suggest that there are two main challenges to global SED fitting of galaxies. The first is the problem of assessing dust mass and the dust properties that shape attenuation curves. Dust luminosity drives the infrared shape of the SED, but absorption and attenuation are governed by dust mass and also strongly affected by geometry and dust inhomogeneities. The absorbing (and scattering) dust is not necessarily the same dust as the dust that dominates the emission of the long-wavelength SED. A galaxy's inclination is also crucial because the lines of sight in the outer regions include cooler dust that may not be detectable at low inclination. Inferring dust properties from SED fitting requires a large spectral range in photometry, but even then, accurate dust masses are difficult to obtain; this is mainly because of the temperature mixing along the line of sight (e.g., Hunt et al. 2015a), but also because of the lack of consensus about dust opacities (see Sect. 3.3.3).

A second challenge is the inherent degeneracy of using SED fitting to derive fundamental properties of galaxies such as SFRs and SFHs. We have shown that galaxies with low sSFRs are problematic, and the lack of diagnostic power of the SED gets translated into problems with L_{FUV} and attenuation as measured by A_{FUV} (see e.g., Figs. 5, 8, 9). Evidence shows that most of the problematic galaxies with low sSFRs are in a quenching or pre-quenching phase (see e.g., Figs. 13 and 14). Thus an important, possibly the most crucial, aspect of SED fitting is the approach to SFHs, and consequent degeneracies in connecting a specific SFH with a specific form of the SED. There is an ambiguity of heating sources for dust (young vs. old stars), and in the MIR spectral regime, there are mixed contributions of ionized gas, stellar photospheres, and hot dust, both stochastically- and bulk-heated. These aspects of the emerging SED are dependent on the evolutionary phase of the galaxy as determined by its SFH. The different approach of GRASIL may be an advantage particularly in the case of low sSFRs, because the shape of the SED is not directly connected with the fitted parameters (see Table 1).

Although CIGALE, GRASIL, and MAGPHYS are rather different in their approaches to fitting SEDs, they are all extremely successful in reproducing the observed SED shapes. Throughout the paper, we have emphasized that the three codes give generally similar estimates of the fundamental quantities M_{star}, SFR, M_{dust}, dust optical depth, and monochromatic luminosities. The implication is that in some sense the problem is overdetermined, that is the number of parameters necessary to construct a SED model exceeds the number of unknown quantities defining its shape. Thus, either the SED fitting is not altogether sensitive to the specific underlying physics or there are "hidden" dependencies among the fundamental quantities. Indeed, these emerge as scaling relations that are observed broadly among all galaxy types.

Given the amount of already available new FUV, IR, and mm data, together with observations of atomic and molecular gas (e.g., Salim et al. 2016; De Vis et al. 2017; Orellana et al. 2017), it is paramount to establish the systematics of different SED models. The models tested here are expected to remain at the state-of-the-art for many years to come, given their current success in fitting panchromatic galaxy SEDs. Their further application to larger datasets containing galaxies with more extreme properties has been, and will continue to be, an important tool for understanding galaxy evolution both in the nearby and distant universe.

References

Aniano, G., Draine, B. T., Calzetti, D., et al. 2012, ApJ, 756, 138
Bendo, G. J., Wilson, C. D., Pohlen, M., et al. 2010, A&A, 518, L65
Bendo, G. J., Boselli, A., Dariush, A., et al. 2012, MNRAS, 419, 1833
Berta, S., Lutz, D., Santini, P., et al. 2013, A&A, 551, A100
Bianchi, S. 2007, A&A, 471, 765
Bianchi, S. 2013, A&A, 552, A89
Binette, L., Magris, C. G., Stasińska, G., & Bruzual, A. G. 1994, A&A, 292, 13
Binney, J., & Merrifield, M. 1998, Galactic Astronomy (Princeton: Princeton Univ. Press)
Boquien, M., Calzetti, D., Kennicutt, R., et al. 2009, ApJ, 706, 553
Boquien, M., Buat, V., Boselli, A., et al. 2012, A&A, 539, A145
Boquien, M., Buat, V., & Perret, V. 2014, A&A, 571, A72
Boquien, M., Kennicutt, R., Calzetti, D., et al. 2016, A&A, 591, A6
Boquien, M., Burgarella, D., Roehlly, Y., et al. 2019, A&A, in press, DOI: 10.1051/0004-6361/201834156
Boselli, A., Cuillandre, J. C., Fossati, M., et al. 2016, A&A, 587, A68
Bothwell, M. S., Maiolino, R., Peng, Y., et al. 2016, MNRAS, 455, 1156
Bouwens, R. J., Aravena, M., Decarli, R., et al. 2016, ApJ, 833, 72
Bressan, A., Granato, G. L., & Silva, L. 1998, A&A, 332, 135
Bressan, A., Silva, L., & Granato, G. L. 2002, A&A, 392, 377
Brinchmann, J., Charlot, S., White, S. D. M., et al. 2004, MNRAS, 351, 1151
Brown, M. J. I., Jarrett, T. H., & Cluver, M. E. 2014a, PASA, 31, 49
Brown, M. J. I., Moustakas, J., Smith, J.-D. T., et al. 2014b, ApJS, 212, 18
Bruzual, G., & Charlot, S. 2003, MNRAS, 344, 1000
Buat, V., Iglesias-Páramo, J., Seibert, M., et al. 2005, ApJ, 619, L51
Buat, V., Noll, S., Burgarella, D., et al. 2012, A&A, 545, A141
Burgarella, D., Heinis, S., Magdis, G., et al. 2011, ApJ, 734, L12
Calura, F., Pipino, A., Chiappini, C., Matteucci, F., & Maiolino, R. 2009, A&A, 504, 373
Calzetti, D., Armus, L., Bohlin, R. C., et al. 2000, ApJ, 533, 682
Calzetti, D., Wu, S.-Y., Hong, S., et al. 2010, ApJ, 714, 1256
Chabrier, G. 2003, PASP, 115, 763
Charlot, S., & Fall, S. M. 2000, ApJ, 539, 718
Ciesla, L., Boquien, M., Boselli, A., et al. 2014, A&A, 565, A128
Ciesla, L., Boselli, A., Elbaz, D., et al. 2016, A&A, 585, A43
Conroy, C., White, M., & Gunn, J. E. 2010, ApJ, 708, 58
Cook, D. O., Dale, D. A., Johnson, B. D., et al. 2014, MNRAS, 445, 899
Cortese, L., Boselli, A., Buat, V., et al. 2006, ApJ, 637, 242
da Cunha, E., Charlot, S., & Elbaz, D. 2008, MNRAS, 388, 1595
da Cunha, E., Eminian, C., Charlot, S., & Blaizot, J. 2010, MNRAS, 403, 1894
Dale, D. A., & Helou, G. 2002, ApJ, 576, 159
Dale, D. A., Aniano, G., Engelbracht, C. W., et al. 2012, ApJ, 745, 95
Dale, D. A., Cook, D. O., Roussel, H., et al. 2017, ApJ, 837, 90
Davis, T. A., Young, L. M., Crocker, A. F., et al. 2014, MNRAS, 444, 3427
De Looze, I., Fritz, J., Baes, M., et al. 2014, A&A, 571, A69

De Vis, P., Dunne, L., Maddox, S., et al. 2017, MNRAS, 464, 4680
Dole, H., Lagache, G., Puget, J.-L., et al. 2006, A&A, 451, 417
Draine, B. T. 2003, ARA&A, 41, 241
Draine, B. T., & Li, A. 2007, ApJ, 657, 810
Draine, B. T., Dale, D. A., Bendo, G., et al. 2007, ApJ, 663, 866
Draine, B. T., Aniano, G., Krause, O., et al. 2014, ApJ, 780, 172
Dunne, L., Eales, S., Edmunds, M., et al. 2000, MNRAS, 315, 115
Elbaz, D., Daddi, E., Le Borgne, D., et al. 2007, A&A, 468, 33
Elbaz, D., Dickinson, M., Hwang, H. S., et al. 2011, A&A, 533, A119
Eskew, M., Zaritsky, D., & Meidt, S. 2012, AJ, 143, 139
Fox, J. 2008, Applied Regression Analysis and Generalized Linear Models (SAGE Publications)
Franceschini, A., Rodighiero, G., & Vaccari, M. 2008, A&A, 487, 837
Galametz, M., Kennicutt, R. C., Calzetti, D., et al. 2013, MNRAS, 431, 1956
Galliano, F., Hony, S., Bernard, J.-P., et al. 2011, A&A, 536, A88
Garn, T., & Best, P. N. 2010, MNRAS, 409, 421
Giovannoli, E., Buat, V., Noll, S., Burgarella, D., & Magnelli, B. 2011, A&A, 525, A150
Gordon, K. D., Clayton, G. C., Witt, A. N., & Misselt, K. A. 2000, ApJ, 533, 236
Grossi, M., Hunt, L. K., Madden, S. C., et al. 2015, A&A, 574, A126
Hao, C.-N., Kennicutt, R. C., Johnson, B. D., et al. 2011, ApJ, 741, 124
Hastings, W. K. 1970, Biometrika, 57, 97
Hauser, M. G., & Dwek, E. 2001, ARA&A, 39, 249
Hayward, C. C., & Smith, D. J. B. 2015, MNRAS, 446, 1512
Hayward, C. C., Lanz, L., Ashby, M. L. N., et al. 2014, MNRAS, 445, 1598
Heckman, T. M., Robert, C., Leitherer, C., Garnett, D. R., & van der Rydt, F. 1998, ApJ, 503, 646
Helou, G. 1986, ApJ, 311, L33
Herrera-Camus, R., Bolatto, A. D., Wolfire, M. G., et al. 2015, ApJ, 800, 1
Hunt, L., Magrini, L., Galli, D., et al. 2012, MNRAS, 427, 906
Hunt, L. K., Draine, B. T., Bianchi, S., et al. 2015a, A&A, 576, A33
Hunt, L. K., García-Burillo, S., Casasola, V., et al. 2015b, A&A, 583, A114
Hunt, L., Dayal, P., Magrini, L., & Ferrara, A. 2016, MNRAS, 463, 2002
Iglesias-Páramo, J., Buat, V., Hernández-Fernández, J., et al. 2007, ApJ, 670, 279
Jarrett, T. H., Masci, F., Tsai, C. W., et al. 2013, AJ, 145, 6
Johnson, B. D., Schiminovich, D., Seibert, M., et al. 2007, ApJS, 173, 392
Just, A., Fuchs, B., Jahreiß, H., et al. 2015, MNRAS, 451, 149
Karim, A., Schinnerer, E., Martínez-Sansigre, A., et al. 2011, ApJ, 730, 61
Kaviraj, S., Schawinski, K., Devriendt, J. E. G., et al. 2007, ApJS, 173, 619
Kennicutt, R. C., Calzetti, D., Aniano, G., et al. 2011, PASP, 123, 1347
Kennicutt, Jr., R. C. 1998, ApJ, 498, 541
Kennicutt, Jr., R. C., Armus, L., Bendo, G., et al. 2003, PASP, 115, 928
Kennicutt, Jr., R. C., Hao, C.-N., Calzetti, D., et al. 2009, ApJ, 703, 1672
Kewley, L. J., & Ellison, S. L. 2008, ApJ, 681, 1183
King, I. 1962, AJ, 67, 471
Kong, X., Charlot, S., Brinchmann, J., & Fall, S. M. 2004, MNRAS, 349, 769
Kreckel, K., Armus, L., Groves, B., et al. 2014, ApJ, 790, 26
Kroupa, P. 2001, MNRAS, 322, 231
Laor, A., & Draine, B. T. 1993, ApJ, 402, 441
Leitner, S. N. 2012, ApJ, 745, 149
Leroy, A. K., Bigiel, F., de Blok, W. J. G., et al. 2012, AJ, 144, 3
Li, G. 2006, Robust Regression (John Wiley & Sons, Inc.), 281
Lo Faro, B., Franceschini, A., Vaccari, M., et al. 2013, ApJ, 762, 108
Lotz, J. M., Ferguson, H. C., & Bohlin, R. C. 2000, ApJ, 532, 830
Magdis, G. E., Daddi, E., Béthermin, M., et al. 2012, ApJ, 760, 6
Maraston, C. 2005, MNRAS, 362, 799
Martinsson, T. P. K., Verheijen, M. A. W., Westfall, K. B., et al. 2013, A&A, 557, A131
McCormick, A., Veilleux, S., & Rupke, D. S. N. 2013, ApJ, 774, 126
McGaugh, S. S., & Schombert, J. M. 2014, AJ, 148, 77
McGaugh, S. S., & Schombert, J. M. 2015, ApJ, 802, 18
Meidt, S. E., Schinnerer, E., Knapen, J. H., et al. 2012, ApJ, 744, 17
Meidt, S. E., Schinnerer, E., van de Ven, G., et al. 2014, ApJ, 788, 144
Metropolis, N., Rosenbluth, A. W., Rosenbluth, M. N., Teller, A. H., & Teller, E. 1953, J. Chem. Phys., 21, 1087
Michałowski, M. J., Hjorth, J., Castro Cerón, J. M., & Watson, D. 2008, ApJ, 672, 817
Michałowski, M. J., Hayward, C. C., Dunlop, J. S., et al. 2014, A&A, 571, A75
Moustakas, J., Kennicutt, Jr., R. C., Tremonti, C. A., et al. 2010, ApJS, 190, 233
Muñoz-Mateos, J. C., Boissier, S., de Gil Paz, A., et al. 2011, ApJ, 731, 10
Murphy, E. J., Condon, J. J., Schinnerer, E., et al. 2011, ApJ, 737, 67
Natta, A., & Panagia, N. 1984, ApJ, 287, 228
Nikutta, R. 2012, PhD Thesis, University of Kentucky, USA
Noeske, K. G., Weiner, B. J., Faber, S. M., et al. 2007, ApJ, 660, L43
Noll, S., Burgarella, D., Giovannoli, E., et al. 2009, A&A, 507, 1793
Norris, M. A., Meidt, S., Van de Ven, G., et al. 2014, ApJ, 797, 55
Oh, S.-H., de Blok, W. J. G., Walter, F., Brinks, E., & Kennicutt, Jr., R. C. 2008, AJ, 136, 2761

Orellana, G., Nagar, N. M., Elbaz, D., et al. 2017, A&A, 602, A68
Osterbrock, D. E., & Ferland, G. J. 2006, Astrophysics of Gaseous Nebulae and Active Galactic Nuclei (Sausalito, CA: University Science Books)
Pannella, M., Carilli, C. L., Daddi, E., et al. 2009, ApJ, 698, L116
Pannella, M., Elbaz, D., Daddi, E., et al. 2015, ApJ, 807, 141
Pappalardo, C., Bizzocchi, L., Fritz, J., et al. 2016, A&A, 589, A11
Peeples, M. S., Werk, J. K., Tumlinson, J., et al. 2014, ApJ, 786, 54
Pellegrini, E. W., Smith, J. D., Wolfire, M. G., et al. 2013, ApJ, 779, L19
Pereira-Santaella, M., Alonso-Herrero, A., Colina, L., et al. 2015, A&A, 577, A78
Pérez-González, P. G., Kennicutt, Jr., R. C., Gordon, K. D., et al. 2006, ApJ, 648, 987
Pettini, M., & Pagel, B. E. J. 2004, MNRAS, 348, L59
Planck Collaboration Int. XXIX. 2016, A&A, 586, A132
Ponomareva, A. A., Verheijen, M. A. W., Papastergis, E., Bosma, A., & Peletier, R. F. 2018, MNRAS, 474, 4366
Pozzetti, L., & Mannucci, F. 2000, MNRAS, 317, L17
Querejeta, M., Meidt, S. E., Schinnerer, E., et al. 2015, ApJS, 219, 5
Rémy-Ruyer, A., Madden, S. C., Galliano, F., et al. 2014, A&A, 563, A31
Rémy-Ruyer, A., Madden, S. C., Galliano, F., et al. 2015, A&A, 582, A121
Rich, R. M., Salim, S., Brinchmann, J., et al. 2005, ApJ, 619, L107
Roussel, H., Helou, G., Smith, J. D., et al. 2006, ApJ, 646, 841
Saintonge, A., Kauffmann, G., Kramer, C., et al. 2011, MNRAS, 415, 32
Salim, S. 2014, Serb. Astron. J., 189, 1
Salim, S., Rich, R. M., Charlot, S., et al. 2007, ApJS, 173, 267
Salim, S., Lee, J. C., Janowiecki, S., et al. 2016, ApJS, 227, 2
Salim, S., Boquien, M., & Lee, J. C. 2018, ApJ, 859, 11
Santini, P., Maiolino, R., Magnelli, B., et al. 2014, A&A, 562, A30
Sarzi, M., Shields, J. C., Schawinski, K., et al. 2010, MNRAS, 402, 2187
Sauvage, M., & Thuan, T. X. 1992, ApJ, 396, L69
Schawinski, K., Kaviraj, S., Khochfar, S., et al. 2007, ApJS, 173, 512
Schawinski, K., Urry, C. M., Simmons, B. D., et al. 2014, MNRAS, 440, 889
Schiminovich, D., Wyder, T. K., Martin, D. C., et al. 2007, ApJS, 173, 315
Schlafly, E. F., & Finkbeiner, D. P. 2011, ApJ, 737, 103
Schmidt, M. 1959, ApJ, 129, 243
Silva, L. 1999, PhD Thesis, SISSA, Italy
Silva, L., Granato, G. L., Bressan, A., & Danese, L. 1998, ApJ, 509, 103
Skibba, R. A., Engelbracht, C. W., Dale, D., et al. 2011, ApJ, 738, 89
Smith, B. J., & Hancock, M. 2009, AJ, 138, 130
Smith, J. D. T., Draine, B. T., Dale, D. A., et al. 2007, ApJ, 656, 770
Smith, D. J. B., Dunne, L., da Cunha, E., et al. 2012, MNRAS, 427, 703
Speagle, J. S., Steinhardt, C. L., Capak, P. L., & Silverman, J. D. 2014, ApJS, 214, 15
Takagi, T., Vansevicius, V., & Arimoto, N. 2003, PASJ, 55, 385
Temi, P., Brighenti, F., & Mathews, W. G. 2009a, ApJ, 695, 1
Temi, P., Brighenti, F., & Mathews, W. G. 2009b, ApJ, 707, 890
Trotta, R. 2008, Contemp. Phys., 49, 71
Verley, S., Corbelli, E., Giovanardi, C., & Hunt, L. K. 2009, A&A, 493, 453
Viaene, S., Fritz, J., Baes, M., et al. 2014, A&A, 567, A71
Viaene, S., Baes, M., Bendo, G., et al. 2016, A&A, 586, A13
Viaene, S., Baes, M., Tamm, A., et al. 2017, A&A, 599, A64
Walterbos, R. A. M., & Schwering, P. B. W. 1987, A&A, 180, 27
Wen, X.-Q., Wu, H., Zhu, Y.-N., et al. 2013, MNRAS, 433, 2946
Whitaker, K. E., Franx, M., Leja, J., et al. 2014, ApJ, 795, 104
Witt, A. N., & Gordon, K. D. 1996, ApJ, 463, 681
Witt, A. N., & Gordon, K. D. 2000, ApJ, 528, 799
Wu, Y., Helou, G., Armus, L., et al. 2010, ApJ, 723, 895
Wyder, T. K., Martin, D. C., Schiminovich, D., et al. 2007, ApJS, 173, 293
Zibetti, S., Charlot, S., & Rix, H.-W. 2009, MNRAS, 400, 1181

1 INAF/Osservatorio Astrofisico di Arcetri, Largo Enrico Fermi 5, 50125 Firenze, Italy
e-mail: hunt@arcetri.astro.it
2 Department of Physics and Astronomy, University College London, Gower Street, London WC1E 6BT, UK
3 Sterrenkundig Observatorium, Universiteit Gent, Krijgslaan 281 S9, 9000 Gent, Belgium
4 Centro de Astronomía (CITEVA), Universidad de Antofagasta, Avenida Angamos 601, Antofagasta, Chile
5 National Optical Astronomy Observatory, 950 N. Cherry Ave., Tucson, AZ 85719, USA
6 Instituto de Astrofísica, Facultad de Física, Pontificia, Universidad Católica de Chile, 306 Santiago 22, Chile
7 INAF/Osservatorio di Astrofisica e Scienza dello Spazio di Bologna, Via Gobetti 93/3, 40129 Bologna, Italy
8 Department of Physics and Astronomy, University of Wyoming, Laramie, WY 82071, USA
9 INAF/Osservatorio Astronomico di Trieste, Via G. B. Tiepolo 11, 34143 Trieste, Italy
10 Institute of Astronomy, University of Cambridge, Madingley Road, Cambridge CB3 0HA, UK
11 Steward Observatory, University of Arizona, 933 North Cherry Avenue, Tucson, AZ 85721, USA
12 Department of Physics & Astronomy, Texas A&M University, College Station, TX 777843, USA
13 IRFU, CEA, Université Paris-Saclay, 91191 Gif-sur-Yvette, France
14 Université Paris Diderot, AIM, Sorbonne Paris Cité, CEA, CNRS, 91191 Gif-sur-Yvette, France
15 Dept. Física Teórica y del Cosmos, Universidad de Granada, Granada, Spain
16 Instituto Universitario Carlos I de Física Teórica y Computacional, Universidad de Granada, Granada, Spain
17 Centre for Astrophysics Research, University of Hertfordshire, College Lane, Hatfield AL10 9AB, UK
18 Leiden Observatory, Leiden University, PO Box 9513, 2300 RA Leiden, The Netherlands
19 Department of Astronomy, University of Massachusetts, Amherst, MA 01003, USA
20 Department of Astronomy, The Ohio State University, 4051 McPherson Laboratory, 140 West 18th Avenue, Columbus, OH 43210, USA
21 Illumination Works LLC, 5650 Blazer Parkway, Suite 152, Dublin, OH 43017, USA
22 Princeton University Observatory, Peyton Hall, Princeton, NJ 08544-1001, USA
23 European Southern Observatory, Karl-Schwarzschild-Strasse 2, 85748 Garching, Germany
24 Space Telescope Science Institute, 3700 San Martin Dr., Baltimore, MD 21218, USA
25 Research School of Astronomy and Astrophysics, The Australian National University, Canberra, ACT 2611, Australia
26 IPAC, California Institute of Technology, 1200 E. California Blvd, Pasadena, CA 91125, USA
27 Max-Planck-Institut für Extraterrestrische Physik, Giessenbachstr., 85748 Garching, Germany
28 Department of Physics and Astronomy, Stony Brook University, Stony Brook, NY 11794-3800, USA
29 Department of Astronomy, Indiana University, Bloomington, IN 47404, USA
30 Center for Astrophysics and Space Sciences, Department of Physics, University of California, San Diego, 9500 Gilman Drive, La Jolla, CA 92093, USA
31 Department of Physics & Astronomy, University of Toledo, 2801 W. Bancroft Street, Toledo, OH 43606, USA
32 Department of Physics and Astronomy, McMaster University, 1280 Main St. W., Hamilton, Ontario L8S 4M1, Canada

Appendix A: Best-fit SED results

The physical quantities from the best-fit SED models are reported in Tables A.1–A.3 for CIGALE, GRASIL, and MAGPHYS, respectively. The best-fit SEDs where each model is plotted together with the multiwavelength photometry are shown in Fig. 1 for NGC 5457 (M 101) in the main text, and here in Fig. A.1 for the remaining galaxies.

Table A.1. CIGALE quantities for KINGFISH sample.

Galaxy	rms (dex)	Log(M_{star}) ($M_\odot$)	Log(SFR) ($M_\odot$ yr^{-1})	Log(M_{dust}) ($M_\odot$)	Log(L_{TIR}) ($L_\odot$)	Log(L_{FUV}) ($L_\odot$)	A_V (mag)	A_{FUV} (mag)
DDO 053	0.224	6.784	−2.430	3.763	7.012	7.413	0.072	0.362
DDO 154	0.086	7.019	−2.092	5.056	6.980	7.753	0.030	0.139
DDO 165	0.065	7.705	−1.780	5.594	7.395	8.058	0.031	0.171
Ho I	0.072	7.435	−2.056	4.801	6.937	7.730	0.037	0.157
Ho II	0.161	8.245	−1.375	4.686	7.862	8.332	0.054	0.293
IC 0342	0.161	10.104	0.437	7.589	10.197	10.260	0.189	1.009
IC 2574	0.259	8.457	−1.136	6.016	8.230	8.613	0.072	0.368
M81 Dw B	0.052	7.130	−2.517	4.379	6.562	6.996	0.076	0.306
NGC 0337	0.035	9.721	0.191	7.403	10.026	10.034	0.200	1.369
NGC 0584	0.107	10.802	−2.851	6.716	8.528	8.033	0.017	0.064
NGC 0628	0.022	9.821	0.031	7.605	9.843	9.861	0.183	1.175
NGC 0855	0.056	8.867	−1.669	5.912	8.523	8.427	0.203	1.109
NGC 0925	0.095	9.598	−0.028	7.386	9.599	9.735	0.133	0.790
NGC 1097	0.008	10.722	0.694	7.968	10.620	10.427	0.502	2.026
NGC 1266	0.066	9.984	0.163	7.074	10.330	10.039	1.199	6.189
NGC 1291	0.045	10.866	−1.094	7.446	9.370	8.876	0.080	0.476
NGC 1316	0.080	11.581	−1.343	7.147	9.796	8.991	0.047	0.195
NGC 1377	0.172	9.770	0.104	6.233	10.122	9.981	0.593	2.669
NGC 1404	0.034	11.059	−2.354	6.959	8.878	8.435	0.025	0.101
NGC 1482	0.041	10.048	0.627	7.405	10.683	10.487	1.159	5.903
NGC 1512	0.049	10.119	−0.217	7.346	9.541	9.482	0.210	0.950
NGC 2146	0.068	10.516	0.920	7.812	11.071	10.879	1.151	5.227
NGC 2798	0.128	10.121	0.265	7.216	10.536	10.349	0.894	4.278
NGC 2841	0.030	10.862	−0.180	7.836	10.018	9.677	0.218	1.237
NGC 2915	0.154	8.102	−1.516	4.931	7.558	8.004	0.078	0.291
NGC 2976	0.023	8.974	−0.821	6.291	8.904	8.848	0.258	1.487
NGC 3049	0.054	9.346	−0.290	6.805	9.528	9.490	0.263	1.573
NGC 3077	0.042	9.201	−1.093	5.994	8.880	8.728	0.293	1.389
NGC 3184	0.048	10.090	0.303	7.739	9.951	9.963	0.221	1.090
NGC 3190	0.047	10.517	−1.143	7.251	9.830	8.758	0.409	1.951
NGC 3198	0.051	9.989	0.221	7.635	9.892	9.881	0.248	1.153
NGC 3265	0.052	9.245	−0.606	6.353	9.370	9.197	0.493	2.677
NGC 3351	0.035	10.224	−0.067	7.209	9.847	9.643	0.347	1.703
NGC 3521	0.013	10.679	0.279	7.927	10.523	10.191	0.549	2.380
NGC 3621	0.044	9.832	0.052	7.281	9.876	9.850	0.254	1.372
NGC 3627	0.014	10.485	0.447	7.737	10.388	10.175	0.454	2.288
NGC 3773	0.068	8.717	−0.933	5.968	8.723	8.886	0.115	0.727
NGC 3938	0.025	10.194	0.429	7.653	10.235	10.229	0.217	1.264
NGC 4236	0.161	8.966	−0.670	6.461	8.594	9.036	0.055	0.314
NGC 4254	0.011	10.312	0.645	7.956	10.565	10.475	0.354	2.031
NGC 4321	0.011	10.516	0.763	7.890	10.493	10.364	0.386	1.858
NGC 4536	0.033	10.167	0.339	7.555	10.291	10.149	0.471	2.147
NGC 4559	0.069	9.484	−0.253	7.168	9.396	9.515	0.142	0.804
NGC 4569	0.016	10.201	−1.382	7.100	9.711	9.297	0.338	1.646
NGC 4579	0.061	10.829	−0.525	7.728	9.969	9.484	0.242	1.228
NGC 4594	0.002	11.082	−1.676	7.308	9.494	8.580	0.083	0.378
NGC 4625	0.046	8.866	−0.885	6.490	8.703	8.814	0.151	0.814
NGC 4631	0.081	9.995	0.365	7.670	10.316	10.235	0.444	1.758
NGC 4725	0.059	10.634	−0.199	7.814	9.829	9.604	0.194	0.999
NGC 4736	0.000	10.215	−0.556	6.852	9.746	9.452	0.310	1.415
NGC 4826	0.023	10.245	−1.101	6.688	9.588	9.077	0.320	1.682
NGC 5055	0.019	10.488	0.161	8.025	10.238	9.995	0.414	1.983
NGC 5398	0.167	8.490	−1.107	5.820	8.542	8.734	0.111	0.669

Table A.1. continued.

Galaxy	rms (dex)	Log(M_{star}) ($M_\odot$)	Log(SFR) ($M_\odot$ yr^{-1})	Log(M_{dust}) ($M_\odot$)	Log(L_{TIR}) ($L_\odot$)	Log(L_{FUV}) ($L_\odot$)	A_V (mag)	A_{FUV} (mag)
NGC 5408	0.216	8.081	−1.271	4.844	8.164	8.570	0.067	0.368
NGC 5457	0.072	10.274	0.536	8.023	10.280	10.336	0.183	1.000
NGC 5474	0.026	8.944	−0.802	6.443	8.630	9.025	0.050	0.357
NGC 5713	0.050	10.117	0.505	7.542	10.491	10.348	0.527	2.872
NGC 5866	0.038	10.612	−1.234	7.028	9.646	8.682	0.219	1.593
NGC 6946	0.083	10.328	0.663	7.642	10.540	10.480	0.297	1.762
NGC 7331	0.011	10.841	0.619	8.096	10.678	10.366	0.606	2.705
NGC 7793	0.080	9.288	−0.452	7.010	9.222	9.367	0.138	0.740

Table A.2. GRASIL quantities for KINGFISH sample.

Galaxy	Geometry	rms (dex)	Log(M_{star}) ($M_\odot$)	Log(SFR) ($M_\odot$ yr^{-1})	Log(M_{dust}) ($M_\odot$)	Log(L_{TIR}) ($L_\odot$)	Log(L_{FUV}) ($L_\odot$)	A_V (mag)	A_{FUV} (mag)
DDO 053	NSD	0.111	6.500	−2.318	4.174	6.951	7.439	0.037	0.260
DDO 154	NSS	0.054	6.880	−1.992	5.240	7.431	7.854	0.070	0.405
DDO 165	NSS	0.068	7.403	−1.499	5.712	8.331	8.321	0.188	1.134
Ho I	NSS	0.145	7.163	−2.180	5.078	7.043	7.556	0.022	0.253
Ho II	NSS	0.090	7.824	−1.392	5.044	7.847	8.397	0.019	0.253
IC 0342	NSD	0.108	9.826	0.506	7.926	10.186	10.236	0.161	0.704
IC 2574	NSS	0.105	8.236	−1.077	6.353	8.308	8.684	0.056	0.503
M81 Dw B	NSS	0.097	6.855	−2.620	4.666	6.601	7.070	0.023	0.316
NGC 0337	NSD	0.058	9.421	0.266	7.392	10.048	10.005	0.179	1.245
NGC 0584	NSS	0.375	10.594	−0.514	7.006	9.049	9.274	0.011	0.681
NGC 0628	NSD	0.064	9.584	0.122	7.702	9.819	9.835	0.113	0.801
NGC 0855	NSD	0.083	8.695	−1.129	6.036	8.551	8.582	0.056	1.039
NGC 0925	NSS	0.079	9.397	0.050	7.768	9.576	9.839	0.106	0.610
NGC 1097	NSD	0.048	10.573	0.724	8.268	10.591	10.433	0.260	1.846
NGC 1266	NSS	0.118	10.104	0.146	7.087	10.495	9.882	1.451	5.503
NGC 1291	NSS	0.155	10.790	−0.102	7.852	9.427	9.600	0.019	0.804
NGC 1316	NSS	0.224	11.410	0.279	7.732	10.080	10.068	0.021	1.316
NGC 1377	NSS	0.081	9.557	0.199	6.826	10.102	9.950	0.455	3.922
NGC 1404	NSD	0.052	10.696	0.206	7.259	10.149	9.974	0.160	3.690
NGC 1482	NSS	0.086	10.081	0.522	7.772	10.650	10.219	1.226	5.002
NGC 1512	NSS	0.062	9.921	−0.082	7.815	9.505	9.599	0.125	0.895
NGC 2146	NSD	0.092	10.361	1.010	7.871	11.081	10.743	1.121	4.677
NGC 2798	NSD	0.069	9.966	0.513	7.320	10.573	10.272	0.948	4.251
NGC 2841	NSS	0.103	10.958	0.196	8.251	9.956	9.929	0.057	1.356
NGC 2915	NSS	0.067	7.694	−1.599	5.195	7.590	8.141	0.018	0.256
NGC 2976	NSD	0.073	8.746	−0.901	6.657	8.845	8.812	0.108	1.181
NGC 3049	NSS	0.056	9.205	−0.286	7.537	9.534	9.487	0.172	1.549
NGC 3077	NSS	0.070	9.001	−0.884	6.511	8.849	8.799	0.093	1.725
NGC 3184	NSD	0.066	9.921	0.273	7.963	9.920	9.936	0.117	0.767
NGC 3190	NSD	0.104	10.612	−0.065	7.773	9.821	9.600	0.194	3.347
NGC 3198	NSD	0.052	9.798	0.202	7.897	9.860	9.874	0.118	0.868
NGC 3265	NSS	0.063	9.169	−0.501	6.875	9.394	9.259	0.282	2.781
NGC 3351	NSS	0.055	10.043	−0.078	7.463	9.810	9.673	0.208	1.693
NGC 3521	NSS	0.104	10.596	0.583	8.396	10.476	10.269	0.315	2.211
NGC 3621	NSD	0.064	9.509	0.065	7.598	9.816	9.801	0.193	0.880
NGC 3627	NSS	0.080	10.332	0.474	7.935	10.366	10.178	0.343	2.022
NGC 3773	NSS	0.059	8.353	−0.848	6.344	8.748	8.849	0.118	0.993
NGC 3938	NSD	0.065	10.001	0.443	7.970	10.178	10.167	0.127	0.848
NGC 4236	NSS	0.088	8.666	−0.615	6.699	8.620	9.139	0.023	0.262
NGC 4254	NSD	0.089	10.084	0.631	8.131	10.516	10.373	0.315	1.345
NGC 4321	NSS	0.098	10.407	0.589	8.189	10.415	10.318	0.324	1.215
NGC 4536	NSD	0.067	10.059	0.424	7.691	10.288	10.132	0.311	1.907
NGC 4559	NSD	0.049	9.196	−0.220	7.328	9.397	9.509	0.081	0.655
NGC 4569	NSS	0.102	10.172	−0.159	7.382	9.681	9.606	0.068	2.034

Table A.2. continued.

Galaxy	Geometry	rms (dex)	Log($M_{\rm star}$) ($M_\odot$)	Log(SFR) ($M_\odot\,{\rm yr}^{-1}$)	Log($M_{\rm dust}$) ($M_\odot$)	Log($L_{\rm TIR}$) ($L_\odot$)	Log($L_{\rm FUV}$) ($L_\odot$)	A_V (mag)	$A_{\rm FUV}$ (mag)
NGC 4579	NSS	0.094	10.825	0.197	8.007	9.988	9.903	0.055	1.958
NGC 4594	NSS	0.240	11.083	−0.048	7.349	9.646	9.726	0.029	1.742
NGC 4625	NSS	0.065	8.658	−0.893	6.705	8.663	8.836	0.146	0.611
NGC 4631	NSS	0.059	9.749	0.460	7.933	10.296	10.200	0.506	1.321
NGC 4725	NSS	0.099	10.719	0.099	8.149	9.774	9.829	0.071	0.974
NGC 4736	NSS	0.062	10.086	−0.102	7.190	9.726	9.627	0.150	1.519
NGC 4826	NSS	0.074	10.144	−0.308	7.004	9.589	9.450	0.108	2.301
NGC 5055	NSS	0.093	10.400	0.384	8.276	10.203	10.055	0.290	1.634
NGC 5398	NSS	0.111	8.108	−0.957	6.196	8.536	8.773	0.084	0.751
NGC 5408	NSS	0.212	7.983	−1.540	5.572	8.313	8.208	0.234	2.135
NGC 5457	NSD	0.048	9.991	0.563	8.118	10.265	10.288	0.115	0.748
NGC 5474	NSS	0.075	8.686	−0.684	6.776	8.625	9.069	0.035	0.335
NGC 5713	NSS	0.072	10.009	0.507	7.824	10.464	10.196	0.665	2.312
NGC 5866	NSS	0.112	10.744	−0.228	7.172	9.724	9.538	0.057	2.949
NGC 6946	NSD	0.101	10.054	0.676	7.886	10.497	10.433	0.247	1.287
NGC 7331	NSD	0.090	10.829	0.707	8.549	10.638	10.374	0.354	2.423
NGC 7793	NSD	0.058	9.018	−0.368	7.189	9.201	9.345	0.109	0.578

Table A.3. `MAGPHYS` quantities for KINGFISH sample.

Galaxy	rms (dex)	Log($M_{\rm star}$) ($M_\odot$)	Log(SFR) ($M_\odot\,{\rm yr}^{-1}$)	Log($M_{\rm dust}$) ($M_\odot$)	Log($L_{\rm TIR}$) ($L_\odot$)	Log($L_{\rm FUV}$) ($L_\odot$)	A_V (mag)	$A_{\rm FUV}$ (mag)
DDO 053	0.096	6.488	−2.352	3.638	7.039	7.467	0.060	0.304
DDO 154	0.059	6.870	−2.140	4.105	7.369	7.738	0.018	0.334
DDO 165	0.063	7.405	−3.095	4.305	8.289	8.264	0.190	1.095
Ho I	0.086	7.368	−2.232	4.568	7.045	7.710	0.039	0.143
Ho II	0.072	8.254	−1.646	4.254	7.870	8.370	0.062	0.189
IC 0342	0.115	9.817	−0.483	7.217	10.147	10.136	0.350	0.901
IC 2574	0.073	8.443	−1.257	5.743	8.358	8.680	0.073	0.341
M81 Dw B	0.071	7.098	−3.102	3.998	6.604	6.883	0.054	0.359
NGC 0337	0.061	9.457	−0.043	6.857	10.076	9.975	0.342	1.449
NGC 0584	0.099	10.722	−2.178	7.622	8.900	8.307	0.024	0.365
NGC 0628	0.041	10.100	0.100	7.000	9.855	9.774	0.382	1.058
NGC 0855	0.057	8.962	−1.438	5.562	8.633	8.525	0.148	1.060
NGC 0925	0.049	9.406	−0.194	6.906	9.591	9.628	0.204	0.758
NGC 1097	0.041	10.490	0.490	7.490	10.619	10.359	0.479	1.877
NGC 1266	0.103	10.157	−0.343	6.657	10.385	9.571	1.660	4.969
NGC 1291	0.066	10.720	−0.980	6.920	9.395	8.843	0.062	0.534
NGC 1316	0.098	11.330	−1.270	6.630	9.890	8.878	0.041	0.542
NGC 1377	0.112	9.768	0.068	5.868	10.139	9.936	0.631	2.373
NGC 1404	0.081	10.796	−1.204	6.796	9.610	8.538	0.099	0.484
NGC 1482	0.056	10.094	0.094	7.094	10.648	9.980	1.713	4.992
NGC 1512	0.041	10.015	−0.485	7.115	9.531	9.420	0.179	0.921
NGC 2146	0.055	10.457	0.757	7.257	11.060	10.607	1.687	4.749
NGC 2798	0.059	10.109	0.209	6.809	10.548	10.151	1.319	3.953
NGC 2841	0.057	10.784	−0.316	7.384	9.979	9.607	0.171	1.130
NGC 2915	0.069	7.741	−1.559	4.741	7.615	8.258	0.033	0.162
NGC 2976	0.038	8.986	−1.214	5.986	8.906	8.760	0.268	1.301
NGC 3049	0.053	9.252	−0.448	6.552	9.618	9.471	0.418	1.543
NGC 3077	0.047	9.152	−1.348	5.652	8.868	8.601	0.231	1.318
NGC 3184	0.056	10.022	−0.078	7.322	9.893	9.891	0.127	1.034
NGC 3190	0.047	10.357	−1.243	6.957	9.793	8.633	0.312	1.777
NGC 3198	0.044	9.884	−0.116	7.184	9.878	9.802	0.246	1.060
NGC 3265	0.036	9.270	−0.830	5.870	9.417	9.050	0.676	2.400
NGC 3351	0.038	10.225	−0.375	6.825	9.844	9.548	0.301	1.575
NGC 3521	0.049	10.584	0.084	7.584	10.477	9.933	0.518	2.234
NGC 3621	0.053	9.618	−0.382	6.918	9.829	9.693	0.359	1.400

Table A.3. continued.

Galaxy	rms (dex)	Log(M_{star}) ($M_\odot$)	Log(SFR) ($M_\odot\,\text{yr}^{-1}$)	Log(M_{dust}) ($M_\odot$)	Log(L_{TIR}) ($L_\odot$)	Log(L_{FUV}) ($L_\odot$)	A_V (mag)	A_{FUV} (mag)
NGC 3627	0.047	10.530	−0.070	7.230	10.376	9.878	0.553	2.097
NGC 3773	0.045	8.572	−1.028	5.572	8.768	8.873	0.116	0.752
NGC 3938	0.049	10.191	0.091	7.291	10.164	10.072	0.218	1.149
NGC 4236	0.070	8.882	−0.618	6.182	8.628	9.087	0.054	0.246
NGC 4254	0.043	10.202	0.502	7.502	10.514	10.288	0.652	1.804
NGC 4321	0.059	10.396	0.396	7.496	10.449	10.288	0.282	1.592
NGC 4536	0.050	10.108	0.208	7.108	10.333	10.135	0.492	2.037
NGC 4559	0.045	9.373	−0.627	6.673	9.403	9.429	0.224	0.771
NGC 4569	0.046	9.873	−0.827	6.673	9.661	9.039	0.261	1.493
NGC 4579	0.053	10.815	−0.485	7.115	9.980	9.393	0.210	1.289
NGC 4594	0.070	11.002	−1.298	6.902	9.527	8.665	0.065	0.783
NGC 4625	0.050	8.523	−1.277	5.823	8.654	8.670	0.186	0.737
NGC 4631	0.064	9.650	0.350	7.250	10.344	10.229	0.421	1.978
NGC 4725	0.056	10.637	−0.463	7.337	9.813	9.494	0.171	0.983
NGC 4736	0.029	10.222	−0.478	6.422	9.702	9.478	0.177	1.317
NGC 4826	0.050	10.229	−0.971	6.329	9.563	8.944	0.244	1.445
NGC 5055	0.035	10.385	−0.015	7.385	10.205	9.916	0.354	1.756
NGC 5398	0.088	8.054	−1.246	5.754	8.604	8.735	0.059	0.725
NGC 5408	0.077	8.048	−1.652	4.548	8.279	8.391	0.063	0.615
NGC 5457	0.051	10.238	0.338	7.538	10.221	10.298	0.164	0.762
NGC 5474	0.040	8.751	−0.949	6.051	8.623	8.950	0.075	0.319
NGC 5713	0.061	9.946	0.246	7.046	10.477	10.143	0.765	2.728
NGC 5866	0.051	10.655	−2.045	6.455	9.677	8.273	0.198	0.745
NGC 6946	0.067	10.151	−0.349	7.351	10.493	10.293	0.560	1.451
NGC 7331	0.048	10.808	0.308	7.708	10.628	10.186	0.531	2.215
NGC 7793	0.058	8.970	−0.530	6.470	9.213	9.291	0.178	0.742
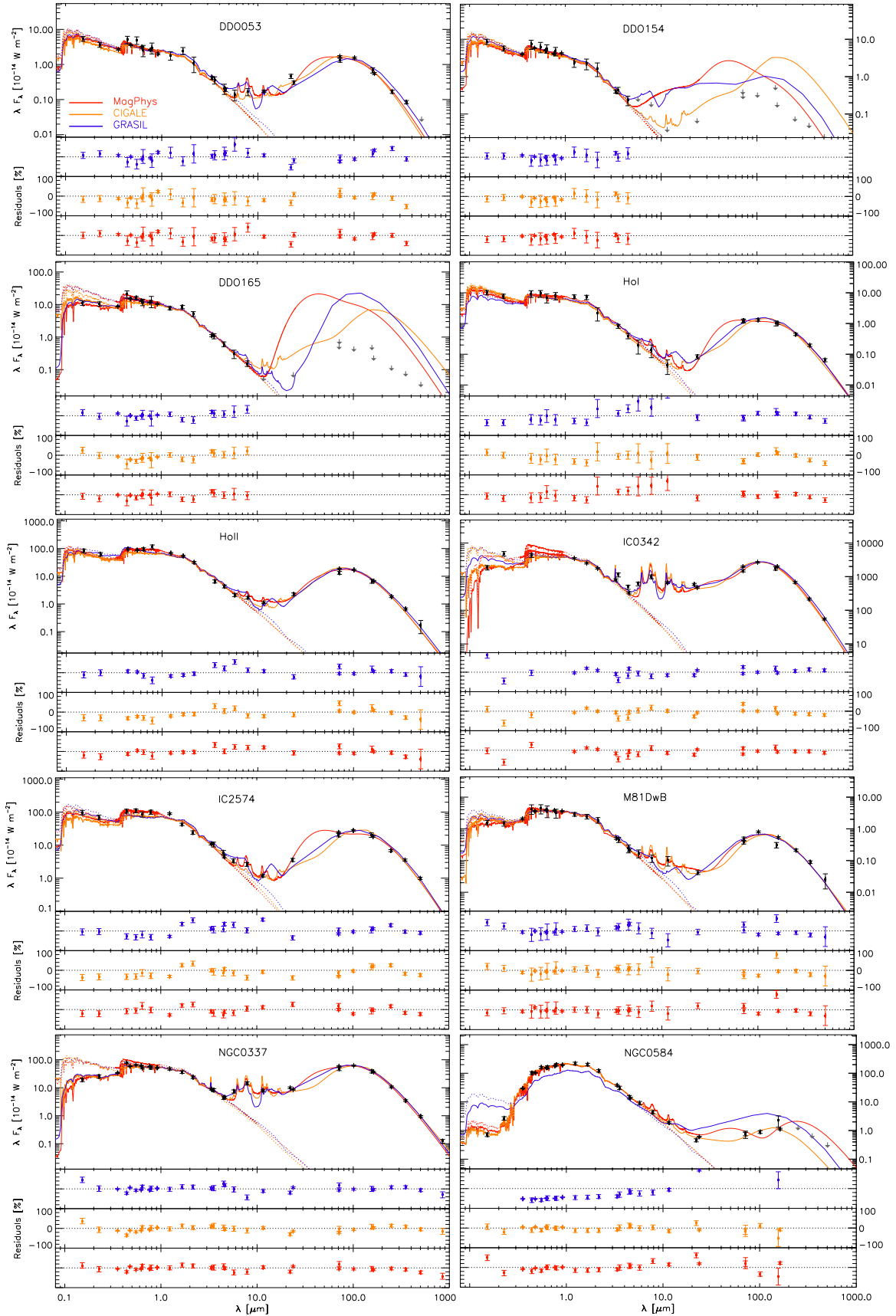
Fig. A.1. Panchromatic SEDs for the KINGFISH galaxies based on the photometry measurements from Dale et al. (2017) overlaid with the best-fitting SED models inferred from the SED fitting tools MAGPHYS (red curve), CIGALE (dark-orange curve) and GRASIL (blue curve). The dashed curves represent the (unattenuated) intrinsic model emission for each SED fitting method (using the same color coding). The bottom part of each panel shows the residuals for each of these models compared to the observed fluxes in each waveband. Gray arrows points show the upper limits when available.
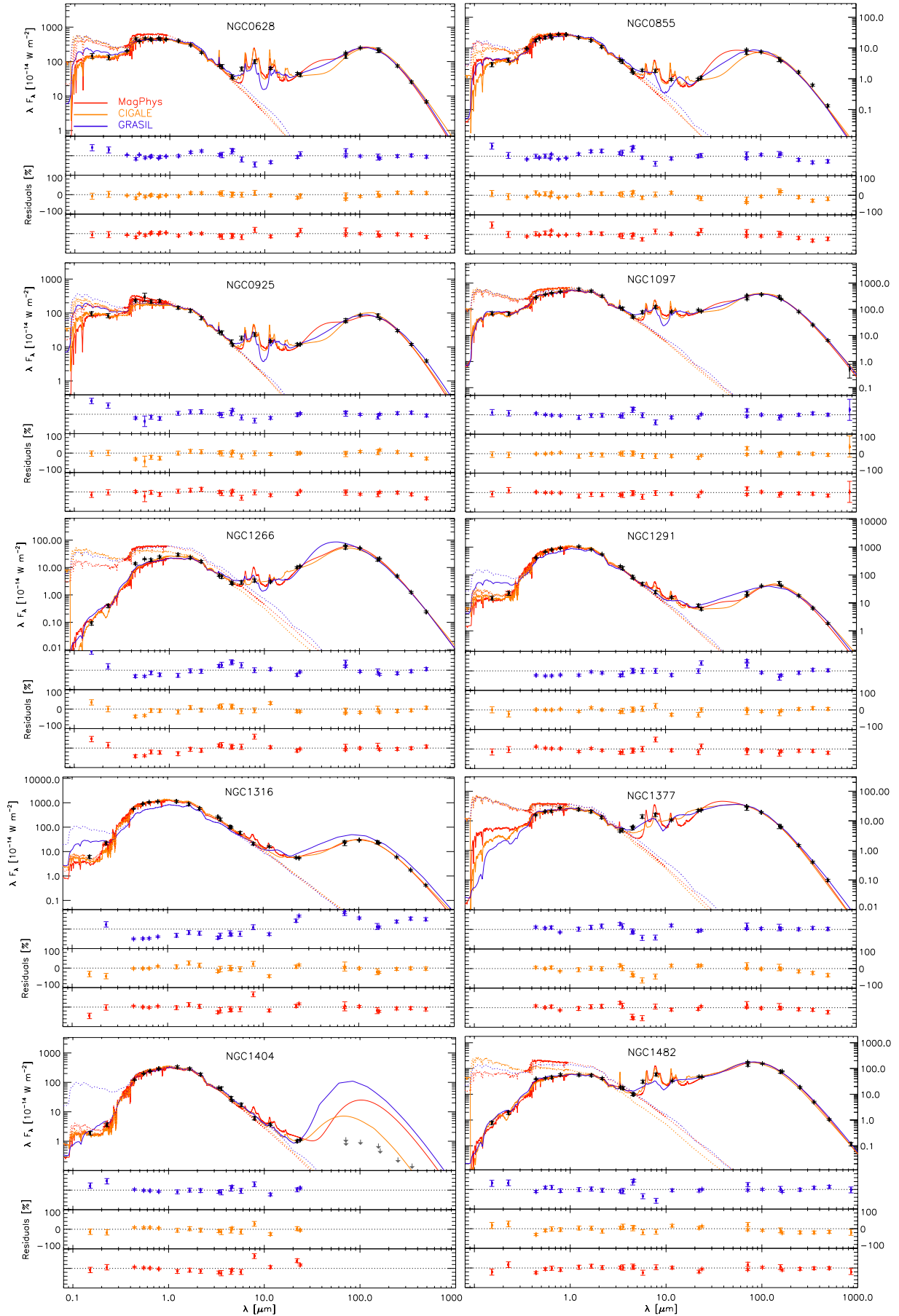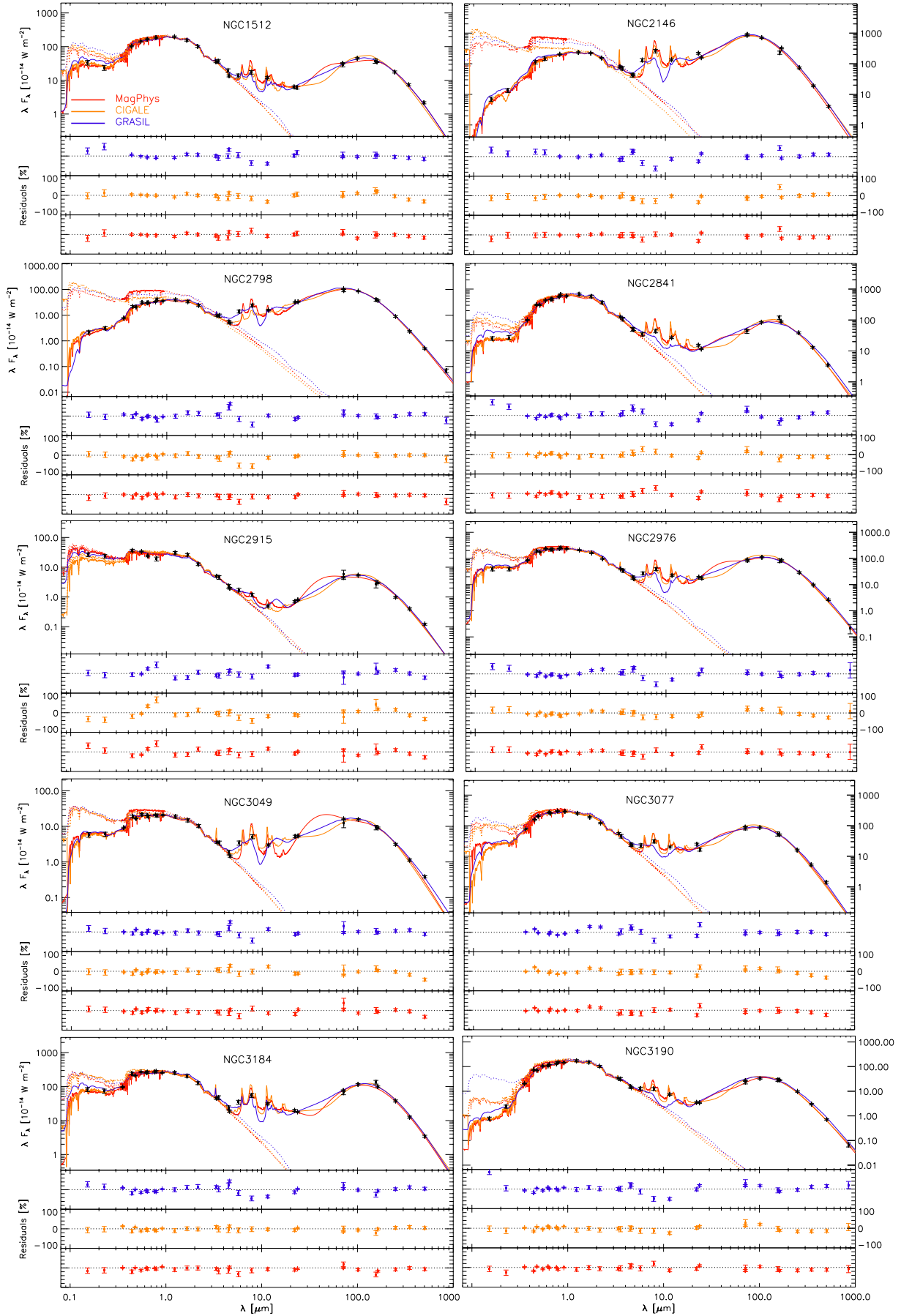
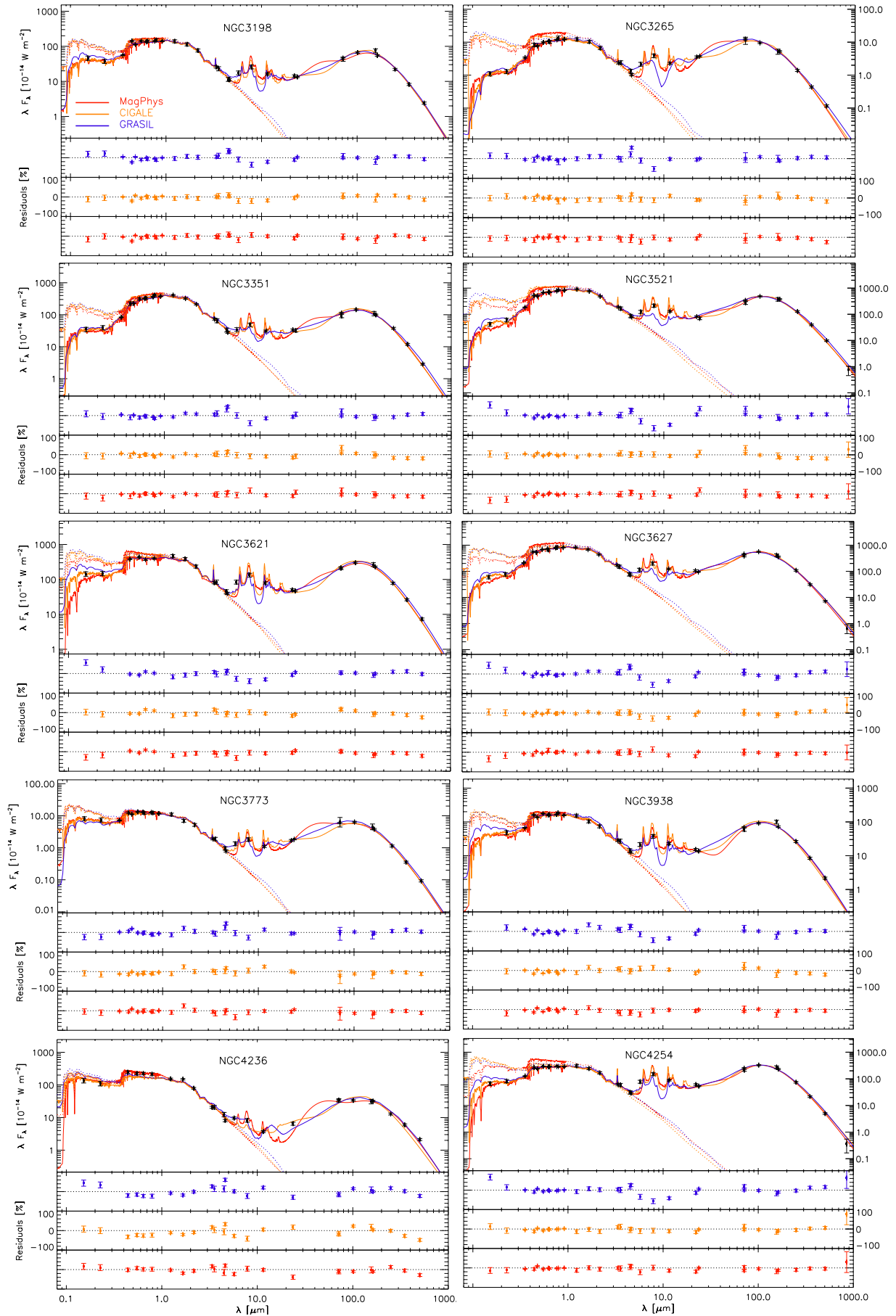**Fig. A.1.** continued.

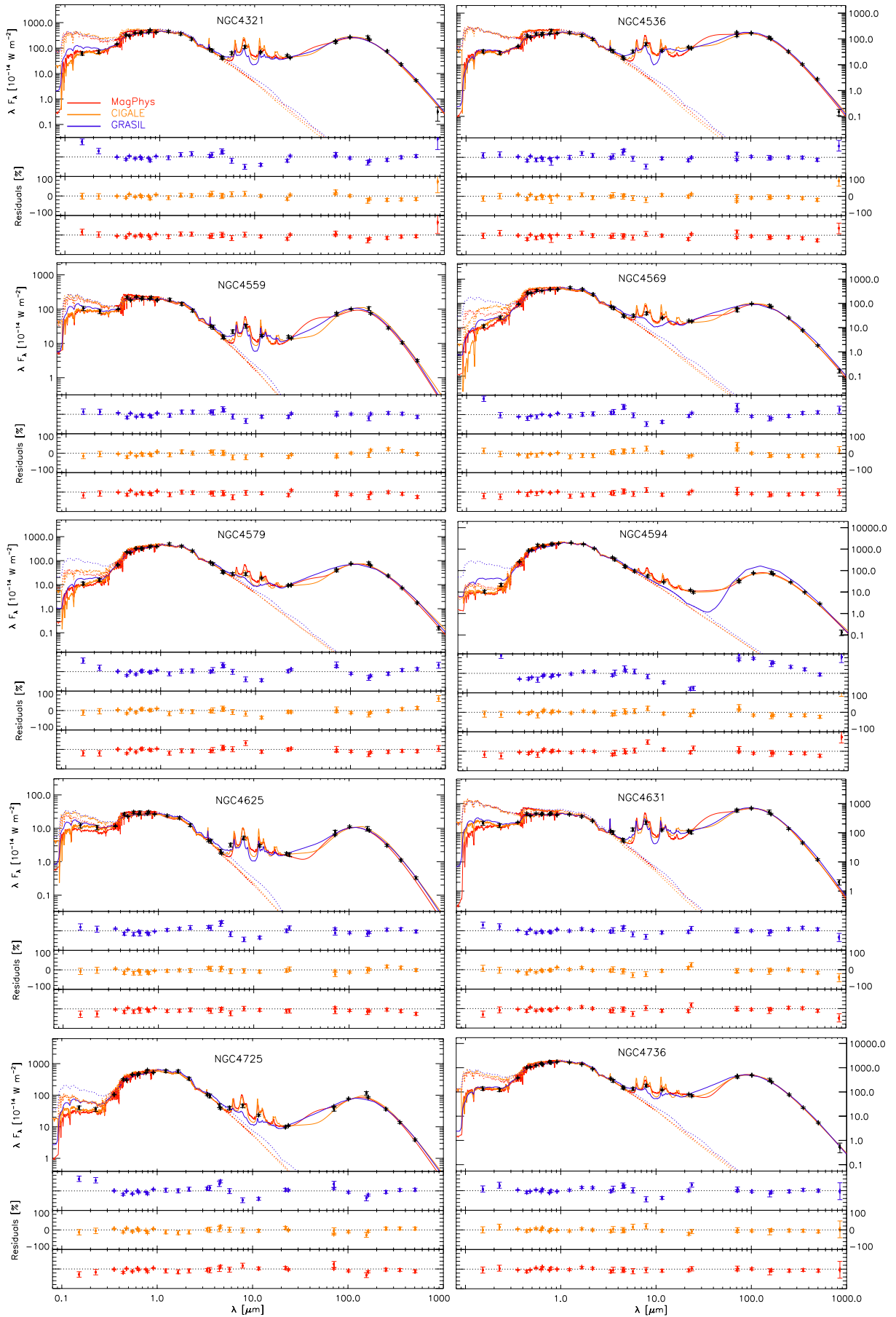**Fig. A.1.** continued.

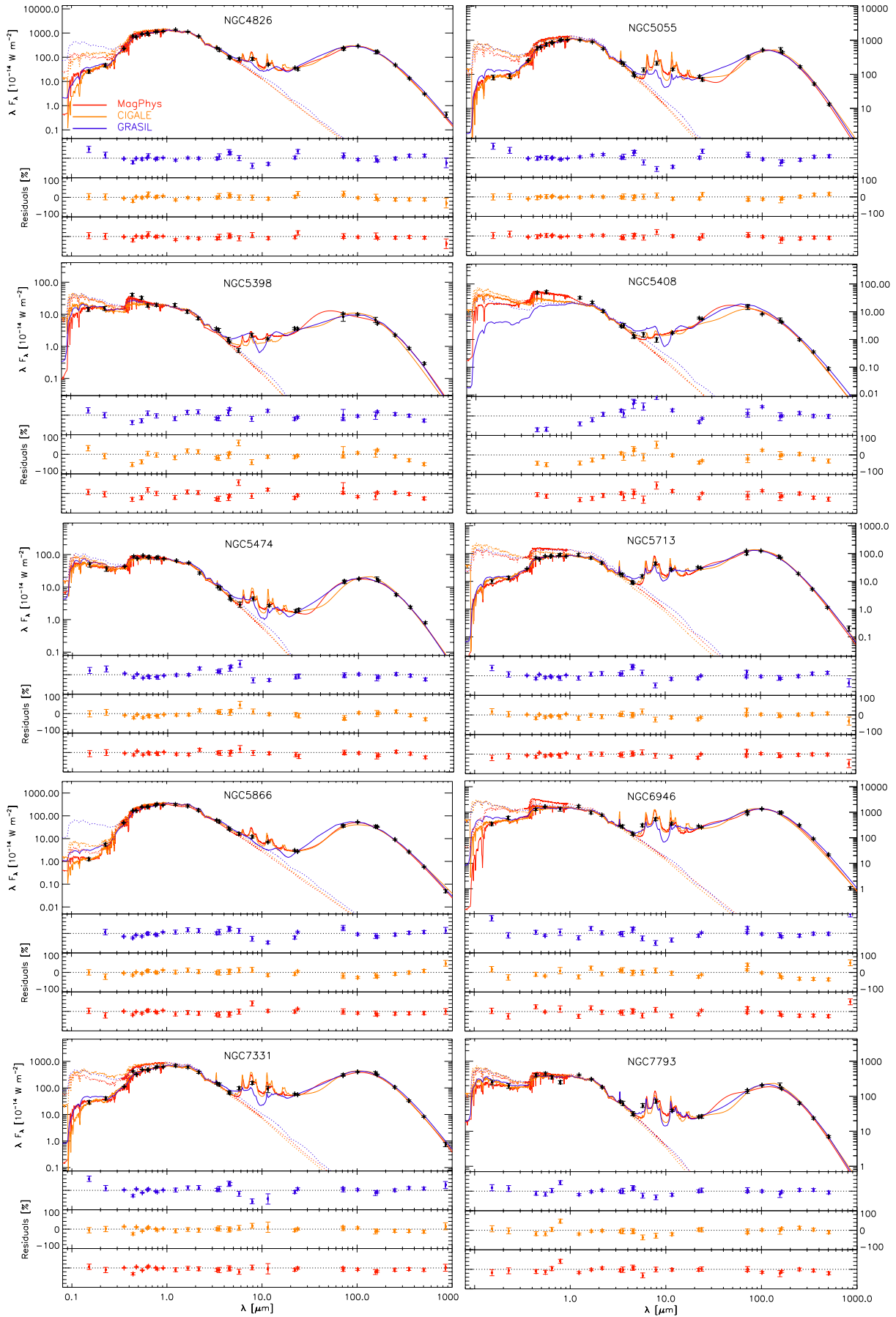**Fig. A.1.** continued.

Fig. A.1. continued.

Fig. A.1. continued.

Appendix B: Description of reference quantities

Here we describe in detail our choices for the inference of the six reference or recipe quantities introduced in Sect. 3.2. All photometry from Dale et al. (2017) has been corrected for foreground Galactic extinction according to A_V measurements by Schlafly & Finkbeiner (2011) and the extinction curve of Draine (2003). A summary of the methods is given in Table B.1, and the values of the computed quantities are reported in Table B.2.

Table B.1. Summary of methods for independently-derived quantities.

Parameter	Method	Reference
Stellar mass, M_{star}	$3.6\,\mu m$ luminosity[a]	Wen et al. (2013)
Stellar mass, M_{star}	$3.6\,\mu m$ luminosity, constant $\Upsilon^{[3.6]}$	McGaugh & Schombert (2014)
Star-formation rate, SFR	FUV+TIR[b]	Murphy et al. (2011)
Star-formation rate, SFR	Hα+24 μm	Kennicutt et al. (2009), Moustakas et al. (2010), Skibba et al. (2011), see text
Dust mass, M_{dust}	Modified blackbody fits	As in (Bianchi 2013), see text
Dust mass, M_{dust}	DL07 model fits	(Aniano et al., in prep.)
Total IR luminosity, L_{TIR}	*Spitzer* data[c]	Draine & Li (2007)
Total IR luminosity, L_{TIR}	*Spitzer+Herschel* data[d]	Galametz et al. (2013)
FUV attenuation, A_{FUV}	IRX, logarithm of ratio of IR and observed FUV fluxes	Murphy et al. (2011)

Notes. [a]Assuming IRAC flux = WISE W1 flux (±5%); [b]if not available, then SFR(FUV), or as last choice SFR(TIR); [c]based on a linear combination IRAC $8\,\mu m$, MIPS $24\,\mu m$, MIPS $70\,\mu m$, and MIPS $160\,\mu m$ luminosities; [d]based on a linear combination MIPS $24\,\mu m$, PACS $70\,\mu m$, and PACS $100\,\mu m$ luminosities.

Table B.2. Independently-derived quantities for KINGFISH sample.

Galaxy	MW A_V (mag)	Hubble type	Distance (Mpc)	12+ log(O/H) (PP04N2)	Log(M_{star})[a] ($M_\odot$)	Log(SFR) (FUV+TIR) ($M_\odot\,yr^{-1}$)	Log(SFR) (Hα+24μm) ($M_\odot\,yr^{-1}$)	Log(M_{dust}) ($M_\odot$)	Log(L_{TIR}) ($L_\odot$)	Log(L_{FUV}) ($L_\odot$)	A_{FUV} (mag)
DDO 053	0.10	10	3.61	8.00	6.919	−2.372	−2.285	3.954	7.088	7.347	0.231
DDO 154	0.03	10	4.30	8.02	7.156	−2.097	−2.562	–	–	7.701	–
DDO 165	0.07	10	4.57	8.04	7.625	−1.934	−2.658	–	–	7.863	–
Ho I	0.14	10	3.90	8.04	7.356	−2.068	−2.282	4.901	7.004	7.686	0.093
Ho II	0.09	10	3.05	8.13	8.070	−1.363	−1.342	4.762	7.951	8.383	0.160
IC 0342	1.53	6	3.28	8.80	10.550	0.320	0.272	7.644	10.216	9.798	0.819
IC 2574	0.10	9	3.79	8.19	8.577	−1.071	−1.068	5.889	8.341	8.645	0.210
M81 Dw B	0.22	10	3.60	8.19	7.028	−2.888	−2.729	4.331	6.693	6.810	0.308
NGC 0337	0.31	7	19.30	8.47	9.927	0.090	0.256	7.284	10.115	9.351	1.359
NGC 0584	0.12	−4	20.80	8.69	10.782	−1.053	–	7.216	8.554	7.989	1.029
NGC 0628	0.19	5	7.20	8.80	10.015	−0.028	−0.027	7.443	9.862	9.380	0.906
NGC 0855	0.19	−5	9.73	8.43	9.121	−1.368	−1.182	5.913	8.614	7.935	1.212
NGC 0925	0.21	7	9.12	8.59	9.776	−0.143	−0.131	7.335	9.590	9.398	0.556
NGC 1097	0.07	3	14.20	8.75	10.796	0.601	0.625	7.935	10.662	9.647	1.841
NGC 1266	0.27	−2	30.60	8.52	10.263	0.253	0.296	7.039	10.478	7.429	6.708
NGC 1291	0.04	1	10.40	8.78	10.940	−0.495	−0.799	7.270	9.372	8.706	1.190
NGC 1316	0.06	−2	21.00	9.31	11.657	−0.082	−0.296	7.113	9.882	8.925	1.724
NGC 1377	0.08	−1	24.60	8.52	10.083	0.299	0.394	6.306	10.191	–	–
NGC 1404	0.03	−4	20.20	8.78	11.066	−1.413	−0.528	–	–	8.384	–
NGC 1482	0.11	−2	22.60	8.74	10.592	0.548	0.667	7.463	10.733	8.097	5.679
NGC 1512	0.03	2	11.60	8.72	10.150	−0.314	−0.464	7.346	9.517	9.151	0.752
NGC 2146	0.26	2	17.20	8.68	10.793	1.001	0.900	7.771	11.120	8.815	4.859
NGC 2798	0.06	1	25.80	8.72	10.444	0.450	0.657	7.208	10.629	8.657	4.040
NGC 2841	0.04	3	14.10	9.31	10.802	0.072	−0.181	7.836	9.957	9.199	1.349
NGC 2915	0.75	10	3.78	8.17	8.200	−1.651	−1.629	4.912	7.634	8.077	0.157
NGC 2976	0.20	5	3.55	8.61	9.054	−1.068	−0.999	6.362	8.897	8.197	1.248
NGC 3049	0.10	2	19.20	8.72	9.530	−0.437	−0.191	6.817	9.612	8.828	1.395
NGC 3077	0.18	10	3.83	8.64	9.245	−0.925	−1.027	6.064	8.884	–	–
NGC 3184	0.05	6	11.70	8.81	10.263	0.137	0.024	7.575	9.947	9.548	0.794

Notes. − corresponds to unavailable data, so missing quantity. [a]Values according to the Wen et al. (2013) formulation.

Table B.2. continued.

Galaxy	MW A_V (mag)	Hubble type	Distance (Mpc)	12+ log(O/H) (PP04N2)	Log(M_{star})[a] ($M_\odot$)	Log(SFR) (FUV+TIR) ($M_\odot$ yr^{-1})	Log(SFR) (Hα+24μm) ($M_\odot$ yr^{-1})	Log(M_{dust}) ($M_\odot$)	Log(L_{TIR}) ($L_\odot$)	Log(L_{FUV}) ($L_\odot$)	A_{FUV} (mag)
NGC 3190	0.07	1	19.30	8.75	10.720	−0.251	−0.602	7.358	9.807	7.960	3.737
NGC 3198	0.03	5	14.10	8.76	10.111	0.055	0.007	7.546	9.892	9.460	0.837
NGC 3265	0.07	−5	19.60	8.69	9.566	−0.651	−0.427	6.355	9.442	8.121	2.501
NGC 3351	0.08	3	9.33	8.77	10.208	−0.166	−0.112	7.269	9.883	8.979	1.620
NGC 3521	0.16	4	11.20	8.81	10.791	0.441	0.425	7.975	10.524	9.216	2.471
NGC 3621	0.22	7	6.55	8.75	10.002	−0.038	0.096	7.330	9.858	9.287	1.038
NGC 3627	0.09	3	9.38	8.62	10.587	0.369	0.389	7.633	10.450	9.223	2.291
NGC 3773	0.07	−2	12.40	8.58	9.038	−0.949	−0.774	5.919	8.811	8.595	0.581
NGC 3938	0.06	5	17.90	8.68	10.396	0.472	0.288	7.735	10.213	−	−
NGC 4236	0.04	8	4.45	8.37	9.027	−0.773	−0.886	6.446	8.602	8.926	0.201
NGC 4254	0.11	5	14.40	8.79	10.551	0.574	0.568	7.881	10.586	9.633	1.716
NGC 4321	0.07	4	14.30	8.76	10.684	0.509	0.428	7.955	10.488	9.596	1.597
NGC 4536	0.05	4	14.50	8.63	10.301	0.291	0.337	7.537	10.362	9.338	1.860
NGC 4559	0.05	6	6.98	8.58	9.595	−0.312	−0.307	7.007	9.430	9.205	0.590
NGC 4569	0.13	2	9.86	8.80	10.252	−0.347	−0.346	7.149	9.735	8.544	2.213
NGC 4579	0.11	3	16.40	8.79	10.766	0.023	−0.008	7.607	10.032	8.977	1.924
NGC 4594	0.14	1	9.08	8.79	11.104	−0.458	−0.747	7.291	9.521	8.431	1.997
NGC 4625	0.05	9	9.30	8.67	8.963	−1.009	−1.136	6.283	8.720	8.521	0.563
NGC 4631	0.05	7	7.62	8.38	10.219	0.380	0.346	7.624	10.355	9.589	1.363
NGC 4725	0.03	2	11.90	8.71	10.599	−0.027	−0.566	7.724	9.771	9.282	0.916
NGC 4736	0.05	2	4.66	8.68	10.256	−0.212	−0.311	6.827	9.777	8.976	1.426
NGC 4826	0.11	2	5.27	8.78	10.205	−0.472	−0.573	6.724	9.634	8.354	2.409
NGC 5055	0.05	4	7.94	9.31	10.566	0.250	0.146	7.843	10.248	9.209	1.890
NGC 5398	0.18	8	7.66	8.33	8.675	−1.160	−0.949	5.903	8.619	8.421	0.562
NGC 5408	0.19	10	4.80	8.19	8.256	−1.562	−0.903	4.980	8.265	−	−
NGC 5457	0.02	6	6.70	8.73	10.489	0.513	0.419	7.877	10.301	10.008	0.665
NGC 5474	0.03	6	6.80	8.46	9.043	−0.820	−1.034	6.383	8.647	8.851	0.259
NGC 5713	0.11	4	21.40	8.70	10.348	0.431	0.485	7.501	10.558	9.153	2.691
NGC 5866	0.04	−2	15.30	8.73	10.772	−0.354	−0.918	6.943	9.784	7.967	3.664
NGC 6946	0.94	6	6.80	8.75	10.572	0.535	0.627	7.863	10.566	9.705	1.538
NGC 7331	0.25	3	14.50	8.80	10.931	0.635	0.508	8.125	10.665	9.281	2.643
NGC 7793	0.05	7	3.91	8.64	9.410	−0.472	−0.469	6.876	9.232	9.079	0.518

B.1. Reference stellar mass

The availability of data at near- to mid-infrared (NIR, MIR) wavelengths, both from *Spitzer*/IRAC and WISE, has prompted the widespread use of 3.4 or 3.6 μm luminosities to measure stellar mass. At these wavelengths, the mass-to-light (M/L = Υ_*) ratios of stellar populations are relatively constant, independently of metallicity and age (Eskew et al. 2012; Meidt et al. 2014; Norris et al. 2014; McGaugh & Schombert 2014). We have relied on two formulations for estimating M_{star} from 3.4–3.6 luminosities: the first by Wen et al. (2013) is based on WISE W1 (3.4 μm) photometry and calibrated to the stellar masses from the Sloan Digital Sky Survey (SDSS) value-added catalogs. We have used IRAC 3.6 μm luminosities interchangeably with WISE W1 3.4 μm values. For the 59 KINGFISH galaxies with both W1 and IRAC photometry the mean ratio is 1.07 ± 0.09. Grossi et al. (2015) find for 23 spiral galaxies a mean flux ratio $F_{3.4}/F_{3.6} = 1.02 ± 0.035$, and using data from Brown et al. (2014b), and Hunt et al. (2015b) obtain a mean flux ratio $F_{3.4}/F_{3.6} = 0.98 ± 0.061$. Thus, within the uncertainties of the photometry, WISE W1 3.4 μm and IRAC 3.6 μm photometry is virtually indistinguishable.

For the estimates of the recipe stellar masses, we combine IRAC 3.6 μm luminosities and the Wen et al. (2013) approach based on Hubble type, divided into early- and late-type galaxies; we also apply their suggested correction for low metallicity (12+log(O/H) ≤ 8.2) amounting to a multiplicative factor of 0.8. The Kroupa (2001) IMF used by Wen et al. (2013) was converted to Chabrier (2003) according to the formulation of Speagle et al. (2014). The second method for calculating stellar mass assumes a constant Υ_* value at 3.6 μm, as found by Eskew et al. (2012), Meidt et al. (2014), Norris et al. (2014), McGaugh & Schombert (2014). Here we adopt the McGaugh & Schombert (2014) Υ_* (in solar units at 3.6 μm) $\Upsilon^{[3.6]} = 0.47$, assuming that $L_\odot(3.6\,\mu$m$) = 1.4 \times 10^{32}$ erg s^{-1} as given by Cook et al. (2014).

However, before applying either method, we first estimate the non-stellar continuum at these wavelengths and subtract it. Such contamination can be very important in dwarf galaxies, especially in those with high SFRs (e.g., Smith & Hancock 2009). The contribution from the ionized gas continuum to the 3.4–3.6 μm flux was estimated from the SFR (see Sect. B.2) using the emission coefficients from Osterbrock & Ferland (2006). We did not attempt to subtract emission from hot dust, since globally its contribution in disk galaxies is typically small (≲10%, Meidt et al. 2012). For the KINGFISH galaxies, our estimate of the fraction of nebular continuum in the 3.6 μm IRAC band ranges from 0 to 2%, so is a very small correction.

B.2. Reference star-formation rate

To estimate SFRs, we used Eq. (18) by Murphy et al. (2011) based on L_{FUV} and L_{TIR}; these quantities were available for 50 galaxies. Otherwise, we preferred the SFR estimate from L_{FUV} (Eq. (3) in Murphy et al. 2011) which was possible only for DDO 154 and DDO 165 (these galaxies are missing also MIPS 24 μm and longer-wavelength detections, and DDO 154 has no detections at all beyond IRAC 4.5 μm). As the last choice, we took SFR from L_{TIR} (Eq. (4) in Murphy et al. 2011) which assumes that only the FUV radiation up to the Balmer decrement is reprocessed by dust; SFR(TIR) is used for 9 galaxies (IC 342, NGC 1377, NGC 2146, NGC 3049, NGC 3077, NGC 393, NGC 4254, NGC 4321, and NGC 5408). In all cases, the Kroupa (2001) IMF adopted by Murphy et al. (2011) was converted to Chabrier according to Speagle et al. (2014).

In order to obviate possible problems with FUV+TIR derived SFRs, we also calculated SFRs inferred from Hα and 24μm luminosities using Hα fluxes corrected for Galactic extinction and [N II] contamination from Kennicutt et al. (2009) or Moustakas et al. (2010). To convert these quantities to SFRs, we adopted the constants from Calzetti et al. (2010) (which are within 1% of those used by Murphy et al. 2011), after adjusting them to an electron temperature of $\sim$7000 K (to calibrate Hα Murphy et al. 2011, uses $T = 10\,000$ K) in order to minimize the offset with the SFRs inferred from $L_{FUV}+L_{TIR}$. When Hα is unavailable in Kennicutt et al. (2009) or Moustakas et al. (2010) (i.e., for NGC 855, NGC 1266, NGC 1316, NGC 1404), we have taken SFR estimates from Kennicutt et al. (2011) or Skibba et al. (2011) after correcting to the same distance scale as Kennicutt et al. (2011). The assumed IMF (Kroupa 2001) was converted to Chabrier (2003), as before according to Speagle et al. (2014). These Hα+24μm SFRs are available for 60 galaxies.

B.3. Reference dust masses

Although numerous studies have inferred dust masses, M_{dust}, of the KINGFISH galaxies (e.g., Draine et al. 2007; da Cunha et al. 2008; Noll et al. 2009; Muñoz-Mateos et al. 2011; Dale et al. 2012; Rémy-Ruyer et al. 2015), they are all based on models, either the ones scrutinized here or others (e.g., Draine & Li 2007; Galliano et al. 2011). To compare the values of M_{dust} found here through SED fitting, we prefer to minimize discrepancies induced by differences in the assumptions made by models. Thus, we adopted the dust masses calculated according to Bianchi (2013) who performed single-temperature modified blackbody (MBB) fits to the KINGFISH galaxies, and assessed differences caused by different dust opacities assumed by various groups. New dust masses were calculated with the same methods as in Bianchi (2013), but using the updated *Herschel* fluxes (see Dale et al. 2017) and the revised *Herschel* filter transmission curves; as in Bianchi (2013), the dust opacities are taken from the DL07 models. These new M_{dust} values are, on average, 0.83 times those found by Bianchi (2013), with most of the change due to the updated flux values. Three KINGFISH galaxies are missing the requisite IR detections to infer M_{dust}: DDO 154, DDO 165, and NGC 1404.

For completeness, we also include in the comparison the updated M_{dust} values taken from (Aniano et al., in prep., their Table 10). These values are derived using the DL07 models presented by Aniano et al. (2012), but have been renormalized taking into account the post-Planck results (Planck Collaboration Int. XXIX 2016).

B.4. Reference luminosities and attenuation

We have calculated L_{TIR} as suggested by DL07 based on *Spitzer* photometry and by Galametz et al. (2013, G13) by combining *Spitzer* and *Herschel*. DL07 gives an analytical expression for L_{TIR} based on luminosities at IRAC 8 μm, and the MIPS bands at 24, 70, and 160 μm. The expression is calibrated on their models and describes the modeled L_{TIR} to within $\sim$10%. From G13, we took the formulation (from their Table 3) for L_{TIR} based on the linear combination with the lowest RMS error, normalized to the mean values of global flux density. To optimize the choice of indicator, we also considered the one based on the largest number of detections for the KINGFISH galaxies (somewhat fewer galaxies were detected with SPIRE). With these constraints, the best G13 recipe, also calibrated on the DL07 models, is based on MIPS 24 μm, and two PACS bands, 70 and 100 μm (see Table B.1).

The FUV luminosity, $L_{FUV} = \nu_{FUV} \ell_{FUV}$ ($\lambda = 0.15 \mu$m), is calculated from the observed FUV fluxes corrected for extinction, according to Murphy et al. (2011), based on IRX, the logarithm (base 10) of the ratio of L_{TIR} to observed FUV luminosity, L_{FUV}[15]. The constant 0.43 relating L_{TIR} to L_{FUV} of Murphy et al. (2011) is close to the value of 0.46 found by Hao et al. (2011), and the two estimates give similar results. IRX is a relatively robust indicator of dust attenuation because it is based on energy balance arguments, and is almost independent of dust properties and dust geometry relative to heating sources (e.g., Buat et al. 2005; Hao et al. 2011). The FUV attenuation, A_{FUV} ($\lambda = 0.15 \mu$m) is taken accordingly from Murphy et al. (2011), again using L_{TIR} from the G13 formulation (see Table B.1).

---

[15] Here we have used L_{TIR} from the formulation of G13.